Title

Durable Pt-based Catalysts for Oxygen Reduction Reaction in Fuel Cell

Author

Liu, Zeyan

Publication Date

2022

Peer reviewed|Thesis/dissertation

UNIVERSITY OF CALIFORNIA

Los Angeles

Durable Pt-based Catalysts for Oxygen Reduction Reaction in Fuel Cell

A dissertation submitted in partial satisfaction of the requirements

for the degree Doctor of Philosophy in Materials Science and Engineering

By

Zeyan Liu

2022

ABSTRACT OF THE DISSERTATION

Durable Pt-based Catalysts for Oxygen Reduction Reaction in Fuel Cell

by

Zeyan Liu

Doctor of Philosophy in Materials Science and Engineering

University of California, Los Angeles, 2022

Professor Yu Huang, Chair

Fuel cells are devices that can efficiently convert fuels into electricity without the limitation of the Carnot cycle. Hydrogen fuel cells have attracted enormous interest due to their high energy density, high-efficiency, and low environmental impacts. The most widely adopted proton-exchange-membrane fuel cells (PEMFCs) use platinum (Pt) catalysts to drive both anode and cathode reactions. To date, the acceleration and retention of the reaction rate of oxygen reduction reaction (ORR) at the cathode remain the roadblock to the broad dissemination of this clean energy technology. The development of robust, high-performing, and cost-effective ORR catalysts is the solution to this challenge.

The first chapter of my dissertation is the introduction of fuel cell devices, ORR fundamental principles, and catalyst design principles.

In the second chapter, I demonstrated a strategy to enhance the intrinsic durability of catalysts in rotating-disk-electrode (RDE) testing. The enhanced stability and ORR activity of

octahedral PtNi nanoparticles are achieved by tuning the surface elemental distribution by introducing a third element (Cu) during synthesis. To uncover the mechanism behind this observation, we performed kinetic Monte Carlo (KMC) simulations initialized using growth tracking experiments and demonstrated that the enhanced stability can be attributed to the increased surface Pt composition of as-synthesized catalysts, which reduces the generation of surface vacancies and suppresses the surface migration and subsequent dissolution of sub-surface Cu and Ni atoms.

While RDE testing provides information on the intrinsic catalytic activity of a catalyst without the interference from ohmic and mass transport losses, it is realized that not all catalysts with promising RDE performance can be translated into practical membrane-electrode-assembly (MEA). It is, therefore, necessary to perform MEA performance evaluation in the early stage of catalyst material development. Specifically, the importance of mass transport in MEA demands additional consideration in stability-enhancing strategies. In the third chapter, I recognized the critical challenge in MEA with ultralow Pt loading and designed a graphene-nanopocket-encaged platinum cobalt nanocatalyst with good electrochemical accessibility and exceptional durability in practical MEA testing. The developed catalyst delivers a state-of-the-art mass activity of 1.21 A/mg_{Pt}, a rated power of 13.2 W/mg_{Pt}, and a mass activity retention of 73% after the accelerated durability test. With the greatly improved rated power and durability, a 6.8 gram Pt loading is projected for a 90-kW PEMFC light-duty vehicle, approaching that used in a typical catalytic converter (2-8 gram).

In the last chapter, to mitigate the additional MEA performance losses related to the leaching of transition metal contents and corresponding cation poisoning effects, I presented a unique design of ultrafine Pt nanocatalysts with embedded cobalt oxide clusters which exploits the

benefit from Pt/oxide interaction to further improve the catalyst stability for durable MEA and PEMFCs without sacrificing activity. The developed nanocatalyst delivers an outstanding initial mass activity of 1.10 A/mg_{Pt}, a rated power density of 1.04 W/cm^2, and a Pt utilization of 10.4 W/mg_{Pt} in a membrane electrode assembly. It exhibits exceptional durability featuring a mass activity retention of 88.2%, a voltage loss of 13.3 mV at 0.8 A/cm^2, and an ultrasmall rated power loss of 7.5% after the accelerated durability test. The extraordinary durability promises a projected lifetime of 15,000 hours.

The dissertation of Zeyan Liu is approved.

Qibing Pei

Ximin He

Xiangfeng Duan

Yu Huang, Committee Chair

University of California, Los Angeles

2022

DEDICATION

to:

My parents Zhongqing Liu, Weiwei Cheng;

My beloved partner Bosi Peng,

For their unconditional support and endless love.

Table of Contents

List of Figures, Schemes, and Tables

Acknowledgments

I would like to express my gratitude to my advisor and chair of my committee, Prof. Yu Huang, for her invaluable advice and continuous support throughout the course of my Ph.D. degree. Her insights on both scientific research and work philosophy were indispensable for accomplishing this dissertation. I would also like to extend my sincere thanks to Prof. Xiangfeng Duan, who also generously provided knowledge and expertise. I would also like to thank my committee members, Prof. Qibing Pei, and Prof. Ximin He for their help on my Ph.D. qualification exam and final dissertation.

Moreover, I would like to thank my collaborators Dr. Qingying Jia from Northeastern University, Dr. Alessandro Fortunelli and his colleagues Dr. Luca Sementa from Italian national research council, Dr. Mingjie Xu and Dr. Xingxu Yan from the University of California, Irvine. I could not have undertaken this journey without their expertise and knowledge. I am also grateful to my colleagues Bosi Peng, Dr. Jin Huang, Dr. Zipeng Zhao for close collaboration on several of my projects. Finally, I would like to thank Dr. Enbo Zhu, Dr. Haotian Liu, Dr. Guangyan Zhong, Dr. Bocheng Cao, Jin Cai, Xu Dong, Ao Zhang, Yu-Han Tsai, Yang Liu and all other group members and collaborators who helped me a lot during my Ph.D. study.

Lastly, I would be remiss in not mentioning my family, especially my parents and my partner. Their belief in me has kept my spirits and motivation high during this process. I would also like to thank my puppy, Bear, for all the entertainment and emotional support.

The introduction in Chapter One is a partial version of *Journal of the American Chemical Society*, **Zeyan Liu**, Zipeng Zhao, Bosi Peng, Xiangfeng Duan, Yu Huang. 2020, 142, 42, 17812-17827. DOI: 10.1021/jacs.0c07696

Chapter Two is a version of *Matter*, Liang Cao, Zipeng Zhao, **Zeyan Liu (equal contribution)**, Wenpei Gao, Sheng Dai, Joonho Gha, Wang Xue, Hongtao Sun, Xiangfeng Duan, Xiaoqing Pan, Tim Mueller, Yu Huang. 2019, 1, 6, 1567-1580. DOI: 10.1016/j.matt.2019.07.015

Chapter Three is a version of *Nature Nanotechnology*, Zipeng Zhao, **Zeyan Liu (equal contribution)**, Ao Zhang, Xingxu Yan, Wang Xue, Bosi Peng, Huolin L. Xin, Xiaoqing Pan, Xiangfeng Duan, Yu Huang, 2022, 17, 968-975. DOI: 10.1038/s41565-022-01170-9

Chapter Four is a version of [Submitted manuscript] Author list: Bosi Peng, **Zeyan Liu (equal contribution)**, Luca Sementa, Qiang Sun, Qingying Jia, Zipeng Zhao, Jin Huang, Mingjie Xu, Alessandro Fortunelli, Xiangfeng Duan, Yu Huang

VITA

Education

2017 B.S. in Chemistry, Chu Kochen Honors College, Zhejiang University, China

Honor

2017 UCLA University Fellowship

2021 UCLA Summer Mentored Research fellowship

2021 UCLA Dissertation Year fellowship

Selected Publications (10 out of 14)

1. Zipeng Zhao, **Zeyan Liu (Equal contribution)**, Ao Zhang, Xingxu Yan, Wang Xue, Bosi Peng, Huolin L Xin, Xiaoqing Pan, Xiangfeng Duan, Yu Huang. "Graphene-nanopocket-encaged PtCo nanocatalysts for highly durable fuel cell operation under demanding ultralow-Pt-loading conditions." *Nature Nanotechnology* (2022).
2. Bosi Peng, **Zeyan Liu (Equal contribution)**, Luca Sementa, Qiang Sun, Qingying Jia, Zipeng Zhao, Jin Huang, Mingjie Xu, Alessandro Fortunelli, Xiangfeng Duan, Yu Huang, Ultrafine Pt Nanoparticles with Endohedral Oxide Clusters for Highly Durable Fuel Cells. (*Submitted*)
3. **Zeyan Liu**, Zipeng Zhao, Bosi Peng, Xiangfeng Duan, and Yu Huang. "Beyond Extended Surfaces: Understanding the Oxygen Reduction Reaction on Nanocatalysts." *Journal of the American Chemical Society* 142, 42, 17812-17827 (2020).
4. Liang Cao, Zipeng Zhao, **Zeyan Liu (Equal contribution)**, Wenpei Gao, Sheng Dai, Joonho Gha, Wang Xue, Hongtao Sun, Xiangfeng Duan, Xiaoqing Pan, Tim Mueller, Yu Huang. "Differential surface elemental distribution leads to significantly enhanced stability of PtNi-based ORR catalysts." *Matter* 1, 6, 1567-1580 (2019).
5. Zipeng Zhao, Changli Chen, **Zeyan Liu (Equal contribution)**, Jin Huang, Menghao Wu, Haotian Liu, Yujing Li, Yu Huang. Pt-Based Nanocrystal for Electrocatalytic Oxygen Reduction. *Advanced Materials* 31,31, 1808115 (2019).
6. Jin Huang, Luca Sementa, **Zeyan Liu**, Giovanni Barcaro, Miao Feng, Ershuai Liu, Li Jiao, Mingjie Xu, Denis Leshchev, Sung-Joon Lee, Mufan Li, Chengzhang Wan,

Enbo Zhu, Yang Liu, Bosi Peng, Xiangfeng Duan, William A Goddard, Alessandro Fortunelli, Qingying Jia, Yu Huang. " Experimental Sabatier plot for predictive design of active and stable Pt-alloy oxygen reduction reaction catalysts", *Nature Catalysis* 5, 513–523 (2022)

7. Jin Huang; Bosi Peng; Thomas Stracensky; **Zeyan Liu**; Ao Zhang; Mingjie Xu; Yang Liu; Zipeng Zhao; Xiangfeng Duan; Qingying Jia; Yu Huang. "Ultralow Loading PtCo Nanowire Catalysts for High-Performance PEMFCs", *Science China Materials* 65 (3), 704-711 (2022)

8. Enbo Zhu, Menghao Wu, Haozhe Xu, Bosi Peng, **Zeyan Liu**, Yujing Li, Yu Huang, Stability of Pt-Group-Metal-based Electrocatalysts in PEMFC, *Advanced Functional Materials*, 2022, 2203883

9. Bosi Peng; Haotian Liu; **Zeyan Liu**; Xiangfeng Duan; Yu Huang. "Towards Rational Design of Single Atom Catalysts", *The Journal of Physical Chemistry* Letters 12 (11), 2837-2847 (2021)

10. Zipeng Zhao, Md Delowar Hossain, Chunchuan Xu, Zijie Lu, Yi-Sheng Liu, Shang-Hsien Hsieh, Ilkeun Lee, Wenpei Gao, Jun Yang, Boris V Merinov, Wang Xue, **Zeyan Liu**, Jingxuan Zhou, Zhengtang Luo, Xiaoqing Pan, Francisco Zaera, Jinghua Guo, Xiangfeng Duan, William A Goddard III, Yu Huang. "Tailoring a Three-Phase Microenvironment for High-Performance Oxygen Reduction Reaction in Proton Exchange Membrane Fuel Cells", *Matter* 3, 5, 1774-1790 (2020)

Chapter 1. Introduction

1.1 Fuel Cell Fundamentals and Principles

Currently, climate change and environmental issues induced by the combustion of fossil fuels are becoming more prominent in human society. The largest sources of carbon dioxide greenhouse gas emissions have been found in the electric generation facilities and the transportation sectors.[1] Targeting at solving these issues, developing sustainable and efficient energy conversion devices becomes an urgent need. Proton-exchange-membrane fuel cells (PEMFCs) represent one of the most attractive and sustainable power generation technologies given its board range of benefits, including zero-emission, high efficiency, high power density, and reduced fossil fuel consumption.[2-3] In particular, fuel cells convert the chemical energy from the fuels into electricity without the limitation of the Carnot cycle; this advantage grants fuel cells great potential to replace the conventional internal combustion engine (ICE) in transportation applications.[4]

For the general principle of a hydrogen fuel cell, as shown in Figure 1.1, the hydrogen fuel and oxygen are fed to the anode and cathode, respectively, through the flow channels and gas diffusion layers (GDL). The hydrogen undergoes an oxidation reaction at the anode and produces protons and electrons, while the oxygen is reduced at the cathode and combined with the electrons and protons to form water. Due to the sluggish kinetics of the cathode oxygen reduction reaction (ORR), a large amount of platinum-based catalyst is needed, hindering the broad dissemination of PEMFCs.[5] To date, Pt-based catalysts account for more than 40% cost of fuel cell stacks.[6] Therefore, the development of robust, high-performing, and cost-effective ORR catalysts is central to the task.[7-8]

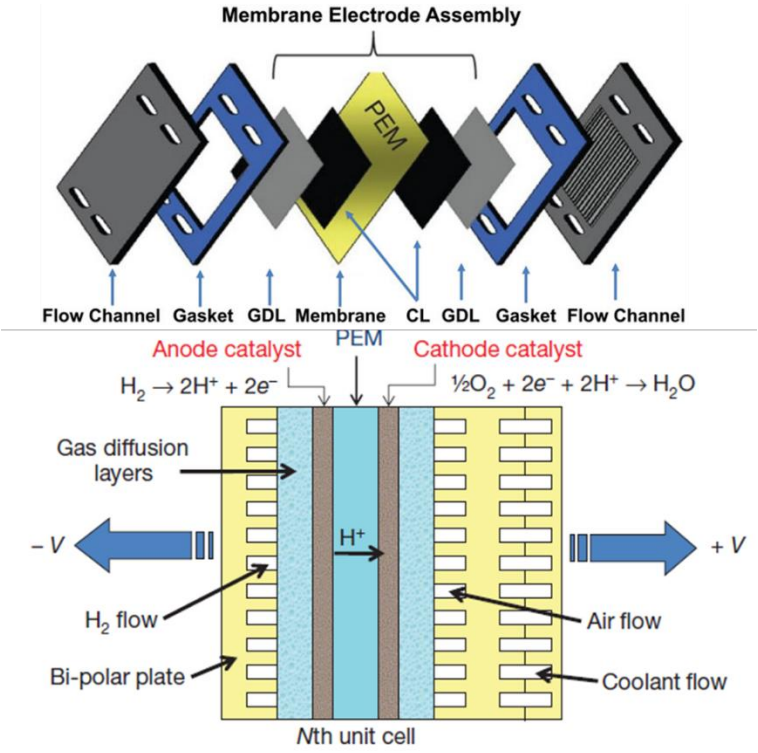

Figure 1. 1. The schematic of proton-exchange-membrane fuel cells (PEMFCs) components and working principles. Adapted with permission from Ref.[4]. Copyright 2012 Springer Nature.

1.2 Oxygen reduction reaction (ORR) Fundamentals

The mechanism of ORR has been extensively investigated experimentally and computationally.[3, 9-12] In ORR, oxygen (O_2) is reduced to water (H_2O) involving four protons and four electrons [$O_2 + 4(H^+ + e^-) \rightarrow 2H_2O$].[13] On the catalytic surface of Pt, ORR usually adopts the four-electron pathway into H_2O.[9] It is also proposed that the direct four-electron ORR can occur through either a dissociative or an associative route, depending on whether the O_2 molecule dissociates before the reduction (Figure 1.2). The dissociation pathway is preferred when the surface binds O_2 strongly or when the oxygen surface coverage is low, while the association pathway is favored when the surface O_2 adsorption is weak or when the surface oxygen coverage is high.[9, 14]

Although multiple oxygen species (*e.g.*, O_{ad}, OH_{ad}, OOH_{ad}) are involved in ORR, as they bind similarly to the surface through the O atom, their adsorption energy can be linearly related

according to the "scaling relationship" (*e.g.*, $E_{ad1}=\gamma E_{ad2}+\xi$, γ and ξ are constants for a given set of adsorbates ad1, ad2 at a given adsorption site).[15-16] Hence usually only one adsorbate is used to describe the adsorption energy of all intermediates and products.[14] In the analysis of ORR catalysis, the adsorption energy of O_{ad} or OH_{ad} is widely used.[17] The understanding of the ORR catalytic activity falls under the Sabatier principle, which prescribes that the interaction between the oxygen species and the catalyst surface need to be just right in order to achieve the best ORR activity.[9] If the surface binds oxygen too strong, the ORR kinetics will be limited by the electron/proton transfer to the O_{ad} or OH_{ad}, while a weak binding hampers the electron/proton transfer to O_{2ad}.[18] It is also recognized that Pt surface binds oxygen stronger than the optimal value, leaving room for further improvement.[3, 7, 9]

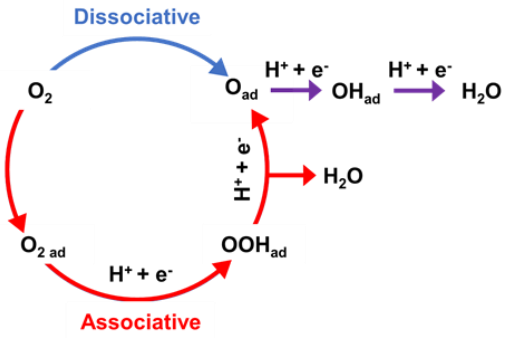

Figure 1. 2. Schematic illustration for the direct four-electron ORR path-ways. The red and blue arrows represent the associative and the dissociative pathway, respectively. The purple arrows represent the reactions that include in both pathways. Adapted with permission from Ref.[5] Copyright 2020 American Chemical Society.

1.3 Theories for the Design of ORR Catalysts

The development of theoretical understanding allows researchers to rationalize their experimental observations. Several reviews have well summarized the development of theories and reactivity descriptors for heterogeneous catalysis.[3, 14, 19] Here, we will briefly introduce theories that shape our understanding of the ORR catalysts.

d-band theory: The d-band theory that connects the surface adsorption behavior of adsorbates and the d-states of the transition metals was established by Nørskov and Hammer in the 1990s via analyzing the interactions between the adsorbates and (111) surfaces of different transition metals.[20-21] The theory links the surface adsorption strength with the different d-band filling of the metal.[20-24] It looks at the electronic states of the transition metal surface in two groups: the sp-bands and the d-bands. As all transition metals have similar broad sp-bands (Figure 1.3a, light blue), it is assumed that their interaction with the valence states of the adsorbates is the same, and hence their contribution to adsorption energy does not vary across different surfaces.[25-26] Thus, the difference in adsorption behavior on various transition metal surfaces is mainly determined by the different coupling between the adsorbate's valence states and the metal d states (Figure 1.3a, red), which produces bonding and antibonding states. The adsorption strength is governed by the filling of the antibonding states due to its proximity to the Fermi level. The upshift (downshift) in d states energy would lead to an upshift (downshift) in antibonding states, and decreased (increased) antibonding filling, which results in stronger (weaker) adsorption. [23, 25-26] To simplify the description of the energy level of d-band, d-band center (ε_d) which represents the average energy of the d band was introduced and widely adopted (Figure 1.3a).[18, 24, 26-27] This correlation between the ε_d and the oxygen adsorption energy, which scales with ORR activity, was demonstrated on the extended surfaces of Pt and Pt-alloys in both theoretical and experimental studies with reasonable correlation.[2, 27-28]

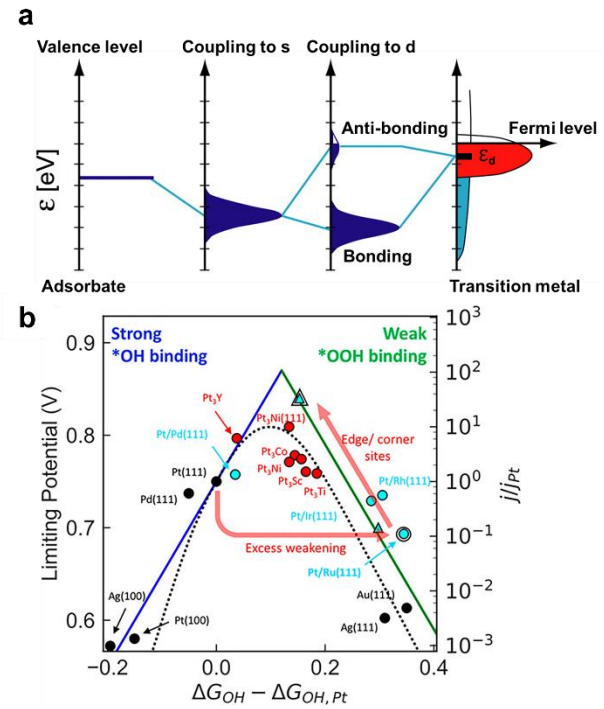

Figure 1. 3. (a) The d-band model for the illustration of the formation of a chemical bond between an adsorbate valence level (leftmost) and the s and d states of a transition-metal surface (rightmost). (b) Relationships between the ORR kinetics and the OH_{ad} adsorption energy, in terms of the calculated limiting potential ($U_{Limiting} = U_{equilibrium} - U_{overpotential}$, solid blue, and green lines) at various metal surfaces (black circle) and the measured kinetic current (black dash line) of Pt_3M alloys (red), and Pt overlayer catalysts (cyan) related to Pt(111). (A) Adapted with permission from Ref.[24] Copyright 2000 Elsevier. (B) Adapted with permission from Ref.[14] Copyright 2018 American Chemical Society.

Within the framework of d-band theory, it is suggested that changing the surface electronic structure (d-band) of the transition metals results in the modulation of the adsorption strength of oxygen species on the catalyst surface, which leads to modified ORR kinetics (Figure 1.3b).[14] With the same metal, the position of ε_d depends significantly on the d-band bandwidth (W_d) as ε_d must change in accordance with W_d to conserve both the d-band filling and the total number of d states.[29] According to the tight-binding model,[30] W_d is proportional to interatomic matrix element (V_i) which describes the atomic arrangement of the surface atom i and its neighboring atoms j.[25, 30] ε_d is thus dependent on the coordination number *(CN)* the characteristic length (r_d) which

correlates with the type of the metal atom, and the distance between the atoms (d_{ij}), as described in Eq. 1.[29]

$$|\varepsilon_d| \propto W_d^{0.5} \propto V_i = \sum_{j=1}^{CN} \frac{\left(r_{d,i} r_{d,j}\right)^{1.5}}{d_{ij}^5} \quad (1)$$

Rooted in this theory, most recent discussions on improving ORR kinetics of Pt-based catalysts centered around ε_d modulation through facet effect,[18] ligand effect,[2, 18, 31] and strain effect,[3, 32] which are briefly summarized below to aid the following discussions.

Facet effect: The structure sensitivity of ORR on low-index Pt surface and its dependence on the *CN* of surface atoms was firstly investigated by Ross *et al*. in 1979, using a stationary single-crystal electrode.[33-34] However, their experimental observations suggested no structural sensitivity toward ORR activity for low index Pt surfaces.[33] It was suggested that the high cycling potential (0-1.5 V vs. reversible hydrogen electrode (RHE). All potentials are referenced to RHE unless specified) could lead to the roughening of Pt surface that assimilated the atomic features.[35-36] To avoid this issue, Marković *et al*. performed the experiments within the potential range of -0.07 to 0.8 V.[37-38] In contrast to the results of Ross *et al.*,[33] they found that the activity for ORR decreased in the sequence (110)>(111)>(100) in 0.1M $HClO_4$.[13] This trend has been attributed to the different oxygen adsorption (O-adsorption) energy on different facets.[14] Per d-band theory, ε_d depends on the *CN* of the metal atom (*CN* in Eq. 1).[39] Since the average *CN* of surface Pt atom decreases in the order of (111) >(100)>(110), ε_d and O-adsorption energy vary accordingly.[25] The observed high activity of (110) surface was the result of surface reconstruction in the electrochemical environment,[40-42] while the unreconstructed (110) exhibited lower activity to (111) in 0.1M $HClO_4$.[42] It indicates the importance of catalyst surface dynamics in correct interpretation of the ORR performance.

Ligand effect: As an effort to enhance the performance and to reduce the cost of Pt-based catalyst, alloying Pt with a non-noble transition metal has been proposed.[2, 18, 31] In a bimetallic system, the d-band theory predicts the d-states of the surface Pt atoms can be modulated by the degree of electron transfer between Pt and the surrounding atoms, also known as the ligand effect. Kitchin *et al*. studied ligand effect in different bimetallic Pt-alloys using density-functional theory (DFT), on Pt(111) single-crystal surface with different transition metals at the subsurface layer.[29] The calculation showed that ε_d of the surface Pt downshifted in energy through interactions with different subsurface 3d metals from Ni to Ti. The trend was explained in the framework of d-band theory, where the r_d increases from the right (Ni) to the left (Ti) in the periodic table, leading to the increase of W_d and downshift of ε_d (Eq. 1). This results in decreased O-adsorption on alloy surface compared to that of pure Pt. The downshift trend of ε_d with 3d metals was also observed experimentally with ultraviolet photoemission spectroscopy (UPS)-determined ε_d on Pt_3M (M=Ni, Co, Fe, V, Ti) polycrystal films.[18, 28] In addition, the measured specific activity (SA) of these Pt_3M polycrystal films were shown to correspond to the measured ε_d in a "volcano-shaped" relation, consistent with the Sabatier principle.[18] It was shown later that the ligand effect also depended on the concentration of the transition metal atoms in the subsurface layer, in near-surface-alloy (NSA) Cu/Pt(111) single-crystal electrode with negligible bulk lattice strain.[31] It was demonstrated that with an increasing concentration of Cu at subsurface, the SA showed a "volcano-shaped" relation as the OH_{ad} adsorption on Pt surface was increasingly weakened due to the enhanced ligand effect between subsurface Cu and surface Pt. This study indicates the importance of near-surface composition in modulating ORR activity. It is worth pointing out that deviation from d-band theory using ε_d-analysis has been reported in theoretical studies on some NSA systems with fully

substituted subsurface, which highlighted the need to develop more inclusive descriptors.[16, 43] Nevertheless, further experimental investigations and validations of these outliners are demanded.

Strain effect: Strain originates from the difference in lattice constants between surface Pt and the underlying crystal structure.[32, 44-45] Luo *et al.* have summarized the effect of strain on the electronic structure that can be described by the d-band theory.[32] In brief, for late transition metals with more than half-filled d-band, the expanded surface (tensile strain) can increase the distance between surface Pt atoms (d_{ij}) and, according to Eq. 1, narrow the d-band and thus result in an upshift of ε_d towards the Fermi level. This upshift can result in stronger O-adsorption on the Pt surface. On the contrary, the compressive strain on Pt surface will weaken surface O-adsorption.[32] It is worth noting that the ligand effect and strain effect usually coexist in Pt-alloys. A study of CO adsorption energy on different layers of Pt on Ru(0001)[44] suggests that the ligand effect becomes negligible when the Pt surface is thicker than three atomic layers, while the strain effect only gradually decreases after five atomic layers. Following this rationale, Escudero-Escribano *et al*. performed ORR studies on acid-leached polycrystalline Pt-lanthanide alloys with a Pt shell thickness of around five atomic layers to experimentally deconvolute strain effect from ligand effect.[46] It was observed that with decreasing atomic radius of lanthanide atoms, the surface compressive strain increased accordingly which resulted in decrease OH_{ad} adsorption energy, and thus led to the measured volcano-shaped ORR activity trend as predicted by the Sabatier principle.[46]

1.4 References

1. *Fuel Cell Technologies Office Multi-Year Research, Development, and Demonstration Plan*; U.S. Department of Energy, 2017.

2. Greeley, J.; Stephens, I. E. L.; Bondarenko, A. S.; Johansson, T. P.; Hansen, H. A.; Jaramillo, T. F.; Rossmeisl, J.; Chorkendorff, I.; Nørskov, J. K., Alloys of Platinum and Early Transition Metals as Oxygen Reduction Electrocatalysts. *Nature Chemistry* 2009, **1**, 552-556 doi:10.1038/nchem.367

3. Zhao, Z.; Chen, C.; Liu, Z.; Huang, J.; Wu, M.; Liu, H.; Li, Y.; Huang, Y., Pt-Based Nanocrystal for Electrocatalytic Oxygen Reduction. *Advanced Materials* 2019, **31**, 1808115 doi:10.1002/adma.201808115

4. Debe, M. K., Electrocatalyst Approaches and Challenges for Automotive Fuel Cells. *Nature* 2012, **486**, 43-51 doi:10.1038/nature11115

5. Liu, Z.; Zhao, Z.; Peng, B.; Duan, X.; Huang, Y., Beyond Extended Surfaces: Understanding the Oxygen Reduction Reaction on Nanocatalysts. *Journal of the American Chemical Society* 2020, **142**, 17812-17827 doi:10.1021/jacs.0c07696

6. James, B.; Huya-Kouadio, J.; Houchins, C.; Desantis, D., *Final Sa 2018 Transportation Fuel Cell Cost Analysis -2020-01-23*. 2018.

7. Debe, M. K., Electrocatalyst Approaches and Challenges for Automotive Fuel Cells. *Nature* 2012, **486**, 43-51 doi:10.1038/nature11115

8. Vielstich, W.; Lamm, A.; Gasteiger, H. A., *Handbook of Fuel Cells: Fundamentals Technology and Applications*. Wiley New York: 2003; Vol. 3.

9. Nørskov, J. K.; Rossmeisl, J.; Logadottir, A.; Lindqvist, L.; Kitchin, J. R.; Bligaard, T.; Jónsson, H., Origin of the Overpotential for Oxygen Reduction at a Fuel-Cell Cathode. *The Journal of Physical Chemistry B* 2004, **108**, 17886-17892 doi:10.1021/jp047349j

10. Nie, Y.; Li, L.; Wei, Z., Recent Advancements in Pt and Pt-Free Catalysts for Oxygen Reduction Reaction. *Chemical Society Reviews* 2015, **44**, 2168-2201 doi:10.1039/C4CS00484A

11. Seh, Z. W.; Kibsgaard, J.; Dickens, C. F.; Chorkendorff, I.; Nørskov, J. K.; Jaramillo, T. F., Combining Theory and Experiment in Electrocatalysis: Insights into Materials Design. *Science* 2017, **355**, eaad4998 doi:10.1126/science.aad4998

12. Tripković, V.; Skúlason, E.; Siahrostami, S.; Nørskov, J. K.; Rossmeisl, J., The Oxygen Reduction Reaction Mechanism on Pt(111) from Density Functional Theory Calculations. *Electrochimica Acta* 2010, **55**, 7975-7981 doi:https://doi.org/10.1016/j.electacta.2010.02.056

13. O'Hayre, R.; Cha, S. W.; Colella, W.; Prinz, F. B., *Fuel Cell Fundamentals*. Wiley: 2016.

14. Kulkarni, A.; Siahrostami, S.; Patel, A.; Nørskov, J. K., Understanding Catalytic Activity Trends in the Oxygen Reduction Reaction. *Chemical Reviews* 2018, **118**, 2302-2312 doi:10.1021/acs.chemrev.7b00488

15. Abild-Pedersen, F.; Greeley, J.; Studt, F.; Rossmeisl, J.; Munter, T. R.; Moses, P. G.; Skúlason, E.; Bligaard, T.; Nørskov, J. K., Scaling Properties of Adsorption Energies for Hydrogen-Containing Molecules on Transition-Metal Surfaces. *Physical Review Letters* 2007, **99**, 016105 doi:10.1103/PhysRevLett.99.016105

16. Calle-Vallejo, F.; Martínez, J. I.; García-Lastra, J. M.; Rossmeisl, J.; Koper, M. T. M., Physical and Chemical Nature of the Scaling Relations between Adsorption Energies of Atoms on Metal Surfaces. *Physical Review Letters* 2012, **108**, 116103 doi:10.1103/PhysRevLett.108.116103

17. Bligaard, T.; Nørskov, J. K.; Dahl, S.; Matthiesen, J.; Christensen, C. H.; Sehested, J., The Brønsted–Evans–Polanyi Relation and the Volcano Curve in Heterogeneous Catalysis. *Journal of Catalysis* 2004, **224**, 206-217 doi:https://doi.org/10.1016/j.jcat.2004.02.034

18. Stamenkovic, V. R.; Mun, B. S.; Arenz, M.; Mayrhofer, K. J. J.; Lucas, C. A.; Wang, G.; Ross, P. N.; Markovic, N. M., Trends in Electrocatalysis on Extended and Nanoscale Pt-Bimetallic Alloy Surfaces. *Nature Materials* 2007, **6**, 241-247 doi:10.1038/nmat1840

19. Zhao, Z.-J.; Liu, S.; Zha, S.; Cheng, D.; Studt, F.; Henkelman, G.; Gong, J., Theory-Guided Design of Catalytic Materials Using Scaling Relationships and Reactivity Descriptors. *Nature Reviews Materials* 2019, **4**, 792-804 doi:10.1038/s41578-019-0152-x

20. Hammer, B.; Norskov, J. K., Why Gold Is the Noblest of All the Metals. *Nature* 1995, **376**, 238-240 doi:10.1038/376238a0

21. Norsko, J. K., Chemisorption on Metal Surfaces. *Reports on Progress in Physics* 1990, **53**, 1253-1295 doi:10.1088/0034-4885/53/10/001

22. Nørskov, J. K.; Studt, F.; Abild-Pedersen, F.; Bligaard, T., *Fundamental Concepts in Heterogeneous Catalysis: Ch. 8 the Electronic Factor in Heterogeneous Catalysis*. John Wiley & Sons: 2014.

23. Nilsson, A.; Pettersson, L. G. M.; Hammer, B.; Bligaard, T.; Christensen, C. H.; Nørskov, J. K., The Electronic Structure Effect in Heterogeneous Catalysis. *Catalysis Letters* 2005, **100**, 111-114 doi:10.1007/s10562-004-3434-9

24. Hammer, B.; Nørskov, J. K., Theoretical Surface Science and Catalysis—Calculations and Concepts. In *Advances in Catalysis*, Academic Press: 2000; Vol. 45, pp 71-129.

25. Bligaard, T.; Nørskov, J. K., Ligand Effects in Heterogeneous Catalysis and Electrochemistry. *Electrochimica Acta* 2007, **52**, 5512-5516 doi:https://doi.org/10.1016/j.electacta.2007.02.041

26. Nørskov, J. K.; Abild-Pedersen, F.; Studt, F.; Bligaard, T., Density Functional Theory in Surface Chemistry and Catalysis. *Proceedings of the National Academy of Sciences* 2011, **108**, 937 doi:10.1073/pnas.1006652108

27. Gates, B. C.; Knoezinger, H., *Advances in Catalysis: Impact of Surface Science on Catalysis*. Elsevier Science: 2001.

28. Stamenkovic, V.; Mun, B. S.; Mayrhofer, K. J. J.; Ross, P. N.; Markovic, N. M.; Rossmeisl, J.; Greeley, J.; Nørskov, J. K., Changing the Activity of Electrocatalysts for Oxygen Reduction by Tuning the Surface Electronic Structure. *Angewandte Chemie International Edition* 2006, **45**, 2897-2901 doi:10.1002/anie.200504386

29. Kitchin, J. R.; Nørskov, J. K.; Barteau, M. A.; Chen, J. G., Modification of the Surface Electronic and Chemical Properties of Pt(111) by Subsurface 3d Transition Metals. *The Journal of Chemical Physics* 2004, **120**, 10240-10246 doi:10.1063/1.1737365

30. Harrison, W. A., *Electronic Structure and the Properties of Solids: The Physics of the Chemical Bond*. Courier Corporation: 2012.

31. Stephens, I. E. L.; Bondarenko, A. S.; Perez-Alonso, F. J.; Calle-Vallejo, F.; Bech, L.; Johansson, T. P.; Jepsen, A. K.; Frydendal, R.; Knudsen, B. P.; Rossmeisl, J.; Chorkendorff, I., Tuning the Activity of Pt(111) for Oxygen Electroreduction by Subsurface Alloying. *Journal of the American Chemical Society* 2011, **133**, 5485-5491 doi:10.1021/ja111690g

32. Luo, M.; Guo, S., Strain-Controlled Electrocatalysis on Multimetallic Nanomaterials. *Nature Reviews Materials* 2017, **2**, 17059 doi:10.1038/natrevmats.2017.59

33. Ross, P. N., Structure Sensitivity in Electrocatalytic Properties of Pt Ii . Oxygen Reduction on Low Index Single Crystals and the Role of Steps. *Journal of The Electrochemical Society* 1979, **126**, 78 doi:10.1149/1.2128991

34. Ross, P. N., Structure Sensitivity in the Electrocatalytic Properties of Pt I . Hydrogen Adsorption on Low Index Single Crystals and the Role of Steps. *Journal of The Electrochemical Society* 1979, **126**, 67 doi:10.1149/1.2128990

35. Lopes, P. P.; Strmcnik, D.; Tripkovic, D.; Connell, J. G.; Stamenkovic, V.; Markovic, N. M., Relationships between Atomic Level Surface Structure and Stability/Activity of Platinum Surface Atoms in Aqueous Environments. *ACS Catalysis* 2016, **6**, 2536-2544 doi:10.1021/acscatal.5b02920

36. Jacobse, L.; Huang, Y.-F.; Koper, M. T. M.; Rost, M. J., Correlation of Surface Site Formation to Nanoisland Growth in the Electrochemical Roughening of Pt(111). *Nature Materials* 2018, **17**, 277-282 doi:10.1038/s41563-017-0015-z

37. Marković, N. M.; Adžić, R. R.; Cahan, B. D.; Yeager, E. B., Structural Effects in Electrocatalysis: Oxygen Reduction on Platinum Low Index Single-Crystal Surfaces in Perchloric Acid Solutions. *Journal of Electroanalytical Chemistry* 1994, **377**, 249-259 doi:https://doi.org/10.1016/0022-0728(94)03467-2

38. Markovic, N. M.; Gasteiger, H. A.; Ross, P. N., Oxygen Reduction on Platinum Low-Index Single-Crystal Surfaces in Sulfuric Acid Solution: Rotating Ring-Pt(Hkl) Disk Studies. *The Journal of Physical Chemistry* 1995, **99**, 3411-3415 doi:10.1021/j100011a001

39. Hammer, B.; Nielsen, O. H.; Nrskov, J. K., Structure Sensitivity in Adsorption: Co Interaction with Stepped and Reconstructed Pt Surfaces. *Catalysis Letters* 1997, **46**, 31-35 doi:10.1023/A:1019073208575

40. Kondo, S.; Nakamura, M.; Maki, N.; Hoshi, N., Active Sites for the Oxygen Reduction Reaction on the Low and High Index Planes of Palladium. *The Journal of Physical Chemistry C* 2009, **113**, 12625-12628 doi:10.1021/jp904278b

41. Hoshi, N.; Nakamura, M.; Sakata, O.; Nakahara, A.; Naito, K.; Ogata, H., Surface X-Ray Scattering of Stepped Surfaces of Platinum in an Electrochemical Environment: Pt(331) = 3(111)-(111) and Pt(511) = 3(100)-(111). *Langmuir* 2011, **27**, 4236-4242 doi:10.1021/la200199b

42. Attard, G. A.; Brew, A., Cyclic Voltammetry and Oxygen Reduction Activity of the Pt{110}-(1×1) Surface. *Journal of Electroanalytical Chemistry* 2015, **747**, 123-129 doi:https://doi.org/10.1016/j.jelechem.2015.04.017

43. Xin, H.; Linic, S., Communications: Exceptions to the D-Band Model of Chemisorption on Metal Surfaces: The Dominant Role of Repulsion between Adsorbate States and Metal D-States. *The Journal of Chemical Physics* 2010, **132**, 221101 doi:10.1063/1.3437609

44. Schlapka, A.; Lischka, M.; Groß, A.; Käsberger, U.; Jakob, P., Surface Strain Versus Substrate Interaction in Heteroepitaxial Metal Layers: Pt on Ru(0001). *Physical Review Letters* 2003, **91**, 016101 doi:10.1103/PhysRevLett.91.016101

45. Strasser, P.; Koh, S.; Anniyev, T.; Greeley, J.; More, K.; Yu, C.; Liu, Z.; Kaya, S.; Nordlund, D.; Ogasawara, H.; Toney, M. F.; Nilsson, A., Lattice-Strain Control of the Activity in Dealloyed Core–Shell Fuel Cell Catalysts. *Nature Chemistry* 2010, **2**, 454-460 doi:10.1038/nchem.623

46. Escudero-Escribano, M.; Malacrida, P.; Hansen, M. H.; Vej-Hansen, U. G.; Velázquez-Palenzuela, A.; Tripkovic, V.; Schiøtz, J.; Rossmeisl, J.; Stephens, I. E. L.; Chorkendorff, I., Tuning the Activity of Pt Alloy Electrocatalysts by Means of the Lanthanide Contraction. *Science* 2016, **352**, 73 doi:10.1126/science.aad8892

Chapter 2. Differential Surface Elemental Distribution Leads to Significantly Enhanced Stability of PtNi-based ORR Catalysts

2.1 Introduction

Alloying Pt with transition metals is a widely adopted approach to address the performance challenge of Pt-based electrochemical catalysts. A variety of structures and compositions of Pt-based alloy catalysts has been studied.[1-5] To date, the best ORR specific activity (SA, activity normalized by electrochemical surface area (ECSA)) is achieved on $Pt_3Ni(111)$ single crystal surface, which shows about 18 mA/cm^2_{Pt} and is about 90 times more active than commercial Pt/C.[6] Stimulated by this finding, intensive research has been focused on developing nanocatalysts that approach the specific activity established on the $Pt_3Ni(111)$ single crystal surface, as nanoscale catalysts hold the advantage of high mass activity (activity normalized by Pt mass loading) due to their high ECSA.[7-15] With exposed (111) facets, Pt-Ni octahedral nanoparticles can reach drastically improved activity compared to commercial Pt/C catalysts, although challenges remained with regard to the poor stability.[11-12] To further improve the activity as well as the stability of octahedral Pt-Ni nanomaterials, introducing a third element to form a ternary alloy or surface doping modification has been explored.[16-21] Reported Mo-Pt_3Ni, PtRhNi, PtNiCu, Ga-PtNi, and PtNiCo octahedral nanoparticles showed enhanced stability and/or activity compared to binary octahedral PtNi catalysts.[16-20, 22-23] Studies to date have suggested possible mechanisms that the third element contributes to the enhanced stability, including lowering surface Pt diffusion/mobility,[17, 24] and stabilizing Ni by suppressing the Ni dissolution.[23]

Herein, we report the synthesis of octahedral PtNiCu nanoparticles with well-controlled octahedral morphology and uniform dispersity on carbon support in solution (details about synthesis are included in Supplementary Information). To the best of our knowledge, this is the

first time octahedral PtNiCu nanoparticles are prepared via solution phase synthesis route. These PtNiCu nanocatalysts demonstrated improved activity and stability compared to PtNi of similar size and similar Pt-composition, as ORR catalysts. The kinetic growth pathway of the PtNi and PtNiCu nanoparticles was recorded, and their respective size and composition at several time points were carefully analyzed. It was clear from the experiments that adding Cu changes the growth behavior of these nano octahedral particles. In addition, a strong correlation between the initial differential Pt/Ni/Cu element distribution and the resultant varied stability was observed by comparing PtNi and PtNiCu in ORR performance.

To understand the reason for the enhanced properties of PtNiCu nanoparticles, we have used atomic-scale computational modeling. As the cores of the nanoparticles are likely kinetically trapped in their as-synthesized structures[22], it is necessary to use kinetic modeling to determine the atomic-scale structures of the particles after electrochemical cyclic voltammetry (CV) activation. Here we go beyond previous efforts to model the thermodynamic equilibrium[18, 25-26] or kinetic evolution[22, 27-28] of alloy nanoparticles by using time-tracking experiments to determine the initial composition profile of the particles and using a cluster-expansion[29-30] energy model trained on density functional theory (DFT)[31] calculations in kinetic Monte Carlo (KMC)[32-33] simulations to determine the structures of the nanoparticles after activation. Evaluation of the rationally initialized KMC simulation for PtNi and PtNiCu particles reveals the origins of the highly enhanced durability of the PtNiCu particles at the atomic level: the higher Pt surface fraction reduces the number of surface vacancies created in the early stage of CV activation, which in turn reduces the opportunity for atoms in sub-surface layers to move to the surface and dissolve.

2.2 Methods

2.2.1 Experimental Methods

Materials and Chemicals

Platinum(II) acetylacetonate [$Pt(acac)_2$], nickel(II) acetylacetonate [$Ni(acac)_2$], nickel(II) acetate tetrahydrate [$Ni(Ac)_2 \cdot 4H_2O$], copper(II) acetate monohydrate [$Cu(Ac)_2 \cdot H_2O$], benzyl acid (BA) were purchased from Sigma Aldrich. Pt/C (20% Pt), molybdenum hexacarbonyl ($Mo(CO)_6$) were purchased from Alfa Aesar. N, N-Dimethylformamide (DMF), acetone, isopropanol were purchased from Fisher Scientific. Ethanol was purchased from Decon Labs, Inc. Vulcan XC-72 carbon black (particle size ~50 nm) was from Cabot Corporation. Water used was Ultrapure Millipore (18.2 MΩ·cm).

Preparation of Octahedral PtNiCu/C

20 mg Vulcan XC-72 carbon black was dispersed in 9 mL DMF under ultrasonication for 30 mins in a 25 ml vial. Then 9 mg $Pt(acac)_2$, 4.5 mg $Ni(ac)_2 \cdot 4H_2O$, and 1.5 mg $Cu(ac)_2 \cdot H_2O$, 65 mg benzoic acid were dissolved in 1 ml DMF and were also added into the 25 ml vial with carbon black dispersion. After ultrasonication for 5 mins, the vial with the well-mixed solution was directly put into 140 ºC oil bath and then slowly heated to 160 ºC. The vial was then kept at 160 ºC for 12 hours (hrs).

After 12 hrs, 1 mg $Pt(acac)_2$, 0.5 mg $Ni(ac)_2 \cdot 4H_2O$, 0.5 mg $Cu(ac)_2 \cdot H_2O$ were dissolved in 0.5 mL DMF and was added into the vial. Then the vial was kept in 170 ºC oil bath for 48 hrs. After the reaction finished, the catalysts were collected by centrifugation, then dispersed and washed with isopropanol and acetone mixture. Then the catalysts were dried in vacuum at room temperature and ready for characterization and electrochemistry test.

Preparation of Octahedral PtNi/C

20 mg Vulcan XC-72 carbon black was dispersed in 9 mL DMF under ultrasonication for 30 mins in a 25 ml vial. Then 9 mg $Pt(acac)_2$, 7.2 mg nickel(II) acetylacetonate [$Ni(acac)_2$], and 85 mg benzoic acid were dissolved in 1 ml DMF and were also added into the 25 ml vial with carbon black dispersion. After ultrasonication for 5 mins, the vial with the well-mixed solution was directly put into 140 ºC oil bath and then slowly heated to 150 ºC. The vial was then kept at 150 ºC for 12 hrs.

After 12 hrs, 1 mg $Pt(acac)_2$, 0.8 mg $Ni(acac)_2$ were dissolved in 0.5 mL DMF and was added into the vial. Then the vial was kept in 150 ºC oil bath for 48 hrs. After the reaction finished, the catalysts were collected by centrifugation, then dispersed and washed with isopropanol and acetone mixture. Then the catalysts were dried in vacuum at room temperature and ready for characterization and electrochemistry test.

Structure and Composition Characterization

Transmission electron microscopy (TEM) images were taken on an FEI T12 transmission electron microscope operated at 120 kV. Atomic resolution scanning transmission electron microscopy (STEM) images and energy-dispersive spectroscopy (EDS) line scan were taken on a JEOL Grand ARM300CF TEM/STEM operated at 300 kV. High angle annular dark field (HAADF) scanning transmission electron microscopy (STEM) images were also taken on an FEI TITAN operated at 200 kV. The samples were prepared by dropping ethanol dispersion of samples onto carbon-coated aluminum TEM grids (Ted Pella, Redding, CA) using pipettes and dried under ambient condition. X-ray powder diffraction patterns were collected on a Panalytical X'Pert Pro X-ray Powder Diffractometer with Cu-Kα radiation. The concentration of catalysts was determined by inductively coupled plasma atomic emission spectroscopy (ICP-AES, Shimadzu ICPE-9000) as well as EDS coupled in ZEISS Supra 40VP scanning electron microscope (SEM).

Electrode Preparation and Electrochemistry Test

A typical catalyst ink was prepared by mixing 2.6 mg of catalyst powder (octahedral, PtNiCu/C, PtNi/C) with a 2 ml ethanol solution containing 20 μL Nafion (5 wt%) with 5 min ultrasonication time. Then, 10 μL of catalyst ink was dropped onto a 5 mm diameter glassy-carbon electrode (Pine Research Instrumentation). Estimation of Pt loading is based on overall Pt ratio within catalyst determined by ICP-AES, and Pt loading is about 1.9 μg for all tested Pt-based alloy samples. The ink was dried under an infrared lamp; then the electrode was ready for the electrochemical test. Commercial Pt/C catalyst was used as the baseline catalysts, and similar procedure as described above was used to conduct the electrochemical measurement. Pt loading is about 1.3 μg for commercial Pt/C.

A three-electrode cell was used to carry out the electrochemical measurements. The working electrode was a catalyst coated glassy carbon electrode. An Ag/AgCl electrode was used as the reference electrode. Pt wire was used as the counter electrode. Cyclic Voltammetry (CV) measurements were conducted in an N_2 saturated 0.1 M $HClO_4$ solution between 0.05 to 1.1 V vs. reversible hydrogen electrode (RHE) at a sweep rate of 100 mV/s. Oxygen reduction reaction (ORR) measurements were conducted in an O_2 saturated 0.1 M $HClO_4$ solution between 0.05 to 1.1 V vs. RHE at a sweep rate of 20 mV/s. Accelerated degradation test (ADT) was performed in oxygen saturated 0.1 M $HClO_4$ solution by applying CV sweeps between 0.6 to 1.0 V vs. RHE at a sweep rate of 100 mV/s. For the CO stripping voltammetry measurements, working electrodes coated with different catalysts were firstly immersed in a CO-saturated 0.1 M $HClO_4$ solution up to 1.5 min, and then the CO stripping voltammetry was recorded respectively in N_2 saturated 0.1 M $HClO_4$ between 0.05 to 1.1 V vs. RHE at a sweep rate of 25 mV/s.

2.2.2 Computational Methods

Cluster Expansion Methodology

The Pt-Ni-Cu-Vacancy cluster expansion, which is able to predict the energies of nanoparticles as a function of shape, size, and internal atomic order, is built using a similar approach to build the Pt-Ni-Mo-Vacancy cluster expansion[18, 22, 26]. The details of the developed Pt-Ni-Cu-Vacancy cluster expansion are provided as follows.

For the generation of training data, we reused all training structures that do not contain Mo atoms from the Pt-Ni-Mo-Vacancy cluster expansion (removing the training structures containing Mo atoms). We created additional 42 random Pt-Cu particles and 54 random Pt-Ni-Cu particles using the same approach that the 74 random Pt-Ni nanoparticles were generated[18]. All nanoparticles were generated under the constraint that there had to be more than 85 total atoms in the nanoparticle, as the inclusion of smaller particles was found to lead to cluster expansions with poor predictive accuracy for multi-nanometer nanoparticles (probably due to quantum size effects). Nanoparticles that experienced significant reconstruction upon relaxation, defined as an atom traveling more than 75% the nearest-neighbor distance from its initial site, were excluded. All nanoparticles were contained in a cubic cell with a lattice parameter of 28.8 Å. The resulting set of random nanoparticles included 74 Pt-Ni nanoparticles and 42 Pt-Cu nanoparticles, and 54 Pt-Ni-Cu nanoparticles. In addition to these structures, the training data consisted of the pure elements Cu, Ni, and Pt in a bulk fcc crystal, vacuum (a lattice containing only vacant sites), and various low-energy structures predicted over the course of this research, for a total of 346 unique structures. These 346 training structures included 143 Pt-Ni-Cu nanoparticles, 119 Pt-Ni nanoparticles, 77 Pt-Cu nanoparticles, 3 pure Pt nanoparticles, 1 Pt bulk, 1 Ni bulk, 1 Cu bulk, and 1 vacuum structure. To reduce the prediction error of the cluster expansion, the pure elements and vacuum were

included twice in the training set[34]. The effective cluster interactions (ECIs) of the cluster expansions were fit to the DFT-calculated formation energies of fully relaxed nanoparticles relative to the reference states of bulk fcc Cu, Ni, and Pt.

The cluster expansion was truncated to include the empty cluster, the one-body (point) cluster, all 2-body clusters up to the seventh-nearest neighbor, all 3-body clusters up to the fifth-nearest neighbor, all 4-body clusters up to the third-nearest neighbor, and 5-, and 6-body clusters up to the second-nearest neighbor, for a total of 1302 symmetrically distinct cluster functions. The ECIs for these cluster functions were fit to the training data using the Bayesian approach with a multivariate Gaussian prior distribution[35]. The inverse of the covariance matrix for the prior, Λ, was diagonal, with elements given by

$$\lambda_{\alpha\alpha} = \begin{cases} 0 & \text{for } \mathrm{n}_\alpha = 0 \\ \lambda_1 & \text{for } \mathrm{n}_\alpha = 1, \\ \lambda_2 (1 + r_\alpha)^{\lambda_3} e^{\lambda_4 n_\alpha} & \text{for } \mathrm{n}_\alpha > 1 \end{cases}$$

where n_α is the number of sites in cluster function α, r_α is the maximum distance between sites, and the parameters λ_1, λ_2, λ_3, and λ_4 were determined by using a conjugate gradient algorithm to minimize the root mean square leave-one-out cross validation (RMS LOOCV) score, an estimate of prediction error[36]. The final values for these parameters were 1.000×10^{-8}, 9.413×10^{-9}, 4.343, and 2.977, respectively. The resulting cluster expansion had an RMS LOOCV error of 3.0 meV per atom relative to DFT calculations.

Metropolis Monte Carlo Simulations

To enable comparison with experimental results and limit the effects of particle size on the predictions of the atomic configuration of PtNi and PtNiCu particles, we have used slightly truncated 6175-atom octahedral nanoparticles (missing only the outermost atoms on each vertex)

with an edge length of approximately 4.8 nm as prototypical particles for Monte Carlo simulations. To predict the atomic structures under thermodynamically stable states, we have run cluster-expansion-based Metropolis Monte Carlo simulations on PtNi and PtNiCu nanoparticles with before-activation composition profiles.

Kinetic Monte Carlo Simulations

The activation process of octahedral PtNi/C and PtNiCu/C nanoparticles has been done at room temperature (about 298 K), which is likely too low for particles to reach equilibrium based on our previous work on octahedral PtNi nanoparticles[22]. The core of the particles is likely kinetically trapped in an as-synthesized metastable state (the synthesis temperature is about 443 K, which is also too low to reach equilibrium during synthesis). Thus, to better understand the structure of the activated particles, we have developed a simple kinetic Monte Carlo (KMC) model of particle evolution in oxidizing conditions based on the Pt-Ni-Cu-Vacancy cluster expansion developed in section 2.1, similar to our previous work[22]. Because the shape of the nanoparticle can change in these simulations, we have updated our estimates of the energetic effects of oxidation (ΔG(*OH), introduced in the work of Pt-Ni-Mo-Vacancy nanoparticles[26]) to account for a greater variety of coordination environments. For Cu atoms on the surface, we found that adsorbed OH (*OH) is more stable than the adsorbed O. Specifically, we have done the following:

(1) We determine the coordination number of Pt/Ni/Cu sites by counting the number of nearest-neighbor sites that are occupied by Pt/Ni/Cu and for which the next-nearest site in the same direction is also occupied. By requiring both sites to be occupied, we effectively distinguish between surface sites (with room for adsorbates) and vacancies in bulk.

(2) For coordination numbers of 3, 4, 6, 7, and 9, we use DFT calculations to estimate ΔG, the extent to which OH adsorption (for Pt, Ni, and Cu) stabilizes the site on the surface at an applied potential of 0.95 V vs. the reversible hydrogen electrode.

(3) The DFT calculations of adsorbed *OH on the surface of nanoparticles were done in vacuum. To account for the presence of a solvent, we adjusted the free energy of adsorbed *OH by adding –0.6 eV per adsorbed molecule, based on the solvation correction value determined by Norskov et al.[37]

(4) For coordination numbers not included in our DFT calculations, we use linear interpolation to estimate the value of ΔG.

(5) We have found that the first OH adsorbed on the surface of the prototypical particle binds more strongly than subsequent OH, due to the excess surface electrons of the particle in vacuum. Our DFT calculations indicate that the difference between the change in free energy (ΔG(*OH)) for the first adsorbed OH and subsequently adsorbed OH (second, third, fourth, and etc.) is –0.391 eV on Pt, –0.352 eV on Ni, and –0.267 eV on Cu. To better model a situation in which multiple OH are adsorbed on nanoparticles, we apply these corrections to the single-OH values calculated on the prototypical particle in step (2) when determining ΔG(*OH).

(6) We set the value of ΔG(*OH) to be zero if it is larger than zero (ΔG(*OH)>0), to indicate that no *OH adsorbs on that surface site.

2.3 Results and Discussion

Structure of Octahedra nanoparticles

The synthesized PtNi and PtNiCu nanoparticles showed well-controlled octahedral morphology and uniform distribution on carbon black support, as shown in transmission electron

microscopy (TEM) images (Figure 2.1). The edge lengths of the resultant octahedral PtNi and PtNiCu are comparable (5.0 ± 0.6 nm for PtNi and 4.9 ± 0.6 nm for PtNiCu, as shown in Figure 2.1).

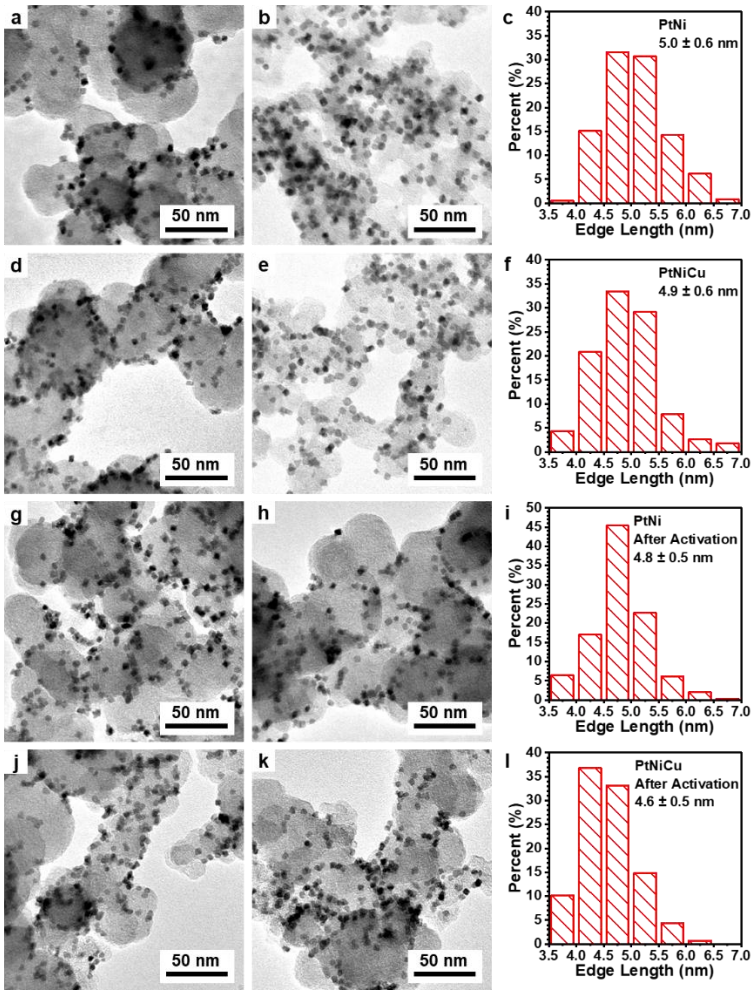

Figure 2. 1. TEM images of octahedral nanostructures on carbon support (a, b) PtNi and corresponding edge length distribution (c); (d, e) PtNiCu and corresponding edge length distribution (f); PtNi after activation (g, h) and corresponding edge length distribution (i); PtNiCu after activation (j, k) and corresponding edge length distribution (l). Adapted with permission from Ref.[38] Copyright 2019 Elsevier.

Powder X-ray diffraction (XRD) spectra show the atomic packing for these PtNi and PtNiCu alloy are face center cubic (fcc) packing with a lattice parameter of 0.379 nm (Figure 2.2a), indicating the same Pt ratio in these two alloys. Atomic resolution scanning transmission electron microscopy (STEM) images revealed the (111) interplanar distances of the alloy PtNi and PtNiCu

nanoparticles were 0.219 nm (Figure 2.2b, c). The lattice parameters based on STEM match well with those based on XRD spectra. These observations confirm that PtNi and PtNiCu were prepared with comparable morphology, size, Pt ratio, and lattice, leaving the only difference between octahedral PtNi and PtNiCu to the Cu and Ni content.

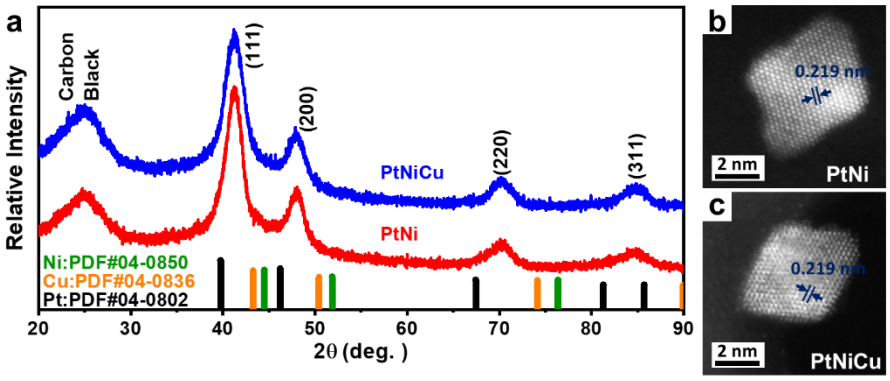

Figure 2. 2. Characterization of octahedral PtNi and PtNiCu nanoparticles. (a) XRD spectra of octahedral PtNi/C, and PtNiCu/C (vertical lines represent standard XRD peak positions: black for Pt (PDF #04-0802), green for Ni (PDF #04-0850), and blue for Cu (PDF #04-0836)). Atomic resolution STEM images of octahedral (b) PtNi, and (c) PtNiCu nanoparticles. Adapted with permission from Ref.[38] Copyright 2019 Elsevier.

Electrochemical Evaluation in RDE testing

The electrochemical performance of the octahedral PtNiCu was studied in comparison of PtNi. CV curves were recorded for commercial Pt/C, octahedral PtNi and PtNiCu (Figure 2.3a), in N_2 saturated 0.1 M $HClO_4$ after CV activation (30 CV cycles for PtNi/C and PtNiCu/C, and 60 CV cycles for Pt/C). Electrochemical surface area (ECSA) was determined by integrating hydrogen underpotential deposition (H_{upd}) charge (H_{upd} charge to surface area conversion constant: 210μC/cm^2). ORR polarization curves were recorded in O_2 saturated 0.1 M $HClO_4$ (Figure 2.3b). The comparison of the above tests showed the mass activity (MA), and specific activity (SA) of octahedral PtNiCu/C were higher than those of octahedral PtNi (Figure 2.3c). The octahedral PtNiCu showed 15.9 times SA and 13.2 times MA compared to commercial Pt/C. To study the

stability of catalysts, the above octahedral nanoparticles were tested in O_2 saturated 0.1 M $HClO_4$ for 30000 CV cycles for an accelerated durability test (ADT). Octahedral PtNiCu showed 69.3% MA retention, which was significantly enhanced compared to 49.4% MA retention of octahedral PtNi (Figure 2.3d). The stability of PtNiCu/C exceeds the U.S. DOE[39] target of fuel cell catalyst stability (less than 40% MA loss after 30000 CV cycles). Interestingly, significant composition change was observed for octahedral PtNi and PtNiCu after CV activation and ADT based on energy dispersive spectroscopy (EDS) analysis. After CV activation, the atomic Ni ratio in octahedral PtNi decreased from 34.5% to 15.2% (Figure 2.3e). In octahedral PtNiCu, Ni was reduced from 16.8% to 12.7%, Cu was reduced from 16.9% to 14.6%, and the total (Ni+Cu) was reduced from 33.7% to 27.3% (Figure 2.3f). It was found that relatively more Cu was retained within the octahedral PtNiCu compared to Ni, consistent with the fact that Cu is more inert than Ni based on their reduction potentials[40] (Table S5). The overall fraction of Cu and Ni after activation for PtNiCu is 27.3%, which was significantly higher than 15.2% for PtNi. As the electrochemical cycling continues, after ADT (30000 CV cycles), octahedral PtNiCu still maintained 11.9% Cu and 5.5% Ni (total 17.4% Cu and Ni) while octahedral PtNi only maintained 6.3% Ni.

These experimental observations suggest that Ni dissolution can be significantly reduced by the presence of Cu. It was also clear that with the presence of Cu, the electrochemical performance of octahedral PtNiCu/C was significantly improved compared with octahedral PtNi/C. In order to understand the fundamental mechanism of these improvements, we carried out theoretical simulations on octahedral PtNi and PtNiCu nanoparticles with the experimentally observed Pt/Ni/Cu compositions and particle size (with edge lengths of approximating 4.8 nm). As the elemental distribution in a Pt-alloy nanocatalyst may differ significantly from a typical

particle in thermodynamic equilibrium[22], we have used *ab-initio* kinetic models initialized according to experimental growth tracking analysis to closely determine the distributions of the elements within the PtNi and PtNiCu nanoparticles.

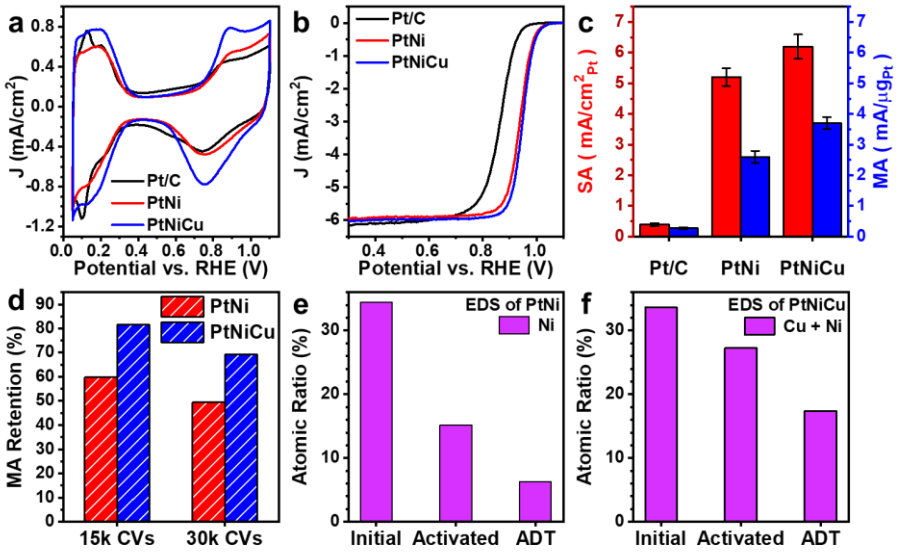

Figure 2. 3. RDE electrochemical evaluation and composition analysis of octahedral PtNi and PtNiCu nanoparticles. (a) CV curves measured in N_2 saturated 0.1 M $HClO_4$ with scan rate 100 mV/s, (b) ORR polarization curves measured in O_2 saturated 0.1 M $HClO_4$ with scan rate 20 mV/s, (c) SA and MA along with the error bars representing standard deviations. (d) Comparison of MA retention between PtNi/C and PtNiCu/C. EDS composition analysis of the atomic fraction of Ni and Cu at initial stage, after CV activation, and after ADT for (e) PtNi/C, and f) PtNiCu/C. Adapted with permission from Ref.[38] Copyright 2019 Elsevier.

Growth Tracking Analysis for Layer-by-layer Composition

The growth tracking of the nanoparticle from six to sixty hours was used as the basis to calculate the initial layer-by-layer compositions of PtNi and PtNiCu nanoparticles for KMC simulations. With the aid of EDS as well as TEM, growth tracking experiments unveiled the composition evolution accompanied by octahedral size growth (Figure 2.4).

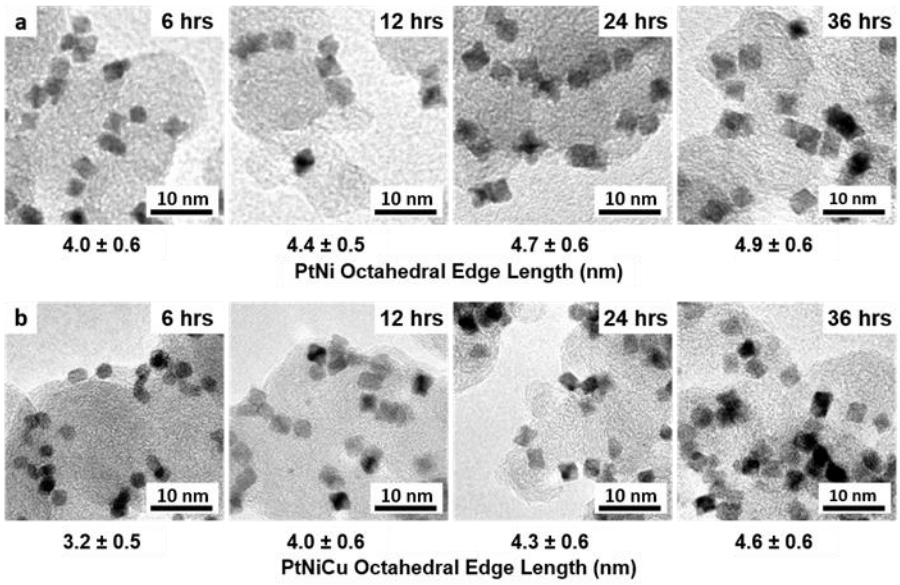

Figure 2. 4. Growth tracking of octahedral edge length based on TEM images of (a) PtNi/C, (b) PtNiCu/C.

For PtNi nanoparticles, the atomic percent of Ni continuously increased from 28.7% to 34.5% (all compositions are atomic percent if without a specific note), while the atomic percent of Pt decreased from 71.3% to 65.5% from six hours to 60 hours (Figure 2.5a). In contrast to PtNi, PtNiCu nanoparticles comprised of 64.1% Pt, 31.2% Cu, and only 4.7% Ni, after six hours of reaction. At 12 hours, the Cu fraction decreased to 21.4% while the Ni fraction increased to 16.1%. After 24 hours, Cu and Ni were nearly equal (Figure 2.5b). The growth tracking of the composition indicated that Cu played a vital role at the early stage of the nanoparticle nucleation and growth. The reduction rate of Cu was much faster than Ni during the reaction, resulting in a much higher atomic fraction of Cu (31.2%) than that of Ni (4.7%) at 6 hours. Both octahedral PtNi (4.0 ± 0.6 to 5.0 ± 0.6 nm) and PtNiCu (3.2 ± 0.5 to 4.9 ± 0.6 nm) showed continuous nanoparticle size growth from 6-60 hours (Figure 2.5a, b), with the difference that PtNiCu nanoparticle showed a smaller size at early growth stage compared to PtNi possibly due to faster nucleation rates in the presence of Cu. Moreover, for PtNi, the growth tracking experiment showed that the overall Ni fraction continued to increase during the growth process; while in PtNiCu the overall (Ni+Cu)

fraction slightly decreased from 12 hours to 60 hours. This observation indicates that PtNi nanoparticles may show a lower Pt ratio on the surface than PtNiCu, given that both have similar overall Pt ratios at 60 hours.

To account for this significant difference of the surface elemental distributions at different reaction times during the synthesis, we calculated the layer-by-layer composition profiles from the core to the surface of particles following the timeline of the growth process (Figure 2.5a, b). The step-by-step calculations are as follows (taking the PtNi nanoparticle as an example): (1) According to growth tracking of the PtNi particle (**Fig. 2**a**),** during the time interval from t=0 hours (hrs) to t=6 hrs, the layers deeper than the 2nd layer have grown; from t=6 hrs to t=12 hrs, the 2nd layer has grown; from t=12 hrs to t=60 hrs, the 1st layer has grown. (2) We used the overall composition at t=6 hrs to set the composition of the core layers (deeper than the 2nd layer). (3) From t=6 hrs to t=12 hrs, the 2nd layer has grown. We used the overall composition at 12 hrs and the composition of the core layers (from step (2)) to derive the composition in the 2nd layer. (4) Similarly, we used the overall compositions at 60 hrs, the compositions of the core layers, and the composition of the 2nd layer to derive the composition in the 1st layer.

The initial composition profile of the PtNiCu nanoparticle has been calculated in a similar way. As a result, we found that the Pt fraction in the PtNiCu particle is about 14.3% higher in the 1^{st} layer, and 8.5% higher in the 2^{nd} layer than in PtNi. To further validate our approach, we generated EDS maps for PtNi and PtNiCu nano-octahedra. The obtained EDS maps show observable amounts of Ni over Pt on the surface for both PtNi and PtNiCu octahedra (Figure 2.5g-j). The EDS maps further reveal that the distribution of Cu is more concentrated in the core of the nanoparticles than Ni is (Figure 2.5h, j), which is consistent with our composition results obtained via growth tracking and the layer-by-layer composition profiles we constructed (Figure 2.5b, d, f).

In contrast, Metropolis Monte Carlo[41] simulations predict that in thermodynamic equilibrium almost all Cu atoms (99.6%) in the PtNiCu nanoparticle segregate to the second layer, the first and third layers are nearly pure (>96%) Pt and most of Ni atoms are in the core below the third layer. These results suggest that due to the relatively low temperature (150-170 ºC) of the particle growth process, the particles are not in equilibrium and the cores are trapped in a metastable state (Figure 2.5), similar to our observations on other Pt-Ni-based nanoparticles.[22] Thus, for consistency with experimental characterization, we initialized the nanoparticle structures for our KMC simulations by creating nearly-octahedral nanoparticles (with six vertex atoms removed) with 21 (111) layers and randomly distributing Ni and Cu atoms in each layer based on the derived layer-by-layer composition profiles (Figure 2.5e, f).

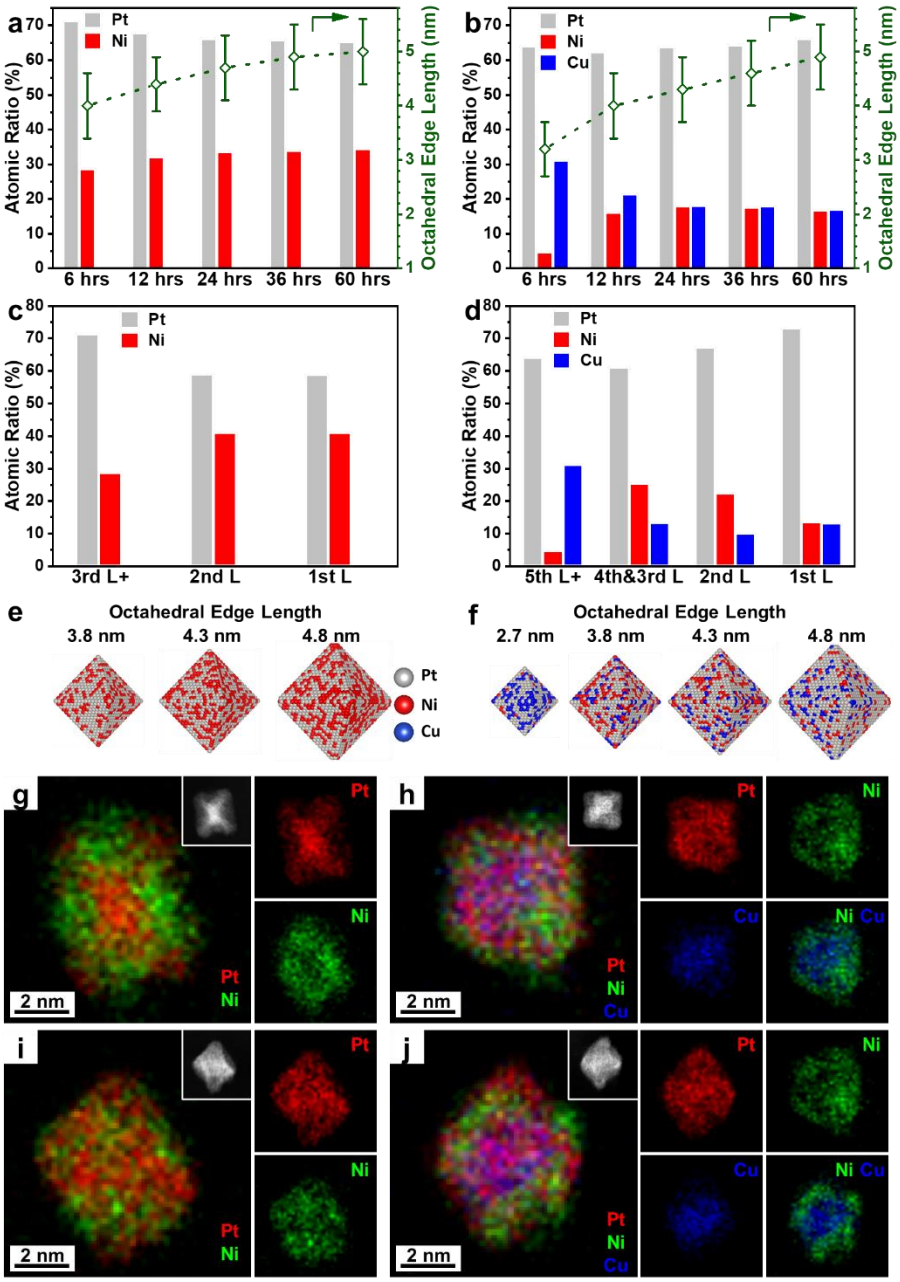

Figure 2. 5. Growth tracking study and simulation model construction. Growth tracking of atomic ratio based on EDS and octahedral edge length based on TEM image for (a) PtNi, and (b) PtNiCu particles. Error bars represent standard deviations. Layer by layer nano octahedron model construction based on growth tracking for (c) PtNi, and (d) PtNiCu. The scheme for the growth of randomly initialized (e) PtNi, and (f) PtNiCu nanoparticles based on (c) and (d) to mimic the increasing octahedral size and various Pt/Ni/Cu compositions during growth. EDS map of octahedral nanoparticles of two representative PtNi (g, i), two representative PtNiCu (h, j) nanoparticles. The left side of each panel shows the map of all elements overlapped, while the right side of the panel exhibits the map of a single element or Ni+Cu overlapped. The insert panel shows the STEM image of the mapped nanoparticle. Adapted with permission from Ref.[38] Copyright 2019 Elsevier.

To determine the structure of particles after activation, we performed KMC simulations of particle evolution in oxidizing conditions (0.95 V vs. RHE) based on a cluster expansion trained on DFT calculations. The KMC simulations show a rapid loss of Ni and Cu from the near-surface sites in the early stage, followed by a steadier concentration profile (Figure 2.6). We stopped the KMC runs when Ni and Cu compositions reached plateaus (insets of Figure 2.6). Snapshots of the resultant particles after Ni and Cu dissolution are shown in Figure 2.7b and e, respectively. The octahedral shape of both PtNi and PtNiCu particles still holds after KMC runs, in agreement with the experiments (Figure 2.1g, h, j, k). After the KMC runs, the Ni (Cu) fraction in the PtNiCu particle (Figure 2.7f) drops from 16.8% (16.9%) to 12.2% (14.7%) which is close to the experimental values of 12.7% (14.6%) for activated particles. In the PtNi particle (Figure 2.7c), the Ni fraction drops from 34.5% to 21.4%, compared to 15.2% Ni in experiments. In both simulations and experiments, there was considerably less Ni and (Ni+Cu) loss in the PtNiCu particle than in the PtNi particle.

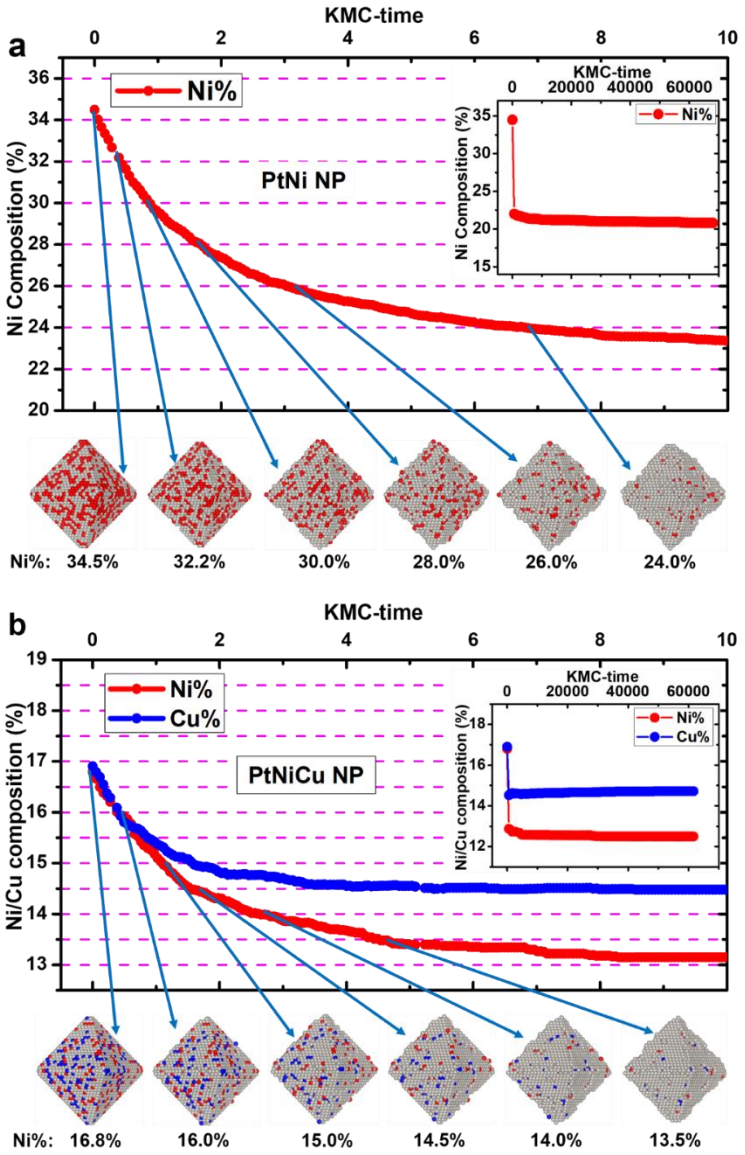

Figure 2. 6. Ni and Cu compositions of PtNi and PtNiCu during KMC runs. The large graphs show Ni and Cu compositions of (a) PtNi and (b) PtNiCu nanoparticles as a function of KMC time for representative KMC runs. Snapshots of the nanoparticle structures are on the bottom row. The insets are the Ni and Cu compositions over the course of the entire KMC simulation. Adapted with permission from Ref.[38] Copyright 2019 Elsevier.

In both particles, the Ni and Cu atoms in the outermost layer dissolve from the particles early in the KMC simulation (Figure 2.6). For the PtNi particle, about 64.4% of Ni in the second layer is lost to dissolution, while for PtNiCu much less (Ni+Cu) content (only about 14.2%) is lost. This leads to a larger fraction of 3d transition metals in the second layer of the PtNiCu nanoparticle (33.7%) compared with the PtNi nanoparticle (25.6%). These results indicate that the amount of

near-surface dissolution is more significant in PtNi nanoparticles than in PtNiCu nanoparticles, suggesting that introduced Cu suppresses the dissolution of subsurface Ni and Cu. The decreased platinum content in the second layer likely contributes to the enhanced activity of the PtNiCu nanoparticles, as previous work has indicated that PtNi nanoparticles bind oxygen too strongly on average[22, 42] and the oxygen binding energy can be reduced by decreasing the Pt content in the second layer[43]. The strain effect also likely contributes to the observed differences in catalytic activity, as the greater fraction of relatively small Ni and Cu atoms in the activated PtNiCu particles will act to reduce surface Pt-Pt bond length, further contributing to relatively weaker oxygen binding energy and higher ORR activity.[22, 43-45]

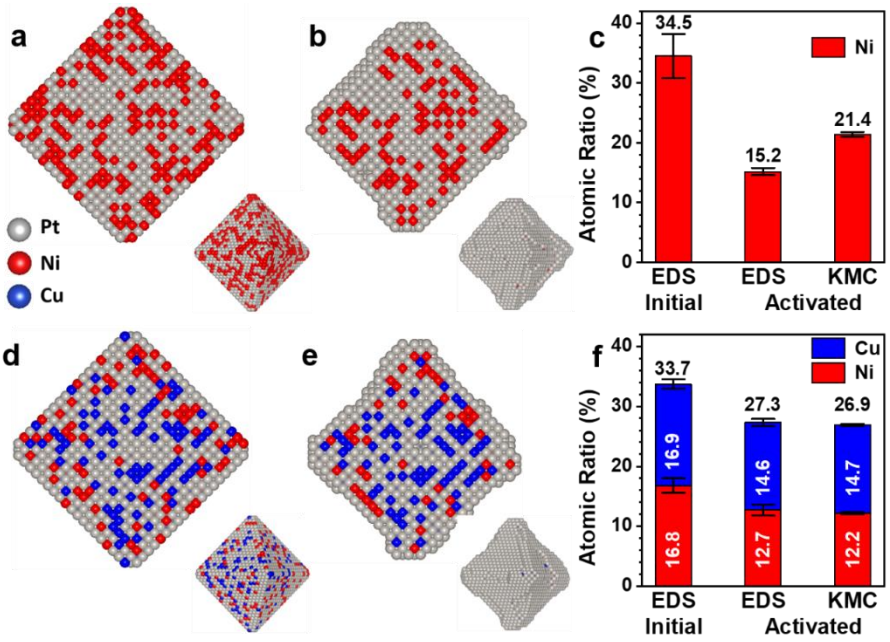

Figure 2. 7. Ni and Cu compositions of PtNi and PtNiCu during KMC runs. The large graphs show Ni and Cu compositions of (a) PtNi and (b) PtNiCu nanoparticles as a function of KMC time for representative KMC runs. Snapshots of the nanoparticle structures are on the bottom row. The insets are the Ni and Cu compositions over the course of the entire KMC simulation. Adapted with permission from Ref.[38] Copyright 2019 Elsevier.

To better understand the reason for the enhanced stability of PtNiCu nanoparticles, we tracked the movement of individual atoms in KMC simulations (Figure 2.8). It was found that in both PtNi and PtNiCu, there is almost no diffusion of atoms that were deeper than the fourth layer,

consistent with a kinetically trapped structure. As our KMC simulations likely overestimate the relative rates at which highly-coordinated atoms hop, it is likely that there is even less inter-layer migration for atoms in sub-surface layers than our simulations show.

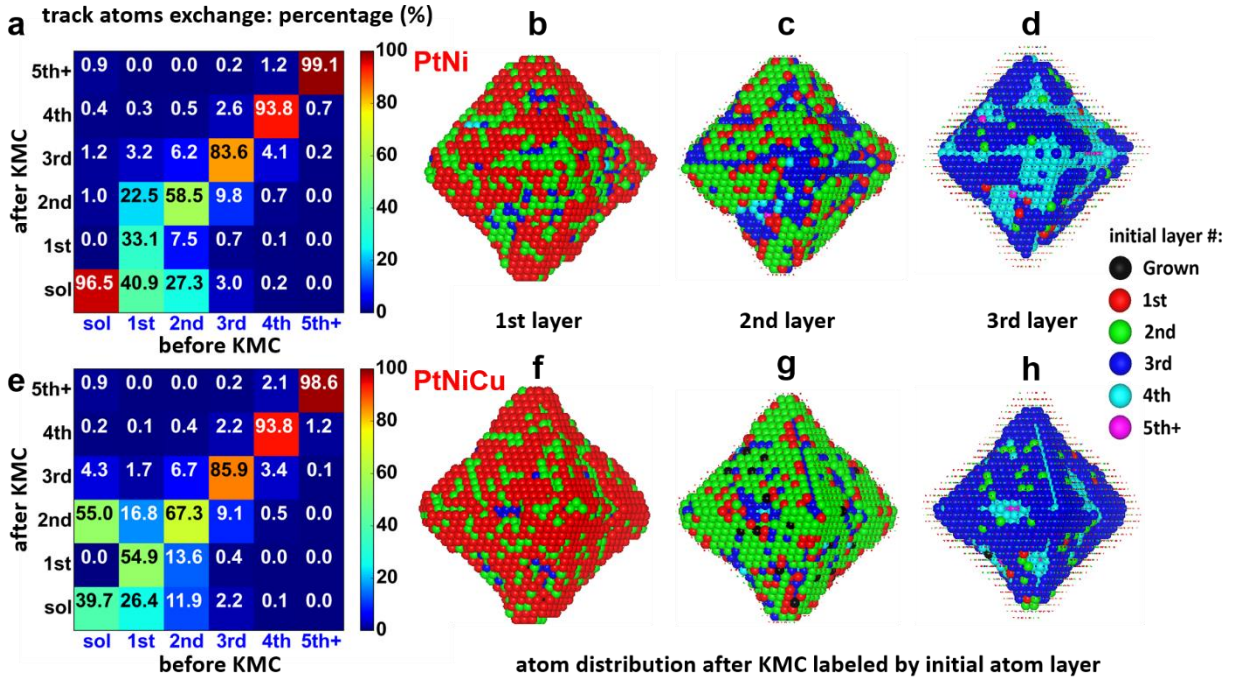

Figure 2. 8. The tracking of the movement of individual atoms during KMC simulations for PtNi and PtNiCu. Atomic tracking results for (a-d) PtNi and (e-h) PtNiCu nanoparticles. In (a) and (e) the x-axis gives the initial layers before KMC, the y-axis gives the final locations after KMC for each atom, and "sol" indicates the solution. The color scheme indicates average percentages of atoms in the initial layer moved to the final layer (from red indicating 100% to navy indicating 0%). It is clear that a higher percentage of atoms stayed in the initial layers (i.e., same initial and final layers, along the diagonal of the table) in PtNiCu than in PtNi. (b-d) and (f-h) show the initial layers of atoms that ended up in the first (b, f), second (c, g), and third (d, h) layers of representative snapshots after KMC runs. The black spheres mean that the atoms were created through growth events. Adapted with permission from Ref.[38] Copyright 2019 Elsevier.

Overall, more atoms are retained in their initial layers in the PtNiCu nanoparticle (e.g., 54.9% in the first layer) than in the PtNi nanoparticle (e.g., 33.1% in the first layer), suggesting decreased diffusivity. It is also observed that more atoms that are initially in sub-surface layers are exposed to the surface in PtNi nanoparticles than in PtNiCu nanoparticles, which can be attributed to more surface vacancies created in PtNi than in PtNiCu. Interestingly, when we run KMC

simulations on PtNi and PtNiCu nanoparticles initialized with switched distribution of Pt and Ni/Cu atoms, the observed differences in the composition and migration of atoms largely disappear (Figure 2.9, hollow symbol curves). These results indicate that although the presence of Cu somewhat reduces the tendency of Ni to dissolve, the enhanced stability is primarily due to the different initial elemental distributions in the PtNi and PtNiCu nanoparticles (Figure 2.9); *i.e.*, the PtNi nanoparticles start with a significantly lower surface fraction of Pt than PtNiCu nanoparticles. As a result, there are more vacancies created on the surface by dissolution in the early stage of KMC runs / CV activation in PtNi, resulting in a substantial initial loss of Ni and allowing more opportunity for the atoms in sub-surface layers to dissolve.

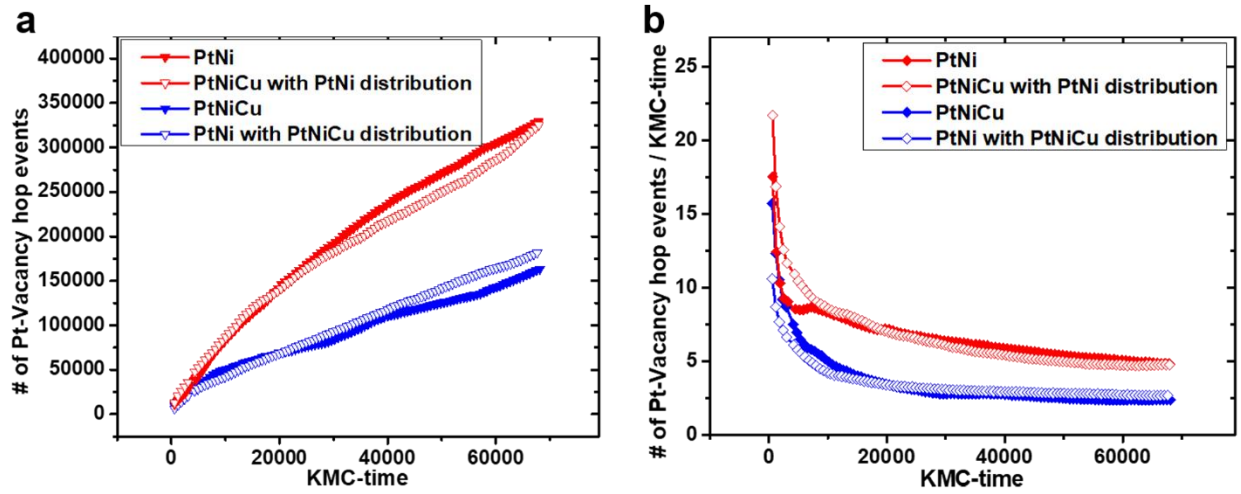

Figure 2. 9. (a) The total number of Pt-Vacancy hop events of representative KMC runs as function of KMC time for the $Pt_{4094}Ni_{1037}Cu_{1044}$ nanoparticle initialized based on experimental data (PtNiCu), the $Pt_{4045}Ni_{2130}$ nanoparticle initialized based on experimental data (PtNi), the $Pt_{4045}Ni_{1065}Cu_{1065}$ nanoparticle created by randomly replacing half of the Ni atoms in the PtNi nanoparticle with Cu atoms (PtNiCu with PtNi distribution), and the $Pt_{4094}Ni_{2081}$ nanoparticle created by replacing all Cu atoms in the PtNi Cu nanoparticle with Ni atoms (PtNi with PtNiCu distribution). (b) The same values as in part (a) divided by the amount of KMC virtual time that has passed. Adapted with permission from Ref.[38] Copyright 2019 Elsevier.

2.4 Conclusion

We reported that octahedral PtNiCu nanoparticles synthesized with solution phase method showed significantly enhanced stability and activity compared to octahedral PtNi. It was found the

introduction of the Cu precursor affected the kinetic growth of the nanoparticles, wherein the Cu ratio is higher than that of Ni at the nucleation stage, followed by the deposition of more Ni. The increased concentration of Cu in early stages of particle growth, relative to Ni, is likely due to the higher reduction potential of the $Cu(Ac)_2$ precursor relative to $Ni(Ac)_2$, providing a design guideline for future efforts. Such PtNiCu nanoparticles were found to retain more Cu and Ni during electrochemical cycling compared to PtNi, leading to improved activity and stability. Kinetic Monte Carlo (KMC) simulations were rationally initialized to reflect a realistic elemental distribution within the nanoparticles, resulting in good agreement between simulations and experimental characterizations of the compositions and structures of the PtNiCu and PtNi nanoparticles after activation. The novel integration between simulation and experiment revealed that the enhanced stability and activity in PtNiCu likely resulted from an increase in the fraction of Pt atoms on the surface of the pre-activated PtNiCu nanoparticles compared to PtNi, which reduces surface dissolution of the 3d transition metals (Ni and Cu in this work) and the creation of surface vacancies, thus limiting the dissolution of atoms from sub-surface layers.

2.5 References

1. Lim, B.; Jiang, M.; Camargo, P. H. C.; Cho, E. C.; Tao, J.; Lu, X.; Zhu, Y.; Xia, Y., Pd-Pt Bimetallic Nanodendrites with High Activity for Oxygen Reduction. *Science* 2009, **324**, 1302-1305 doi:10.1126/science.1170377

2. Chen, C.; Kang, Y.; Huo, Z.; Zhu, Z.; Huang, W.; Xin, H. L.; Snyder, J. D.; Li, D.; Herron, J. A.; Mavrikakis, M.; Chi, M.; More, K. L.; Li, Y.; Markovic, N. M.; Somorjai, G. A.; Yang, P.; Stamenkovic, V. R., Highly Crystalline Multimetallic Nanoframes with Three-Dimensional Electrocatalytic Surfaces. *Science* 2014, **343**, 1339-1343 doi:10.1126/science.1249061

3. Zhang, L.; Roling, L. T.; Wang, X.; Vara, M.; Chi, M.; Liu, J.; Choi, S.-I.; Park, J.; Herron, J. A.; Xie, Z.; Mavrikakis, M.; Xia, Y., Platinum-Based Nanocages with Subnanometer-Thick Walls and Well-Defined, Controllable Facets. *Science* 2015, **349**, 412-416 doi:10.1126/science.aab0801

4. Li, M.; Zhao, Z.; Cheng, T.; Fortunelli, A.; Chen, C.-Y.; Yu, R.; Zhang, Q.; Gu, L.; Merinov, B. V.; Lin, Z.; Zhu, E.; Yu, T.; Jia, Q.; Guo, J.; Zhang, L.; Goddard, W. A.; Huang, Y.; Duan, X., Ultrafine Jagged Platinum Nanowires Enable Ultrahigh Mass Activity for the Oxygen Reduction Reaction. *Science* 2016, **354**, 1414-1419 doi:10.1126/science.aaf9050

5. Bu, L.; Zhang, N.; Guo, S.; Zhang, X.; Li, J.; Yao, J.; Wu, T.; Lu, G.; Ma, J.-Y.; Su, D.; Huang, X., Biaxially Strained Ptpb/Pt Core/Shell Nanoplate Boosts Oxygen Reduction Catalysis. *Science* 2016, **354**, 1410-1414 doi:10.1126/science.aah6133

6. Stamenkovic, V. R.; Fowler, B.; Mun, B. S.; Wang, G.; Ross, P. N.; Lucas, C. A.; Marković, N. M., Improved Oxygen Reduction Activity on Pt3ni(111) Via Increased Surface Site Availability. *Science* 2007, **315**, 493-497 doi:10.1126/science.1135941

7. Wu, J.; Zhang, J.; Peng, Z.; Yang, S.; Wagner, F. T.; Yang, H., Truncated Octahedral Pt3ni Oxygen Reduction Reaction Electrocatalysts. *J. Am. Chem. Soc.* 2010, **132**, 4984-4985 doi:10.1021/ja100571h

8. Zhang, J.; Yang, H.; Fang, J.; Zou, S., Synthesis and Oxygen Reduction Activity of Shape-Controlled Pt3ni Nanopolyhedra. *Nano Lett.* 2010, **10**, 638-644 doi:10.1021/nl903717z

9. Carpenter, M. K.; Moylan, T. E.; Kukreja, R. S.; Atwan, M. H.; Tessema, M. M., Solvothermal Synthesis of Platinum Alloy Nanoparticles for Oxygen Reduction Electrocatalysis. *J. Am. Chem. Soc.* 2012, **134**, 8535-8542 doi:10.1021/ja300756y

10. Cui, C.; Gan, L.; Li, H.-H.; Yu, S.-H.; Heggen, M.; Strasser, P., Octahedral Ptni Nanoparticle Catalysts: Exceptional Oxygen Reduction Activity by Tuning the Alloy Particle Surface Composition. *Nano Lett.* 2012, **12**, 5885-5889 doi:10.1021/nl3032795

11. Choi, S.-I.; Xie, S.; Shao, M.; Odell, J. H.; Lu, N.; Peng, H.-C.; Protsailo, L.; Guerrero, S.; Park, J.; Xia, X.; Wang, J.; Kim, M. J.; Xia, Y., Synthesis and Characterization of 9 Nm Pt–Ni Octahedra with a Record High Activity of 3.3 a/Mgpt for the Oxygen Reduction Reaction. *Nano Lett.* 2013, **13**, 3420-3425 doi:10.1021/nl401881z

12. Cui, C.; Gan, L.; Heggen, M.; Rudi, S.; Strasser, P., Compositional Segregation in Shaped Pt Alloy Nanoparticles and Their Structural Behaviour During Electrocatalysis. *Nat. Mater.* 2013, **12**, 765-771 doi:10.1038/nmat3668

13. Huang, X.; Zhao, Z.; Chen, Y.; Zhu, E.; Li, M.; Duan, X.; Huang, Y., A Rational Design of Carbon-Supported Dispersive Pt-Based Octahedra as Efficient Oxygen Reduction Reaction Catalysts. *Energy Environ. Sci.* 2014, **7**, 2957-2962 doi:10.1039/C4EE01082E

14. Niu, G.; Zhou, M.; Yang, X.; Park, J.; Lu, N.; Wang, J.; Kim, M. J.; Wang, L.; Xia, Y., Synthesis of Pt–Ni Octahedra in Continuous-Flow Droplet Reactors for the Scalable Production of Highly Active Catalysts toward Oxygen Reduction. *Nano Lett.* 2016, **16**, 3850-3857 doi:10.1021/acs.nanolett.6b01340

15. Zhang, C.; Hwang, S. Y.; Trout, A.; Peng, Z., Solid-State Chemistry-Enabled Scalable Production of Octahedral Pt–Ni Alloy Electrocatalyst for Oxygen Reduction Reaction. *J. Am. Chem. Soc.* 2014, **136**, 7805-7808 doi:10.1021/ja501293x

16. Zhao, Z.; Feng, M.; Zhou, J.; Liu, Z.; Li, M.; Fan, Z.; Tsen, O.; Miao, J.; Duan, X.; Huang, Y., Composition Tunable Ternary Pt-Ni-Co Octahedra for Optimized Oxygen Reduction Activity. *Chem. Commun.* 2016, **52**, 11215-11218 doi:10.1039/C6CC06165F

17. Beermann, V.; Gocyla, M.; Willinger, E.; Rudi, S.; Heggen, M.; Dunin-Borkowski, R. E.; Willinger, M.-G.; Strasser, P., Rh-Doped Pt–Ni Octahedral Nanoparticles: Understanding the Correlation between Elemental Distribution, Oxygen Reduction Reaction, and Shape Stability. *Nano Lett.* 2016, **16**, 1719-1725 doi:10.1021/acs.nanolett.5b04636

18. Huang, X.; Zhao, Z.; Cao, L.; Chen, Y.; Zhu, E.; Lin, Z.; Li, M.; Yan, A.; Zettl, A.; Wang, Y. M.; Duan, X.; Mueller, T.; Huang, Y., High-Performance Transition Metal–Doped Pt3ni Octahedra for Oxygen Reduction Reaction. *Science* 2015, **348**, 1230-1234 doi:10.1126/science.aaa8765

19. Arán-Ais, R. M.; Dionigi, F.; Merzdorf, T.; Gocyla, M.; Heggen, M.; Dunin-Borkowski, R. E.; Gliech, M.; Solla-Gullón, J.; Herrero, E.; Feliu, J. M.; Strasser, P., Elemental Anisotropic Growth and Atomic-Scale Structure of Shape-Controlled Octahedral Pt–Ni–Co Alloy Nanocatalysts. *Nano Lett.* 2015, **15**, 7473-7480 doi:10.1021/acs.nanolett.5b03057

20. Zhang, C.; Sandorf, W.; Peng, Z., Octahedral Pt_2cuni Uniform Alloy Nanoparticle Catalyst with High Activity and Promising Stability for Oxygen Reduction Reaction. *ACS Catal.* 2015, **5**, 2296-2300 doi:10.1021/cs502112g

21. He, D.; Zhang, L.; He, D.; Zhou, G.; Lin, Y.; Deng, Z.; Hong, X.; Wu, Y.; Chen, C.; Li, Y., Amorphous Nickel Boride Membrane on a Platinum–Nickel Alloy Surface for Enhanced Oxygen Reduction Reaction. *Nat. Commun.* 2016, **7**, 12362 doi:10.1038/ncomms12362

22. Jia, Q.; Zhao, Z.; Cao, L.; Li, J.; Ghoshal, S.; Davies, V.; Stavitski, E.; Attenkofer, K.; Liu, Z.; Li, M.; Duan, X.; Mukerjee, S.; Mueller, T.; Huang, Y., Roles of Mo Surface Dopants in Enhancing the Orr Performance of Octahedral Ptni Nanoparticles. *Nano Lett.* 2018, **18**, 798-804 doi:10.1021/acs.nanolett.7b04007

23. Lim, J.; Shin, H.; Kim, M.; Lee, H.; Lee, K.-S.; Kwon, Y.; Song, D.; Oh, S.; Kim, H.; Cho, E., Ga–Doped Pt–Ni Octahedral Nanoparticles as a Highly Active and Durable Electrocatalyst for Oxygen Reduction Reaction. *Nano Lett.* 2018, **18**, 2450-2458 doi:10.1021/acs.nanolett.8b00028

24. Zhang, Y.; Duan, Z.; Xiao, C.; Wang, G., Density Functional Theory Calculation of Platinum Surface Segregation Energy in Pt3ni (111) Surface Doped with a Third Transition Metal. *Surf. Sci.* 2011, **605**, 1577-1582 doi:https://doi.org/10.1016/j.susc.2011.05.032

25. Wang, G.; Van Hove, M. A.; Ross, P. N.; Baskes, M. I., Monte Carlo Simulations of Segregation in Pt-Ni Catalyst Nanoparticles. *J. Chem. Phys.* 2005, **122**, 024706 doi:doi:http://dx.doi.org/10.1063/1.1828033

26. Cao, L.; Mueller, T., Theoretical Insights into the Effects of Oxidation and Mo-Doping on the Structure and Stability of Pt–Ni Nanoparticles. *Nano Lett.* 2016, **16**, 7748-7754 doi:10.1021/acs.nanolett.6b03867

27. Callejas-Tovar, R.; Diaz, C. A.; de la Hoz, J. M. M.; Balbuena, P. B., Dealloying of Platinum-Based Alloy Catalysts: Kinetic Monte Carlo Simulations. *Electrochim. Acta* 2013, **101**, 326-333 doi:https://doi.org/10.1016/j.electacta.2013.01.053

28. Wang, C.; Chi, M.; Wang, G.; van der Vliet, D.; Li, D.; More, K.; Wang, H.-H.; Schlueter, J. A.; Markovic, N. M.; Stamenkovic, V. R., Correlation between Surface Chemistry and Electrocatalytic Properties of Monodisperse Ptxni1-X Nanoparticles. *Adv. Funct. Mater.* 2011, **21**, 147-152 doi:10.1002/adfm.201001138

29. Sanchez, J. M.; Ducastelle, F.; Gratias, D., Generalized Cluster Description of Multicomponent Systems. *Physica A* 1984, **128**, 334-350 doi:https://doi.org/10.1016/0378-4371(84)90096-7

30. Cao, L.; Li, C.; Mueller, T., The Use of Cluster Expansions to Predict the Structures and Properties of Surfaces and Nanostructured Materials. *J. Chem. Inf. Model.* 2018, doi:10.1021/acs.jcim.8b00413

31. Kohn, W.; Sham, L. J., Self-Consistent Equations Including Exchange and Correlation Effects. *Phys. Rev.* 1965, **140**, A1133-A1138

32. Schulze, T. P., Efficient Kinetic Monte Carlo Simulation. *J. Comput. Phys.* 2008, **227**, 2455-2462 doi:https://doi.org/10.1016/j.jcp.2007.10.021

33. Serebrinsky, S. A., Physical Time Scale in Kinetic Monte Carlo Simulations of Continuous-Time Markov Chains. *Phys. Rev. E* 2011, **83**, 037701

34. Mueller, T.; Ceder, G., Exact Expressions for Structure Selection in Cluster Expansions. *Phys. Rev. B* 2010, **82**, 184107

35. Mueller, T.; Ceder, G., Bayesian Approach to Cluster Expansions. *Phys. Rev. B* 2009, **80**, 024103

36. van de Walle, A.; Ceder, G., Automating First-Principles Phase Diagram Calculations. *J. Phase Equilib.* 2002, **23**, 348 doi:10.1361/105497102770331596

37. Karlberg, G. S.; Rossmeisl, J.; Nørskov, J. K., Estimations of Electric Field Effects on the Oxygen Reduction Reaction Based on the Density Functional Theory. *Phys. Chem. Chem. Phys.* 2007, **9**, 5158-5161 doi:10.1039/B705938H

38. Cao, L.; Zhao, Z.; Liu, Z.; Gao, W.; Dai, S.; Gha, J.; Xue, W.; Sun, H.; Duan, X.; Pan, X.; Mueller, T.; Huang, Y., Differential Surface Elemental Distribution Leads to Significantly Enhanced Stability of Ptni-Based Orr Catalysts. *Matter* 2019, **1**, 1567-1580 doi:https://doi.org/10.1016/j.matt.2019.07.015

39. Fuel Cell Technologies Office Multi-Year Research, Development, and Demonstration Plan. Department of Energy https://www.energy.gov/eere/fuelcells/downloads/fuel-cell-technologies-office-multi-year-research-development-and-22.

40. Arning, M. D.; Minteer, S. D., Electrode Potentials. In *Handbook of Electrochemistry*, Zoski, C., Ed. Elsevier: Amsterdam, 2007; pp 813-827.

41. Metropolis, N.; Rosenbluth, A. W.; Rosenbluth, M. N.; Teller, A. H.; Teller, E., Equation of State Calculations by Fast Computing Machines. *J. Chem. Phys.* 1953, **21**, 1087-1092 doi:10.1063/1.1699114

42. Shao, M.; Odell, J. H.; Peles, A.; Su, D., The Role of Transition Metals in the Catalytic Activity of Pt Alloys: Quantification of Strain and Ligand Effects. *Chem. Commun.* 2014, **50**, 2173-2176 doi:10.1039/C3CC47341D

43. Cao, L.; Mueller, T., Rational Design of Pt3ni Surface Structures for the Oxygen Reduction Reaction. *J. Phys. Chem. C* 2015, **119**, 17735-17747 doi:10.1021/acs.jpcc.5b04951

44. Jia, Q.; Liang, W.; Bates, M. K.; Mani, P.; Lee, W.; Mukerjee, S., Activity Descriptor Identification for Oxygen Reduction on Platinum-Based Bimetallic Nanoparticles: In Situ Observation of the Linear Composition–Strain–Activity Relationship. *ACS Nano* 2015, **9**, 387-400 doi:10.1021/nn506721f

45. Strasser, P.; Koh, S.; Anniyev, T.; Greeley, J.; More, K.; Yu, C.; Liu, Z.; Kaya, S.; Nordlund, D.; Ogasawara, H.; Toney, M. F.; Nilsson, A., Lattice-Strain Control of the Activity in Dealloyed Core–Shell Fuel Cell Catalysts. *Nat. Chem.* 2010, **2**, 454 doi:10.1038/nchem.623 https://www.nature.com/articles/nchem.623#supplementary-information

Chapter 3. Graphene Nanopocket Encaged PtCo Nanocatalysts for Highly Durable Fuel Cell Operation under the Demanding Ultralow Pt Loading Conditions

3.1 Introduction

Proton exchange membrane fuel cells (PEMFCs) attract great interest as a clean power source to replace internal combustion engines. Platinum (Pt) group metals (PGMs) are indispensable catalyst materials for the current commercial PEMFCs, especially for accelerating the sluggish cathodic oxygen reduction reaction (ORR)[1]. We note that the PGM catalysts are also essential in the catalytic converters of the internal combustion engines (ICEs) for reducing hazardous gas emission[2]. The amount of PGM required for the internal combustion engine vehicles is about 2-8 grams per vehicle, which consumes nearly half of the total global PGM supply[3-4]. However, the amount of PGM used in current commercial fuel cell vehicles (FCV) is about 5-10 times higher (*e.g.*, ~36 grams per vehicle in Toyota Mirai)[5-7], which is clearly not sustainable. Hence, the high cost and limited reserve of PGM represent the most critical roadblock to the broad implementation of PEMFCs[8].

To enable more widespread adoption of PEMFCs, it is highly desirable to reduce the PGM usage[9], which has motivated worldwide efforts to develop more active and more durable catalysts[10-27]. To this end, the US Department of Energy (DOE) has set a series of technical targets for PEMFC catalysts, including a minimum beginning-of-life (BOL) mass activity (MA) of 0.44 A/mg_{PGM}, a rated power of 8 W/mg_{PGM}, an end-of-life (EOL) MA retention > 60% and a voltage loss < 30 mV at 0.8 A/cm^2 after the aggressive square wave accelerated durability test (ADT)[28].

Simultaneously achieving the DOE targets in practical PEMFCs at the ultralow PGM loading is fundamentally challenging due to several intrinsic trade-off factors. In general, the intrinsic MA of a given PGM catalyst is determined by the product of its specific activity (SA) and

electrochemical surface area (ECSA). Although an increase of either SA or ECSA could lead to a significant boost in MA as demonstrated in half-cell studies based on rotating disk electrode (RDE)[10-15], it has been a persistent challenge to translate such improved MA into a proportional reduction of PGM loading in full-cell [*i.e.* membrane electrode assembly (MEA)] test pertaining to practical PEMFCs[9, 29], where mass transport plays a more important role. In this regard, although advanced PGM catalyst with high SA can in principle help maintain the activity by providing higher turnover frequency (TOF), it exerts higher stress on mass transport in order to deliver more reactants to and remove more products away from each catalyst site. Particularly, a reduction in PGM loading reduces the total number of active sites on the electrode, elevating mass transport stress to each active site and eventually causing serious mass transport resistance that limit the achievable power or MA in practical PEMFCs[30]. To mitigate the limitations caused by reduced PGM loading, one may reduce the catalyst size to form ultrafine nanocatalysts, rendering high ECSA (larger number of active sites per mass). However, the ultrafine nanoparticles (particularly for those < 4 nm) with a high surface-to-volume ratio are thermodynamically less stable, prone to substantial size growth through either a physical coalescence and/or Ostwald ripening process[31-32], which lead to gradual ECSA lost and MA lost, resulting in unsatisfactory durability[33-34].

Therefore, the desired reduction of the PGM loading in MEA to the ultralow level exacerbates the challenge of retaining long-term operation durability. In particular, to sustain the same power density (or current density) at a lower PGM loading means a higher TOF on a given catalytic site, necessitating faster oxygen delivery and water removal, which could accelerate the diffusion of dissolved Pt atoms and the Ostwald ripening process, thus further aggravating the catalyst degradation during PEMFC operation. Additionally, considering that the oxygen transport resistance in the MEA is inversely proportional to the number of catalytic sites[9, 35], at ultralow

PGM loading with already reduced active sites to possibly just above the function threshold, a slight catalyst degradation (*e.g.*, catalyst coalescence and reduction of catalytic sites after ADT) could lead to a more dramatic increase of oxygen transport resistance and consequently a more substantial performance loss, much more severe than that in MEA with higher PGM loading (Figure 3.1)[35]. For example, the durability of the MEA cells made with commercial Pt/C catalyst, severely degraded when the total PGM loading is reduced from 0.100 to 0.070 mg/cm^2, with the voltage loss at 0.80 mA/cm^2 increased substantially from 54 mV to 163 mV after ADT, far exceeding the DOE target of 30 mV (Figure 3.1b). Thus, to maintain the long-term stability in PEMFCs with ultralow PGM loading represents a highly demanding situation that requires ultrafine sized nanocatalysts with exceptional durability, two intrinsically competing requirements in a nanocatalyst design. This has imposed a persistent challenge to continue reducing the PGM loading in practical PEMFCs to reach the level of ICE vehicles.

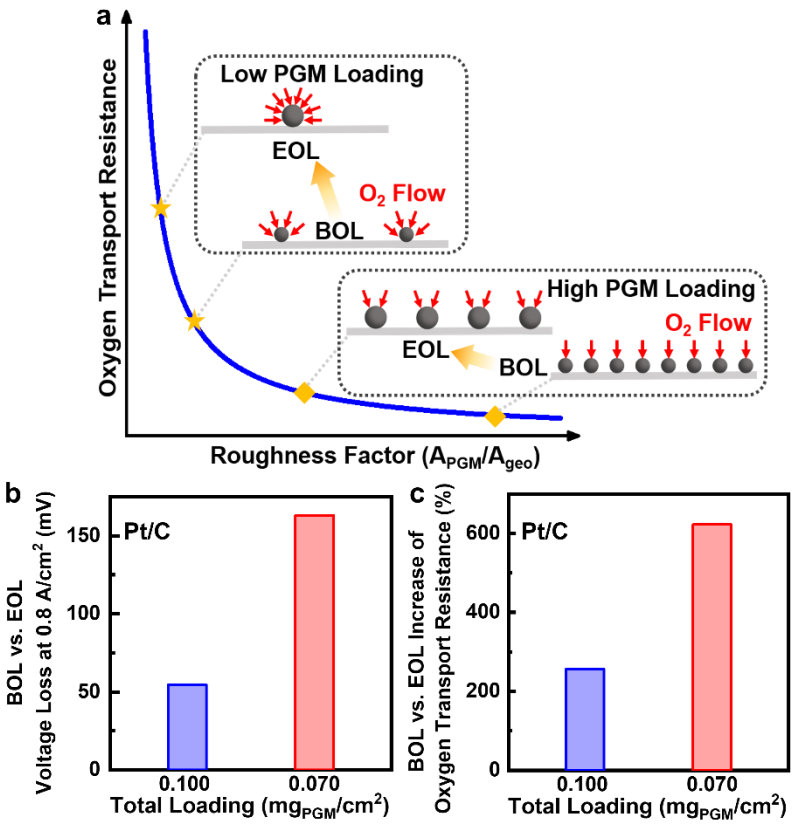

Figure 3. 1. Oxygen transport resistance vs. catalyst roughness factor to highlight the impact of PGM loading on the durability of MEA. The roughness factor is defined as the electrochemical active area (A_{PGM}) divided by the area of the electrode (A_{geo}) and largely correlates with the number of catalyst nanoparticles for a given PGM loading. For high PGM loading with a larger number of catalytic sites, the oxygen diffusion resistance is relatively small. Nanocatalyst coalescence or Ostwald ripening during the ADT reduces the number of catalytic sites, and thus require delivering more O_2 to a given catalytic site and thus lead to a slight increase of oxygen transport resistance. In contrast, for the low PGM loading, more oxygen needs to be delivered onto each nanocatalyst to maintain the same current, and size growth during ADT could cause a more serious challenge in oxygen diffusion, thus leading to a more dramatic increase in oxygen diffusion resistance. Additionally, similar challenges exist for water removal. At lower PGM loading, more water needs to be removed from a given catalytic site, which may also contribute to faster diffusion of dissolved Pt atoms and a more rapid Ostwald ripening process, thus further accelerating the catalyst degradation. (a) Sketch of oxygen transport resistance related to roughness factor (related to PGM loading) during the fuel cell operation (BOL vs. EOL). (b) The voltage loss at 0.8 A/cm^2 (BOL vs. EOL) at different loading. (c) The increased ratio of measured oxygen transport resistance (BOL vs. EOL) at different loading. Adapted with permission from Ref.[36] Copyright 2022 Springer Nature

In the previous chapter, we investigated the stability enhancement strategy of introducing a third element to the PtNi system in RDE testing. In this chapter, we further explore the effective catalyst design to improve durability in practical MEA fuel cell devices. Here we report the design and synthesis of ultrafine platinum cobalt nanocatalysts encaged in graphene nanopockets

(PtCo@Gnp) for highly robust ultralow PGM loading PEMFCs. With this design, encaging ultrafine catalysts in non-contacting graphene nanopockets that not only allows electrochemical accessibility but also restricts catalyst coalescence, and retards the oxidative dissolution, diffusion and Ostwald ripening process. This unique structure ensures superior catalyst durability even under the highly demanding ultralow PGM loading conditions. With the PtCo@Gnp nanocatalysts, the MEA with a PGM loading of 0.100 mg/cm^2 delivers a state-of-the-art MA of 1.14 A/mg$_{PGM}$, a rated power of 10.1 W/mg$_{PGM}$ (1.01 W//cm^2), a MA retention of 66%, and a potential loss of only 23.5 mV at 0.8 A/cm^2, all exceeding the DOE technical targets for 2020. Furthermore, at a reduced PGM loading (total loading 0.07 mg/cm^2 including both cathode and anode) approaching the DOE stretch target (0.0625 mg$_{PGM}$/cm^2)[9], the MEA retains a high MA of 1.21 A/mg$_{PGM}$, a rated power of 13.2 W/mg$_{PGM}$ (0.92 W//cm^2), a MA retention of 73%, an EOL rated power of 0.80 W/cm^2 and a voltage loss of only 18.8 mV at 0.8 A/cm^2 after ADT. With greatly improved rated power (13.2 W/mg$_{PGM}$) and durability in MEAs with an ultralow PGM loading (0.070 mg/cm^2), we project a 90-kW FCV can be realized with a PGM loading of only 6.8 grams PGM, comparable to that in typical catalytic converters for ICE powered vehicles[2, 9].

3.2 Experimental Methods

Materials and Chemicals

Platinum (II) acetylacetonate [Pt(acac)$_2$], and Aquivion D83-06A ionomer dispersion were purchased from Sigma Aldrich. Cobalt(II) acetylacetonate [Co(acac)$_2$], commercial Pt/C (weight ratio of Pt: 10%), commercial Pt/C (weight ratio of Pt: 40%) were purchased from Alfa Aesar. Commercial PtCo/C (c-PtCo/C) catalyst was purchased from Premetek. Ethanol was purchased from Decon Labs, Inc. N, N-Dimethylformamide (DMF), acetone, and isopropanol (IPA) were purchased from Fisher Scientific. Gas diffusion layer (GDL), and polytetrafluoroethylene (PTFE)

gasket were purchased from The Fuel Cell Store. Carbon black (Ketjenblack EC-300J) was obtained from Fitz Chem LLC. The water used was ultrapure (18.2 MΩ·cm) and was generated by a Millipore equipment.

Treatment of Carbon Support

The carbon black support (Ketjenblack EC-300J) is treated in hydrogen (H_2)/argon (Ar) mixture before use as noted in the literature[37].

Synthesis of PtCo@Gnp

For a typical synthesis, 150 mg of carbon black, 150 mg of $Pt(acac)_2$, 190 mg of $Co(acac)_2$, and 10 mL of acetone were mixed in a glass vial under ultrasonication for 10 min. Then acetone in the mixture was evaporated at room temperature. The powder mixture of metal precursor and carbon black was collected and further annealed in a quartz tube in an H_2/Ar mixture in a quartz tube. The temperature is heated from about 20 °C to 700 °C in 15 hours and maintained at 700 °C for 6 hours. The sample was collected after it was fully cooled to room temperature.

Acid-wash and Annealing

The synthesized PtCo@Gnp was further subjected to acid wash in N_2 saturated 0.2 M H_2SO_4 within a capped vial. The vial was kept at 85 ºC for 16 hours. After acid wash, the catalyst was rinsed a few times with ultrapure water, and collected via centrifugation. Then the collected catalyst was dried in in vacuum. The obtained catalyst was then annealed in H_2/Ar mixture, at 200 °C for 1.5 hours. The final product was collected after it was fully cooled down.

For a fair comparison, the c-PtCo/C is also subjected to acid wash and further annealing with the same procedure to reduce the poison effect of leached metal cation during fuel cell operation.

Structure and Composition Characterization

X-ray powder diffraction (XRD) patterns were collected with a Panalytical X'Pert Pro X-ray powder diffractometer using Cu-Kα radiation as an incident beam. X-ray photoelectron spectroscopy (XPS) tests were done with a Kratos AXIS Ultra DLD spectrometer. The elemental composition of catalysts was analyzed with inductively coupled plasma atomic emission spectroscopy (ICP-AES, Shimadzu ICPE-9000) as well as energy-dispersive spectroscopy (EDS) [coupled with an FEI TITAN Transmission electron microscopy (TEM)].

TEM images were taken with an FEI T12 transmission electron microscope operated at 120 kV. Atomic resolution high angle annular dark-field (HAADF) images, as well as energy-dispersive spectroscopy (EDS) maps, were taken using a JEOL Grand ARM300CF scanning/transmission electron microscopy (S/TEM) operated at 300 kV. The TEM/STEM sample grids were prepared by dispersing the sample in a mixture of water and ethanol, then dripping the dispersion onto regular carbon film coated aluminum grids (for EDS analysis), regular carbon film coated copper grids, or lacey carbon film coated copper grids (for high-resolution STEM) using a pipette and drying under ambient condition.

The atomic-resolution STEM-EELS experiments were conducted using the unique ultrahigh energy resolution monochromated and spherical aberration-corrected Nion UltraSTEM200, operated at 60 kV. The convergence semi-angle and the beam current were set as 38 mrad and ~15 pA, respectively. The EELS dispersion and dwell time were 0.28 eV/channel and 0.5 s/pixel, respectively. The pixel size of the STEM-EELS spectrum image was set as 0.20–0.34 nm, depending on the field of view. The data analysis of removing background was carried out by the power-law function in the commercial software package Digital Micrograph.

In order to ensure the reliability of the collected atomic-resolution STEM images and EELS spectra of graphene nanopocket. The low accelerating voltage and low beam current were used to

mitigate the electron beam-induced damage to the sample, especially for carbon atoms. Several precautions were also employed during high-resolution STEM experiments to eliminate the electron beam-induced contamination and other artifacts. (1) After dispersing samples onto lacey carbon film coated copper TEM grids, we annealed the as-prepared TEM grids at 160 °C in a vacuum chamber for over 8 hours right before transferring them into Nion UltraSTEM200 electron microscope[38]. Vacuum annealing can remove most of the residual solvent and other absorbed molecules, which are the major source of contamination in TEM. (2) High-resolution STEM experiments were only conducted when the pressure of the TEM column is lower than 2×10^{-9} Torr to ensure an ultraclean environment. (3) During the STEM experiments, we carefully monitored the morphology of the observed nanoparticles and there were no obvious carbon deposits (contaminations) and shape changes. Therefore, we can exclude the carbon deposits and other artifacts that presumably occurred in TEM for explaining the formation of carbon shells covering Pt nanoparticles.

Electrochemical Measurement in RDE

For the ink preparation, the catalyst powder (Pt/C, c-PtNi/C, PtCo@Gnp) was mixed with ethanol under ultrasonication for about 5 min. Then, ionomer dispersion was added to the ink, and the ratio of ionomer dispersion over the solvent (Nafion dispersion, 5 wt%) was fixed to be 8 μL/ml. After a short time of ultrasonication (1-2 min), the final ink was ready to use. And, 10 μL of prepared ink was dropped onto a 5 mm diameter glassy carbon electrode and was dried in air. Then, the electrode was ready for the electrochemical test. For all studied catalysts, the platinum group metal (PGM) loading was fixed at about 3.2 μg for each tested electrode, which is estimated based on the overall PGM ratio within the catalyst (determined by ICP-AES). The electrochemical measurements were performed in a three-electrode system, which includes a working electrode, a

counter electrode, and a reference electrode. The working electrode glassy carbon electrode loaded with catalyst as described above. An Ag/AgCl electrode and a Pt wire were used as the reference electrode and counter electrode, respectively. Cyclic Voltammetry (CV) measurements were conducted in an N_2 saturated 0.1 M $HClO_4$ solution between 0.05 to 1.1 V vs. reversible hydrogen electrode (RHE) at a sweep rate of 100 mV/s. Electrochemical active surface area (ECSA) was measured by integrating the hydrogen underpotential deposition (H_{upd}) peak in CV, assuming 210 $\mu C/cm^2_{PGM}$. Oxygen reduction reaction (ORR) tests were conducted in an O_2 saturated 0.1 M $HClO_4$ solution with a linear voltage scan at a sweep rate of 20 mV/s.

MEA Fabrication and Measurement

In general, the fabrication of membrane electrode assembly (MEA) followed the established protocol noted in our previous work[37]. The catalyst ink was prepared by mixing the catalysts with water-IPA solvent and ionomer solution through ultrasonication. The fresh ink was then spray-coated onto a reinforced perfluorosulfonic acid (PFSA) membrane (12 μm thickness) by using a Sono-Tek ultrasonic spray system. The anode catalyst was Pt/C (weight ratio of Pt: 10%) with PGM loading fixed to be 0.010 mg_{PGM}/cm^2. The cathode catalyst loading was controlled to be 0.060 and 0.090 mg_{PGM}/cm^2. Both anode and cathode loading were confirmed by the ICP-AES measurements. The prepared CCM was dried in a vacuum desiccator to evaporate the solvents before assembly. Two gas diffusion layers (GDLs), two PTFE gaskets, and the CCM were pressed to make the MEA.

Then, a prepared MEA was loaded in a 5 cm^2 single-cell fixture and the performance was evaluated in a Scribner 850e fuel cell test system. The MEA was initially activated by holding the potential at 0.5 V under H_2/Air flow (100/100 sccm) at 80 °C, 150 kPa_{abs} (abs: absolute; all pressures in this work refer to the absolute pressure unless specifically noted), and 100% relative

humidity (RH). Then, the MEA was further activated at a high humidity condition, which let both cathode and anode gases pass a corresponding humidifier at 80 °C before entering the fuel cell (hold at 60 °C). The mass activity was tested at 80 °C, 150 kPa_{abs}, and 100% RH, with a gas flow rate of 835 (H_2)/2000 (O_2) sccm for anode/cathode. The accelerated durability test (ADT) included 30000 cycles of square wave with each cycle holding the MEA at the voltage of 0.6 V for 3 seconds and then 0.95 V for 3 seconds, according to the DOE MEA ADT protocol for PGM based catalysts. The full ADT is carried at 80 °C, 150 kPa_{abs}, 100% RH with H_2/N_2 flow 100/100 sccm for anode and cathode, respectively. Note that the square wave protocol demonstrates a five times acceleration effect compared to the previously used triangle wave protocol in terms of the degradation of catalyst at a given period, which represents a more aggressive test protocol to better simulate the lifetime degradation of catalysts[39]. The MEA's beginning-of-life (BOL) and end-of-life (EOL) performance metrics, such as MA, ECSA, and H_2 crossover, were recorded by the Scribner 850e fuel cell test station and the Scribner 885 potentiostat associated with the 850e fuel cell station. The ECSA was determined by integrating the CO stripping peak, assuming 420 $\mu C/cm^2_{Pt}$. The CO stripping test in MEA was generally followed the protocol noted in the literature[40].

Rated Power Test for MEA

In general, the estimation of rated power followed the established protocol noted in our previous work[37]. The BOL and EOL rated power of prepared MEA was tested in Scribner 850e fuel cell test system under 94 °C, 250 $kPa_{abs,}$ and 100% RH.[2] The H_2/Air gas flow rate was 126/400 sccm for anode/cathode, which is equivalent to the stoichiometry ratio of 1.5/2.0 at 2.4 A/cm^2 (end of current density plot). The ADT protocol is the same as noted in the previous section.

For a practical fuel cell, DOE sets a heat rejection target of $Q/\Delta T_i$ <1.45. And, the rated power was measured at rated voltage (V_{rated}), which can be defined by the following equation 1 (**Eq. 1**) [4].

$$\frac{Q}{\Delta T_i} = \frac{P_{stack}(1.25 - V_{rated})}{V_{rated}(T_{stack} - T_{ambient})} \qquad \textbf{Eq. 1}$$

The DOE uses a 90-kW stack gross power (Pstack) as an example, which provides 80 kW net power. Assuming that P_{stack} = 90 kW and $T_{ambient}$ =40 °C, if T_{stack} =94 °C, $Q/\Delta T_i$ =1.445, which meets the target ($Q/\Delta T_i$ of ≤1.45), the V_{rated} will be around 0.67 V. Thus, the rated power will be measured at 0.67 V.[2]

Oxygen Transport Resistance Test for MEA

In general, the measurement of oxygen transport resistance followed the established protocol noted in our previous work.[37] The MEA was tested at 80 °C with 65% RH for both anode and cathode. Ultrahigh pure hydrogen was applied to the anode. The mix-gases (O_2 and N_2) were pre-mixed by Airgas, Inc., and the mix-gas cylinders were used as a gas source. The dry O_2 mole ratios for pre-mixed gases were 0.981%, 1.491%, and 2.001%, which was determined by Airgas, Inc. To identify the pressure independent part of the total oxygen transport resistance, the test was performed at a total pressure of 110, 150, 190, 230, and 270 kPa_{abs}. The total oxygen transport resistance can be approximately obtained by the following **Eq. 2**.

$$R_{total} = \frac{4FC_{O_2}}{i_{lim}} = \frac{4F}{i_{lim}} \times \frac{P_{abs} - P_{H_2O}}{RT} \times x_{O_2-dry} \qquad \textbf{Eq. 2}$$

Note: $R_{total}^{O_2}$ represents the total oxygen transport resistance. C_{O_2} represents oxygen concentration. P_{abs} is the total pressure. P_{H_2O} is the pressure of water vapor at testing temperature. x_{O_2-dry} is the dry O_2 ratio. i_{lim} represents the limit current density.

The limit current density was identified as the largest current density (considering the absolute value) obtained through linear voltage sweep (0.12 to 0.40 V, 2 mV/s) using the 885 potentiostat attached to the 850e fuel cell station. The total oxygen transport resistance can be separated into the pressure-dependent part ($R^{P\text{-}d}$) and pressure-independent part ($R^{P\text{-}ind}$), which represents the Knudsen diffusion and diffusion of oxygen through the ionomer layer.[41-42] The relationship of total oxygen resistance (R_{total}), pressure-dependent part of oxygen transport resistance ($R^{P\text{-}d}$), and pressure-independent part of oxygen transport resistance ($R^{P\text{-}ind}$) can be expressed in the following **Eq. 3**.

$$R_{total} = R^{P-d} + R^{P-ind} \qquad \textbf{Eq. 3}$$

Estimation of Size Distribution Weighted by Mass

By assuming a spherical model using the measured size as diameter, we can estimate the relative volume and the relative mass of each nanoparticle to obtain the mass-weighted size distribution, which gives the mass fraction contributed by nanoparticles of different sizes (**Supplementary Table 1**). The weighted average size ($\bar{d}_w$) is obtained by the following **Eq. 4**. The d_i, m_i, V_i, and ρ are the size, mass, volume, and density of that nanoparticle, correspondingly.

$$\bar{d}_w = \frac{\sum_1^n d_i m_i}{\sum_1^n m_i} = \frac{\rho \sum_1^n d_i V_i}{\rho \sum_1^n V_i} = \frac{\sum_1^n d_i V_i}{\sum_1^n V_i} \qquad \textbf{Eq. 4}$$

Estimation of Theoretical Limit of ECSA

We estimated the theoretical limit of ECSA based on the statics of nanoparticle size. A spherical model to estimate the surface Pt area and the Pt mass of each nanoparticle. The ECSA is defined as the sum of accessible surface Pt area of all nanoparticles divided by the sum of Pt mass of all nanoparticles (**Eq. 5**).

$$ECSA = \frac{A_{Pt}}{m_{Pt}} = \frac{b \sum_{i=1}^n 4\pi(\frac{d_i}{2})^2}{\rho_{Pt}(\sum_{i=1}^n \frac{4}{3}\pi(\frac{d_i}{2})^3)} \qquad \textbf{Eq. 5}$$

A_{Pt} is the total surface Pt area and m_{Pt} is the total Pt mass. The d_i is the diameter of a nanoparticle and i represents an integer from 1 to n (n is the total number of nanoparticles). The b is a constant that represents the ratio of accessible surface since some part of the surface is attached with the support. We assumed b to be 0.75. The ρ_{Pt} is the mass of Pt per unit volume, which can be estimated from the lattice parameter and the Pt ratio (**Eq. 6**). The a is the lattice parameter of a unit cell and a can be estimated based on Vegard's law for an alloy sample. The unit cell of face-centered cubic (fcc) packing contains 4 atoms. The c is the average ratio of Pt atoms within a unit cell and is based on the EDS analysis. M_{Pt} is the molar mass of Pt. N_A is Avogadro constant.

$$\rho_{Pt} = \frac{4cM_{Pt}}{N_A a^3} \qquad \textbf{Eq. 6}$$

Note that the only PGM contained in the nanoparticles is Pt. Thus, we can use Pt to represent the PGM.

In addition, for a single nanoparticle, we can also estimate the relation between ECSA and the size (diameter d) of a nanoparticle using a spherical model (**Eq. 7**). The definition of b and ρ_{Pt} in **Eq. 7** is the same as in **Eq. 5**. Since b and ρ_{Pt} are both constants for a given nanoparticle, we further simplified the equation using a C to represent all constants ($C=6b/\rho_{Pt}$). Clearly, we can see an inverse relationship between ECSA and size (diameter d)**.**

$$ECSA = \frac{b4\pi(\frac{d}{2})^2}{\rho_{Pt}\frac{4}{3}\pi(\frac{d}{2})^3} = \frac{6b}{\rho_{Pt}d} = \frac{C}{d} \qquad \textbf{Eq. 7}$$

Estimation of Nanoparticle Density

Assuming a spherical shape for a given nanoparticle, we can obtain the sum of the surface area of all nanoparticles (**Eq. 8**) and the contribution of each nanoparticle to the total surface area (**Eq. 9**). Then, based on the statics, we can obtain the size distribution of nanoparticles weighted by their surface area.

$$A_{total} = \sum_1^n A_i = \sum_1^n 4\pi(\frac{d_i}{2})^2 \qquad \textbf{Eq. 8}$$

$$F_i = \frac{A_i}{A_{total}} \qquad \textbf{Eq. 9}$$

The A_{total} represents the total surface area. The A_i represents the surface area of nanoparticle i (i represents an integer from 1 to n). The d_i represents the diameter of nanoparticle i. The F_i represents the contribution ratio of a given nanoparticle to the total surface area.

The theoretical density of nanoparticles within the MEA cathode can be estimated based on the measured ECSA. We can first obtain the electrochemical surface area per unit area of the electrode by multiplying the ECSA with cathode loading. Then, the total electrochemical surface area can be distributed to each size of nanoparticle according to its contribution to the total surface area (F_i) (**Eq. 10**). Then, the density of nanoparticle of each size (N_i) can be obtained via dividing the distributed electrochemical area of the size (E_i) by the electrochemical surface area of a nanoparticle at the size ($4\pi b(\frac{d_i}{2})^2$). The total density of nanoparticle N_{total} can be obtained by summing up the N_i (**Eq. 11**).

$$E_i = ECSA \times PGM\ loading \times F_i \qquad \textbf{Eq. 10}$$

$$N_{total} = \sum N_i = \sum \frac{E_i}{4\pi b(\frac{d_i}{2})^2} \qquad \textbf{Eq. 11}$$

The E_i is the electrochemical surface area of a given size. N_{total} is the density of nanoparticles in an electrode. N_i represents the density of nanoparticles of a given size. The d_i here represents the diameter of a given nanoparticle. The b is a constant that represents the ratio of accessible surface since some part of the surface is attached with the support. We assumed b to be 0.75 same as the above section of ECSA estimation.

3.3 Results and Discussion

Structure Characterization

The PtCo@Gnp was prepared by impregnating carbon support with organometallic Pt and Co precursors [platinum acetylacetonate and cobalt acetylacetonate], which were then subjected to high-temperature pyrolysis at 700 ^{o}C. The prepared catalysts were further washed with sulfuric acid to pre-leach Co.[43,44-45] The transmission electron microscopy (TEM) studies reveal ultrafine nanoparticles uniformly distributed on the carbon support with a mass-weighted average size of 3.0 ± 0.8 nm (Figure 3.2b, c).

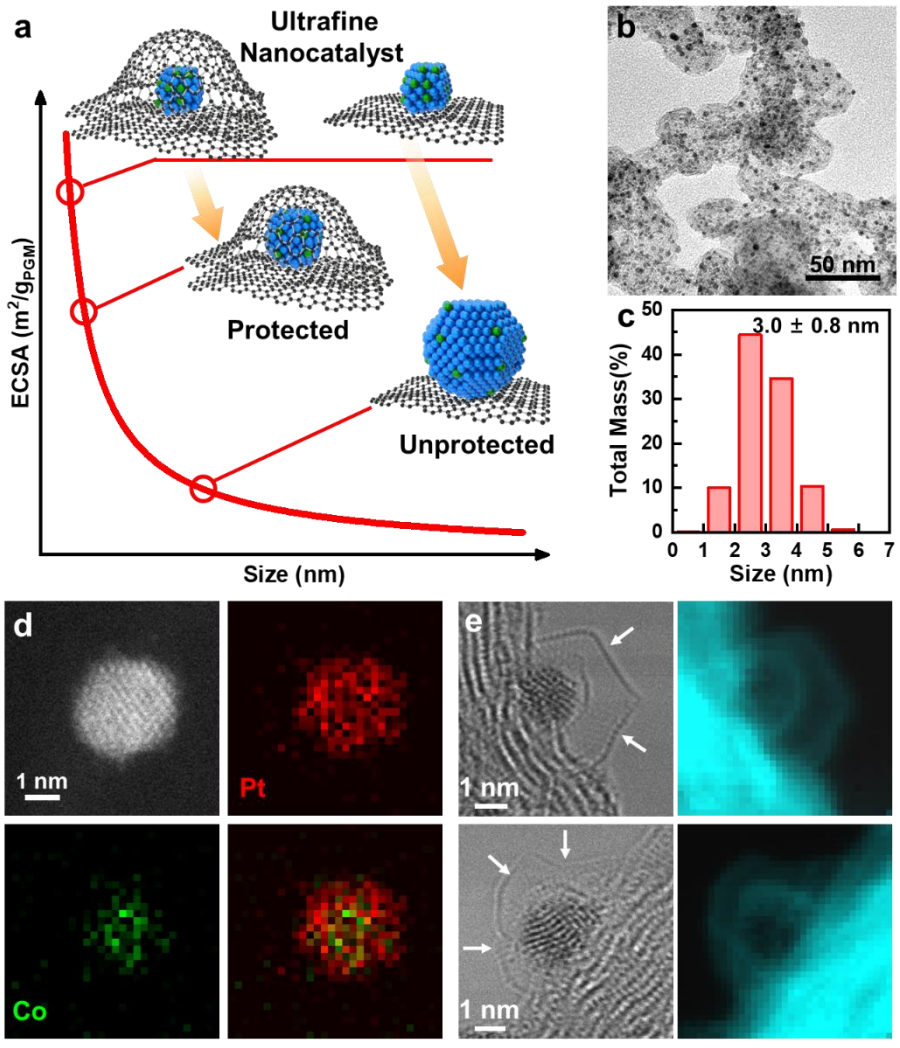

Figure 3. 2. Schematic of the protective nanopocket design and characterization of the PtCo@Gnp. (a) Schematic illustration of ultrafine nanocatalysts encaged in graphene pockets and their impact on ECSA retention after accelerated durability test. Characterization of the PtCo@Gnp before catalysis test: (b) TEM image, (c) size distribution, (d) HAADF STEM image, and EDS elemental maps, and (e) bright-field STEM and EELS mapping at carbon k-edge images highlighting enclosure of ultrafine nanoparticle by graphene nanopockets (indicated by white arrows). Adapted with permission from Ref.[36] Copyright 2022 Springer Nature

The powder X-ray diffraction (XRD) studies show the resulted catalysts exhibit a face-centered cubic (fcc) structure, the same as the Pt/C (Figure 3.3a). The overall composition analysis by the inductively coupled plasma atomic emission spectroscopy (ICP-AES) gives a Pt:Co atomic ratio of 80.8:19.2, while the surface-sensitive X-ray photoelectron spectroscopy (XPS) reveals a higher Pt:Co ratio of 89.4:10.6 (Figure 3.3b, c), indicating a core-shell structure with a Pt-rich shell, which is also confirmed by scanning transmission electron microscopy (STEM) and the corresponding energy-dispersive X-ray spectroscopy (EDS) elemental mapping studies (Figure 3.2d).

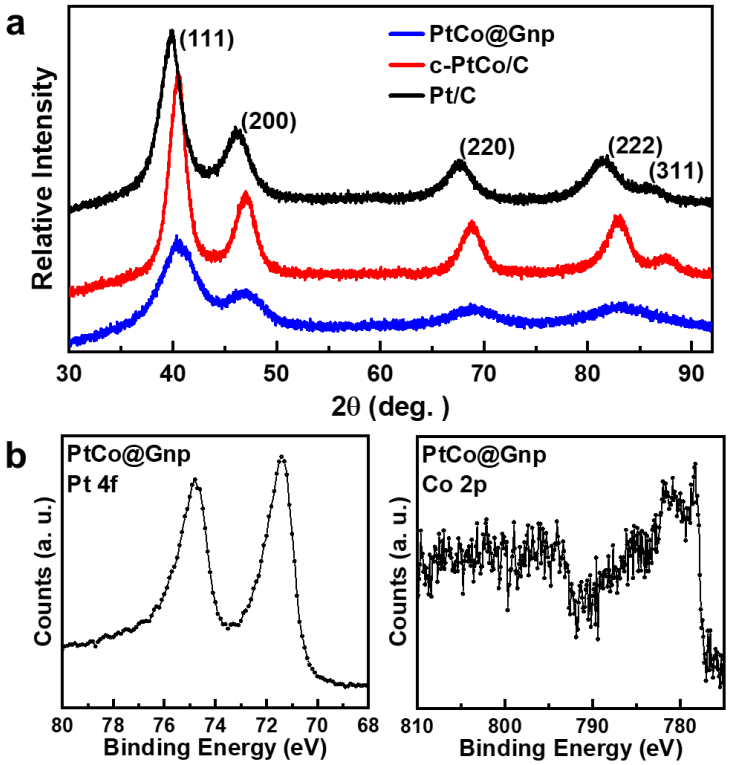

Figure 3. 3. Characterization of tested catalysts. (a) XRD data of Pt/C, c-PtCo/C, PtCo@Gnp, (b) XPS data of PtCo@Gnp. Adapted with permission from Ref.[36] Copyright 2022 Springer Nature

We further examined the PtCo@Gnps with high-resolution STEM, where a close comparison of the high-angle annular dark-field (HAADF) and bright-field STEM images reveals that the ultrafine PtCo nanoparticles are apparently encaged in nanoscale pockets consisting of monolayer or few-layer graphene enclosures (Figure 3.2e). In particular, the bright-field image clearly shows that the PtCo nanoparticles are well supported on carbon backbone structure, with well-resolved graphitic layers. Notably, an additional graphitic layer (typically monolayer graphene) is clearly visible surrounding the PtCo nanoparticles. An exhaustive examination shows all PtCo nanoparticles are encaged in similar graphene nanopockets (Figure 3.2e). The presence of the graphene outer layer around the PtCo nanoparticles was also confirmed by electron energy loss spectroscopy (EELS) mapping (Figure 3.2e). The observed graphene nanopocket is likely formed during the high-temperature pyrolysis process, where the decomposition of the metal acetylacetonates generates gaseous carbonaceous molecules.[46-47] which then react on the PtCo nanocatalyst surface leading to the in situ formation of graphene nanopocket.[48-50]

It is worth noting that such graphene nanopockets generally feature a nanometer-scale space (~0.4-1.0 nm) from the PtCo surface, forming a non-contact enclosure in graphene nanopockets that renders PtCo@Gnp electrochemically accessible. Indeed, the PtCo@Gnp showed an impressive ECSA of 68.7 m^2/g_{PGM}, which is considerably higher than that of Pt/C (34.7 m^2/g_{PGM}) and largely consistent with the expected ECSA for the measured particle size. Similarly, the ORR specific activity of PtCo@Gnp (1.62 mA/cm^2) is 2.7 times that of Pt/C (0.61 mA/cm^2) measured using a rotating disk electrode (RDE) (Figure 3.4). The above features clearly indicate that the graphene nanopocket may be porous allowing for surface accessibility, and the PtCo@Gnp is electrochemically active.

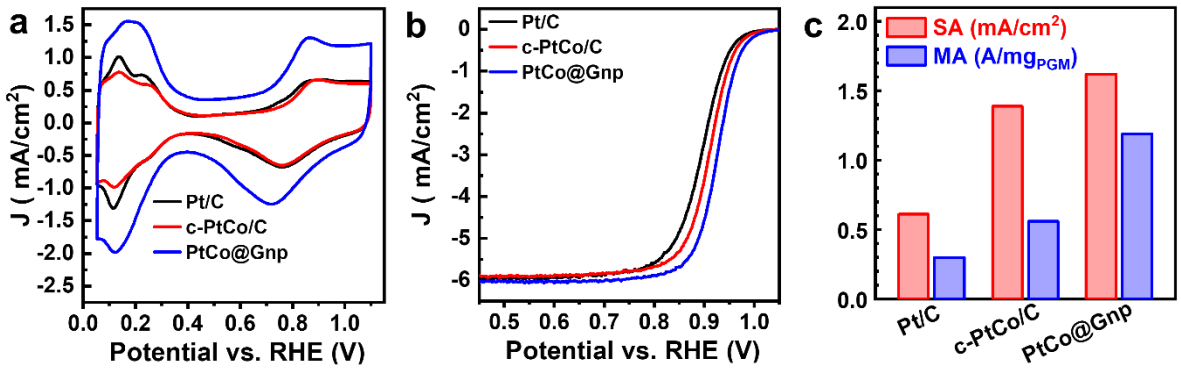

Figure 3. 4. Rotating disk electrode (RDE) test of catalysts. (a) cyclic voltammetry curves tested in N_2 saturated 0.1 M $HClO_4$. (b) ORR polarization curves in O_2 saturated 0.1 M $HClO_4$. (c) comparison of mass activities (MA) and specific activities (SA). Adapted with permission from Ref.[36] Copyright 2022 Springer Nature

Fuel Cell Performance Evaluation

MEAs with different catalysts were fabricated following prior established proctocol[37] (see Methods). In order to benchmark against the DOE 2020 performance targets[28] and also to evaluate the performance of the PtCo@Gnp at ultralow loading, we prepared the cathodes with two distinct PGM loadings of 0.090 and 0.060 mg_{PGM}/cm^2. Together with the anode loading of 0.010 mg_{PGM}/cm^2 (commercial Pt/C), the total PGM loading is 0.100 and 0.070 mg_{PGM}/cm^2, respectively. We note the PGM loading of 0.070 mg_{PGM}/cm^2 is only 19% of the PGM loading in Toyota Mirai (0.365 mg_{PGM}/cm^2)[5, 51] and represents an ultralow PGM loading approaching the DOE stretch target (0.0625 mg_{PGM}/cm^2)[9]. We have benchmarked our catalysts vs. Pt/C and commercial PtCo/C catalyst (noted as c-PtCo/C) at the same PGM loadings. For a fair comparison, all materials were the same in all MEAs except for the cathode catalyst. Accordingly, the MEAs were labeled by the cathode catalysts.

The PtCo@Gnp exhibited an initial MAs of 1.14 A/mg_{PGM} at the cathode PGM loading of 0.090 and MA of 1.21 A/mg_{PGM} at 0.060 mg_{PGM}/cm^2 (Figure 3.5), considerably higher than the Pt/C (0.42 and 0.40 A/mg_{PGM}), c-PtCo (0.57 A/mg_{PGM}) and the DOE target (0.44 A/mg_{PGM}). For

the ADT, we adopted the updated 30,000-cycle square wave protocol by holding the cathode at 0.6 V for 3 s and 0.95 V for 3s in each cycle. Importantly, even at the ultralow loading of 0.070 mg_{PGM}/cm^2, the PtCo@Gnp retained 73% of its initial MA after the aggressive square wave ADT, which is much higher than the 25% and 30% MA retention observed in Pt/C and c-PtCo/C, respectively, at the same loading, and represents the best-known durability under the demanding ultralow PGM loading level achieved in the square wave ADT (Figure 3.5d). Moreover, we note that the PtCo@Gnp EOL MA (0.89 A/mg_{PGM}) is >3 times of the DOE target (0.264 A/mg_{PGM}), >5 times of the c-PtCo/C (0.17 A/mg_{PGM}) and nearly 9 times of the Pt/C (0.10 A/mg_{PGM}), representing the highest EOL MA reported in MEA tests to date (Figure 3.5d).[37, 43, 52-56]

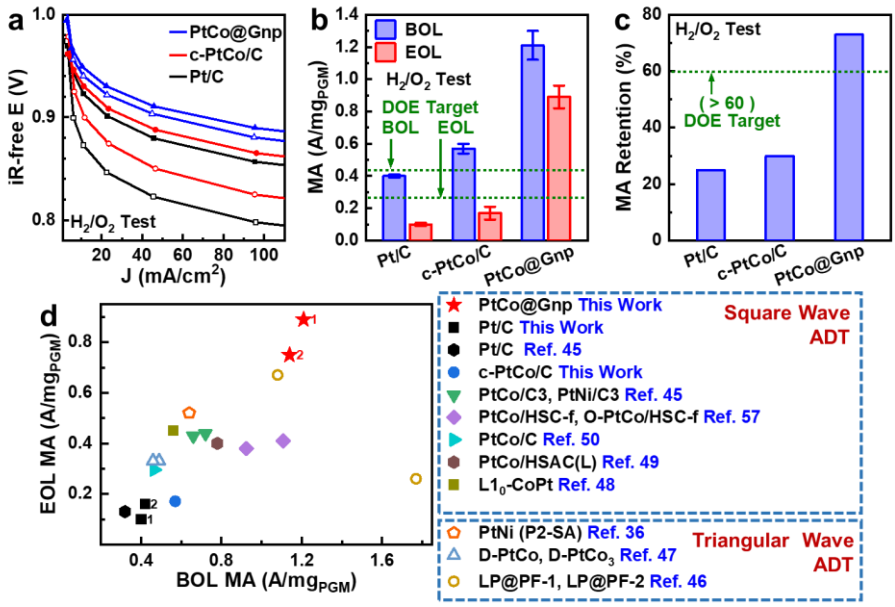

Figure 3. 5. The mass activity (MA) of Pt/C, c-PtCo/C, and PtCo@Gnp tested in membrane electrode assemblies (MEAs) and compared with representative catalysts in the literature. (a-c) MA test under H_2/O_2 flow at 80 °C, 150 kPa_{abs} at the cathode loading of 0.060 mg_{PGM}/cm^2 (total loading 0.070 mg_{PGM}/cm^2). Comparison of (a) polarization plots tested in H_2/O_2, (b) MA, (c) MA retention. The error bars in panel (b) represent the standard deviation. (d) The comparison of beginning-of-life (BOL) and end-of-life (EOL) MA between PtCo@Gnp with the state-of-art in literature. The solid symbols highlight the materials evaluated strictly following the DOE recommended square wave accelerated durability test (ADT), which is five times more aggressive[39] than the hollow symbols represented triangle wave ADT. The plot highlights that the PtoCo@Gnp MEAs show extraordinary EOL MAs far outperforming all other reported values. "Ordered-PtCo" is abbreviated as "O-PtCo". The red star symbols represent MA performance of MEAs with different PGM loadings ((1) 0.070 and (2) 0.100 mg_{PGM}/cm^2) evaluated in this study, showing considerably higher EOL MA than all

previous studies and highlighting exceptional durability. Note that Ref.[52] presents catalysts with mixed PGM and non-PGM sites but only normalized by PGM material (0.033 mg_{Pt}/cm^2 for LP@PF-1, 0.035 mg_{Pt}/cm^2 for LP@PF-2). Adapted with permission from Ref.[36] Copyright 2022 Springer Nature

While the cathode MA test under pure oxygen gives a better evaluation of the intrinsic activity less impacted by mass transfer issues, the rated power test using air as the oxygen source directly reflects the practical performance of the PEMFC under working environment. Following the recommended DOE testing protocols, the rated power of the MEAs was evaluated at 0.67 V when the fuel cell operates at 94 °C.[2, 28, 57] In general, the PtCo@Gnp demonstrated notably better performance than Pt/C or c-PtCo/C throughout the low to high current density regime (Figure 3.6a). In particular, the PtCo@Gnp delivers a mass normalized rated power of 10.1 and 13.2 W/mg_{PGM} at the PGM loading of 0.100, and 0.070 mg_{PGM}/cm^2 (Figure 3.6d), respectively, both of which greatly exceed the DOE target (8 W/mg_{PGM}) (Figure 3.6e).

Impressively, the PtCo@Gnp exhibited outstanding durability far outperforming Pt/C or c-PtCo/C, as reflected in EOL rated power performance after the ADT. In particular, at the ultralow PGM loading of 0.070 mg_{PGM}/cm^2, the PtCo@Gnp exhibited an EOL rated power of 11.4 W/mg_{PGM}, greatly exceeding that of Pt/C (3.8 W/mg_{PGM}) (Figure 3.6e). Likewise, the PtCo@Gnp showed a voltage loss as small as 18.8 mV at 0.8 A/cm^2 (meeting the loss < 30 mV DOE target)[28] even at the ultralow PGM loading of 0.070 mg_{PGM}/cm^2, which is nearly one order of magnitude smaller than that of Pt/C (163 mV) or c-PtCo/C (100.8 mV) at the same loading (Figure 3.6f), clearly highlighting the greatly improved stability of the PtCo@Gnp.

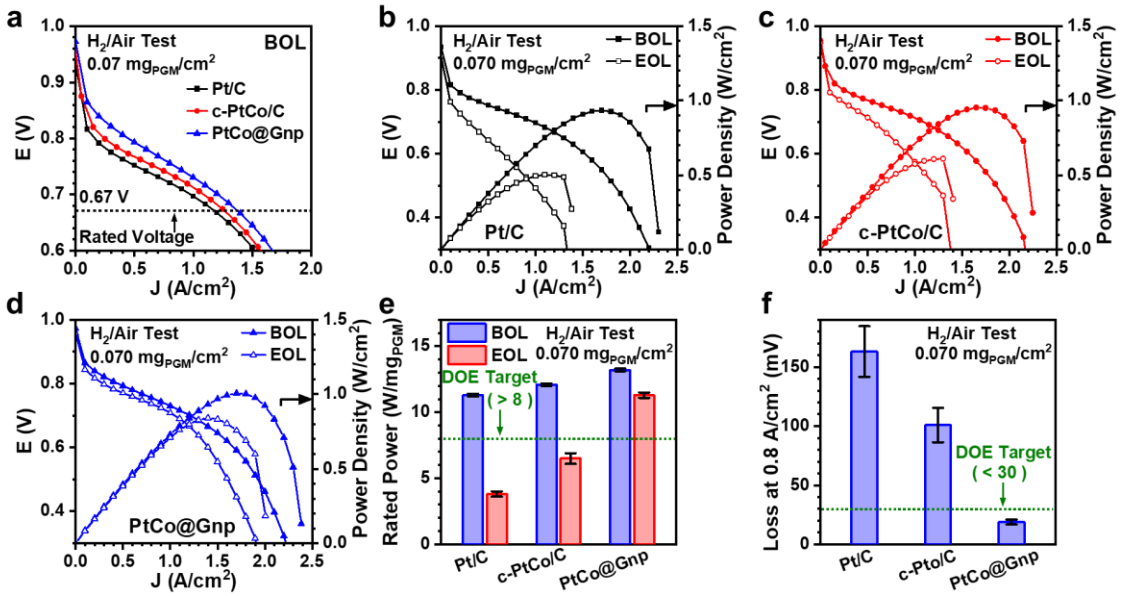

Figure 3. 6. MEAs with ultralow PGM loading (total loading of 0.070 mg_{PGM}/cm^2 including both cathode and anode) tested under H_2/Air. (a-d) The polarization plots. (a) The comparison of Pt/C and PtCo@Gnp at the beginning-of-life (BOL). (b) The comparison of Pt/C at BOL and end-of-life (EOL). (c) The comparison of PtCo at BOL and EOL. (d) The comparison of PtCo@Gnp at BOL and EOL. (e) Rated power of MEA normalized by total PGM loading. (f) The comparison of voltage loss at 0.8 A/cm^2 (EOL vs. BOL). The error bars in (e) and (f) represents the standard deviations. Adapted with permission from Ref.[36] Copyright 2022 Springer Nature

We further note that area-normalized rated power represents another critical parameter for practical applications. At the PGM loading of 0.100 mg_{PGM}/cm^2, the PtCo@Gnp delivers a rated power of 1.01 W/cm^2, satisfying the DOE target (1.0 W/cm^2) and outperforming Pt/C (0.91 W/cm^2). The exceptional durability of the PtCo@Gnp is particularly highlighted by the extraordinary EOL areal rated power. After the ADT, the PtCo@Gnp retained an EOL rated power of 0.87 W/cm^2 at the PGM loading of 0.100 mg_{PGM}/cm^2, greatly outperforming Pt/C (0.57 W/cm^2). Furthermore, at the ultralow PGM loading of 0.070 mg_{PGM}/cm^2, the PtCo@Gnp MEA exhibits a phenomenal EOL areal rated power of 0.80 W/cm^2, far exceeding that of Pt/C (0.27 W/cm^2) or c-PtCo/C (0.52 W/cm^2) at the same loading, demonstrating the extraordinary durability of the PtCo@Gnp even under the much more demanding ultralow PGM loading conditions. To the best of our knowledge, the PtCo@Gnp represents the only catalyst that can work at the highly

demanding ultralow loading conditions with all the EOL performance metrics exceeding the DOE targets.[2, 58] Such greatly improved EOL performance can deliver more uniform power output over the lifetime, desirable for practical applications. Moreover, the greatly improved durability beyond the DOE targets could significantly prolong the fuel cell lifetime by ~50% based on linear extrapolation of MA degradation or voltage loss[59].

Durability Analysis

To understand the substantially different stability between PtCo@Gnp and Pt/C, we further characterized and compared the different catalysts after the ADT in MEA. We have first evaluated the nanoparticle size distribution change before and after ADT. To properly reflect the mass fraction of different-sized particles, we have plotted mass-weighted size distribution. Overall, the mass-weighted size of Pt/C increases dramatically from 5.7 ± 2.0 nm at BOL to 12.2 ± 5.6 nm at EOL (Figure 3.7a, Table 3.1). Similar size increases are also observed in c-PtCo/C (Figure 3.7b, Table 3.1). Such an increase in nanoparticle size can be largely attributed to: (1) nanoparticle detachment, movement, and coalescence, and (2) oxidative dissolution, diffusion, and Ostwald ripening process[32]. To this end, the graphene enclosure can effectively prevent nanoparticle movement and coalescence, as well as greatly retard oxidative dissolution and diffusion by largely retaining the dissolved Pt atoms within the graphene pockets, which may redeposit onto the PtCo nanoparticles thus helping maintain the size of the ultrafine PtCo nanoparticles. Indeed, the mass-weighted average size of the PtCo nanoparticles in PtCo@Gnp only increases moderately from 3.4 ± 1.1 nm at BOL to 5.1 ± 1.7 nm at EOL (Figure 3.7c), clearly highlighting that the presence of graphene nanopockets has effectively restrained the size growth and improved the overall durability of the PtCo nanocatalysts.

Catalyst	Average Size (nm)		
	As Prepared	Beginning-of-life	End-of-life
Pt/C	3.8 ± 1.1	3.9 ± 1.5	5.8 ± 2.9
c-PtCo/C	4.2 ± 1.2	4.3 ± 1.4	5.7 ± 2.4
PtCo@Gnp	2.3 ± 0.7	2.6 ± 0.8	3.6 ± 1.4
	Weighted Average Size (nm)*		
Pt/C	4.9 ± 1.5	5.7 ± 2.0	12.2 ± 5.6
c-PtCo/C	5.7 ± 1.7	5.8 ± 1.8	9.5 ± 4.0
PtCo@Gnp	3.0 ± 0.8	3.4 ± 1.1	5.1 ± 1.7

Table 3. 1. The comparison of analysis results of average size and weighted average size count the mass of each nanoparticle.

The high-resolution STEM image and EDS maps confirmed that the PtCo nanoparticles in PtCo@Gnp retained their core-shell-like structure with a Pt-rich shell at EOL (Figure 3.7d). It is also noted that the protective graphene nanopockets remained on the PtCo nanoparticle, but with reduced space in between (Figure 3.7e, f). It is likely that graphene nanopockets had become more hydrophilic after ADT and collapsed onto the PtCo nanoparticles due to the capillary force during the TEM sample preparation. The much smaller increase of the mass-weighted size in PtCo@Gnp (from 3.4 nm to 5.1 nm) allows for retaining a relatively high ECSA of 32.4 m^2/g_{PGM} at EOL, substantially higher than that of Pt/C (13.2 m^2/g_{PGM}) and c-PtCo/C (13.6 m^2/g_{PGM}) (Figure 3.7g).

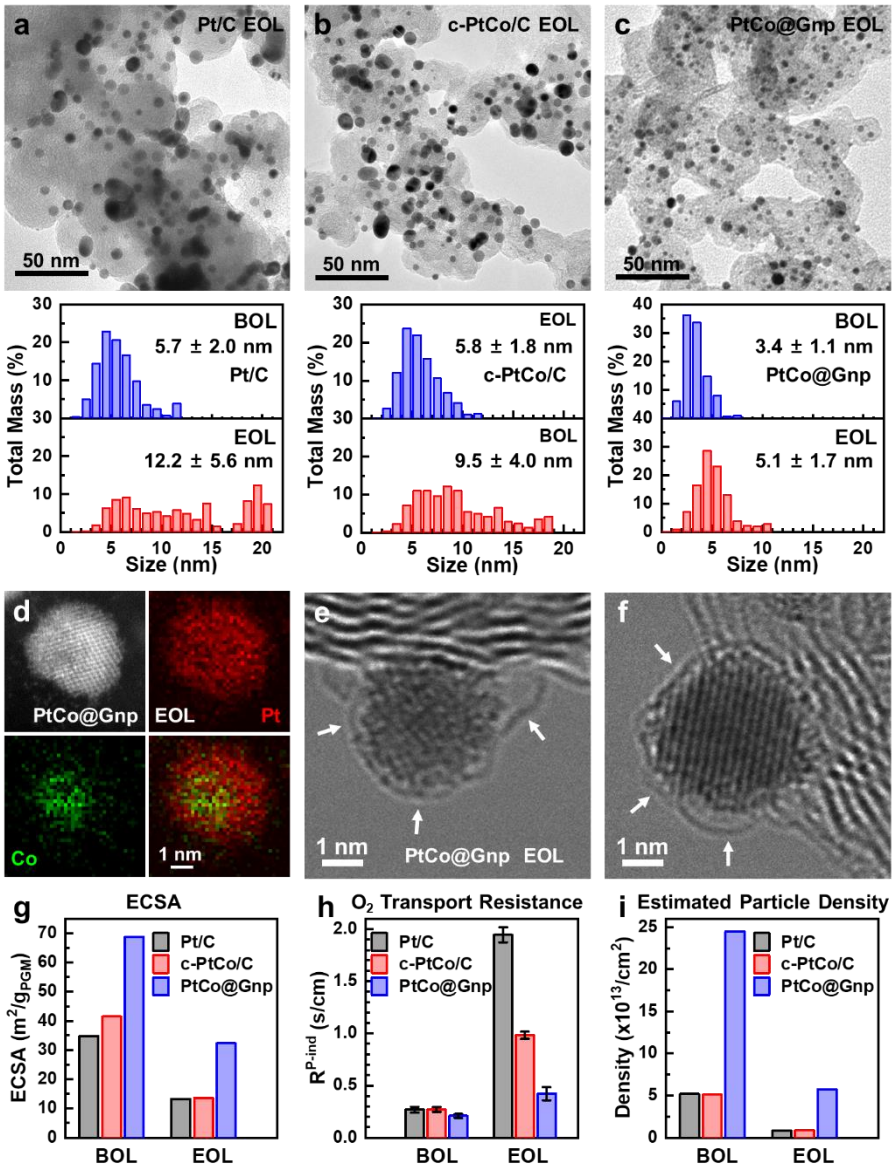

Figure 3. 7. Characterization of catalysts at EOL, analysis of size distribution, and corresponding MEA test results. TEM images of nanocatalysts at EOL, and corresponding mass-weighted size analysis of (a) Pt/C, (b) c-PtCo/C, (c) PtCo@Gnp (d) STEM image, and the corresponding EDS elemental maps of PtCo@Gnp at EOL. (e, f) Bright-field STEM images of PtCo@Gnp at EOL (white arrow indicates the graphene pocket). (g) The comparison of ECSA. (h) Pressure independent oxygen transport resistance for tested MEAs. (i) The estimated nanoparticle per electrode area (particle density) for cathode catalysts. The error bars in panel (h) represent standard error. Adapted with permission from Ref.[36] Copyright 2022 Springer Nature

The ability to retain high ECSA in PtCo@Gnp during fuel cell operations can also be evidenced by the oxygen transport resistance studies since the pressure independent oxygen transport resistance ($R^{P\text{-}Ind}$) of an MEA is inversely linked to the number of active sites per unit

area of the electrode[41-42]. In contrast to the significant increase of $R^{P\text{-}Ind}$ in Pt/C (640%) and c-PtCo/C (265%) MEAs, the PtCo@Gnp MEA showed a much smaller increase of ~100% after the ADT (Figure 3.7h, Figure 3.8). The dramatic increase of $R^{P\text{-}Ind}$ for Pt/C electrode can be attributed to a seriously increased particle size (12.2 nm) and a significantly reduced particle density (from 5.2×10^{13} to $8.1 \times 10^{12}/cm^2$) (see Methods), which lead to significantly increased resistance for oxygen diffusion to reach active sites[30]. In contrast, the PtCo@Gnp retains a relatively smaller size (5.1 nm) and a high particle density ($5.7 \times 10^{13}/cm^2$) at EOL to ensure a sufficiently low $R^{P\text{-}Ind}$, which is essential for long-term stability (Figure 3.7i).

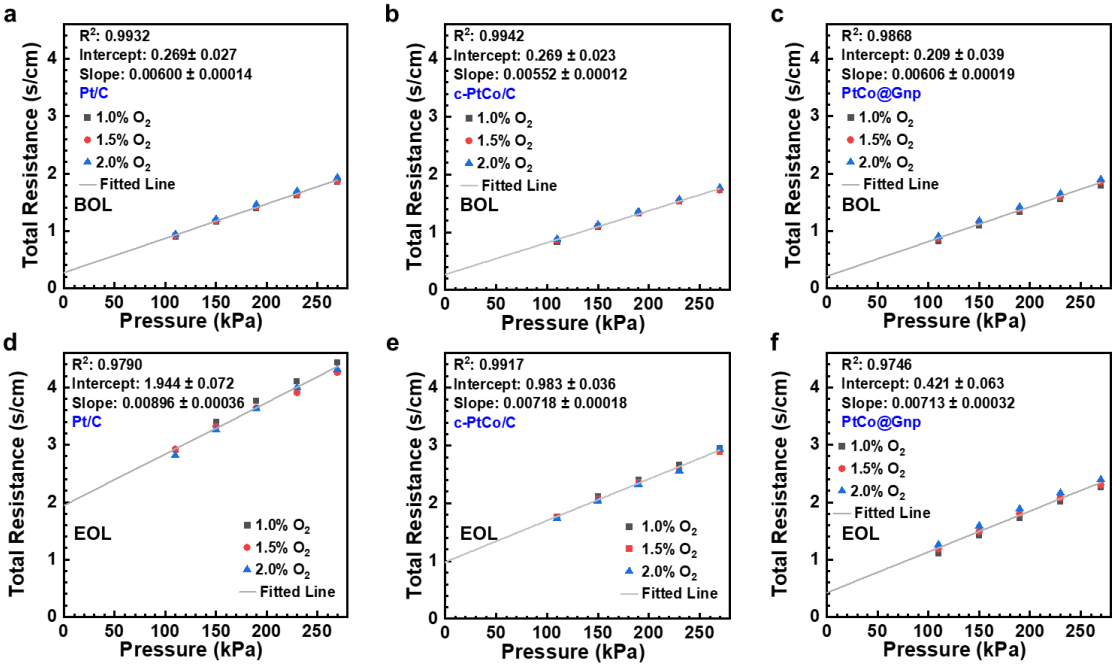

Figure 3. 8. The measured total oxygen transport resistances in an MEA at BOL and EOL were plotted with the total pressure during the measurement. The total loading (anode plus cathode) is 0.070 mg_{PGM}/cm^2. (a) Pt/C BOL, (b) c-PtCo/C BOL, (c) PtCo@Gnp BOL, (d) Pt/C EOL, (e) c-PtCo/C EOL, (f) PtCo@Gnp EOL. The total oxygen transport resistance can be separated into a pressure-dependent part ($R^{P\text{-}d}$) and a pressure-independent part ($R^{P\text{-}ind}$), which represents the Knudsen diffusion and diffusion of oxygen through the ionomer layer in the catalyst layer. Thus, the pressure-independent part is critical for oxygen transport in an operating fuel cell. The relationship of total oxygen resistance (R_{total}), pressure-dependent part of oxygen transport resistance ($R^{P\text{-}d}$), and pressure independent part of oxygen transport resistance ($R^{P\text{-}ind}$) can be expressed in the following equation: $R_{total} = R^{P-d} + R^{P-ind}$. Adapted with permission from Ref.[36] Copyright 2022 Springer Nature

3.4 Conclusion

Together, by encaging ultrafine nanocatalysts in graphene nanopockets, we have created a new design of PtCo@Gnp that shows superior stability against size growth during practical MEA operations. Our design enables highly robust PEMFCs at the ultralow PGM loading conditions (0.070 mg_{PGM}/cm^2), achieving a high mass activity (1.21 A/g_{PGM}), a high rated power of 13.2 W/mg_{PGM}, an extraordinary durability with high MA retention of 73%, and only an 18.8 mV voltage loss at 0.8 A/cm^2 after ADT, all exceeding the relevant DOE targets. With the high rated power and high durability at ultralow PGM loading, the PtCo@Gnp can promise to substantially reduce the needed PGM in a 90-kW FCV to around 6.8 g, which is comparable to the PGM loading in the typical catalytic converters for ICE powered vehicles (Figure 3.9). It is well recognized that the system cost and durability represent the two most critical roadblocks to the widespread adoption of PEMFCs[60]. Our study addresses exactly these critical challenges and marks a critical step toward the substantial reduction of PGM loading (thus the cost) while retaining extraordinary durability in practical fuel cells for more widespread adoption.

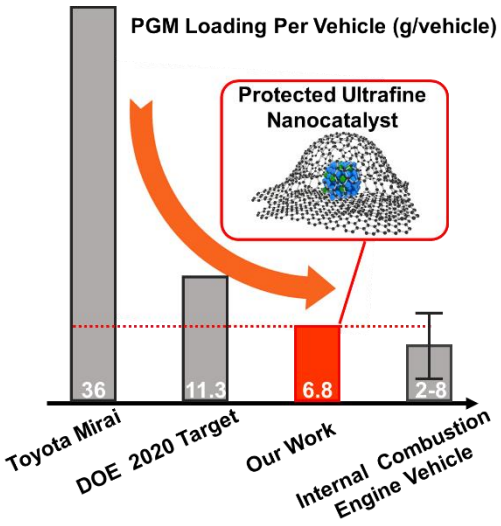

Figure 3. 9. Comparison of the needed PGM in Toyota Mairi or a 90-kW FCV based on DOE target, or our catalyst design, and that in an internal combustion engine powered vehicle. Adapted with permission from Ref.[36] Copyright 2022 Springer Nature

3.5 References

1. Debe, M. K., Electrocatalyst Approaches and Challenges for Automotive Fuel Cells. *Nature* 2012, **486**, 43-51 doi:10.1038/nature11115

2. Yarlagadda, V.; Carpenter, M. K.; Moylan, T. E.; Kukreja, R. S.; Koestner, R.; Gu, W.; Thompson, L.; Kongkanand, A., Boosting Fuel Cell Performance with Accessible Carbon Mesopores. *ACS Energy Letters* 2018, **3**, 618-621 doi:10.1021/acsenergylett.8b00186

3. Tollefson, J., Worth Its Weight in Platinum. *Nature* 2007, **450**, 334-335

4. Bossi, T.; Gediga, J., The Environmental Profile of Platinum Group Metals. *Johnson Matthey Technology Review* 2017, **61**, 111-121

5. James, B. D.; Huya-Kouadio, J. M.; Houchins, C.; DeSantis, D. A. *Mass Production Cost Estimation of Direct H_2 Pem Fuel Cell Systems for Transportation Applications: 2018 Update*; US Department of Energy, 2018.

6. Pollet, B. G.; Kocha, S. S.; Staffell, I., Current Status of Automotive Fuel Cells for Sustainable Transport. *Current Opinion in Electrochemistry* 2019, **16**, 90-95 doi:https://doi.org/10.1016/j.coelec.2019.04.021

7. Gröger, O.; Gasteiger, H. A.; Suchsland, J.-P., Electromobility: Batteries or Fuel Cells? *Journal of The Electrochemical Society* 2015, **162**, A2605-A2622 doi:10.1149/2.0211514jes

8. Hao, H.; Geng, Y.; Tate, J. E.; Liu, F.; Sun, X.; Mu, Z.; Xun, D.; Liu, Z.; Zhao, F., Securing Platinum-Group Metals for Transport Low-Carbon Transition. *One Earth* 2019, **1**, 117-125 doi:https://doi.org/10.1016/j.oneear.2019.08.012

9. Kongkanand, A.; Mathias, M. F., The Priority and Challenge of High-Power Performance of Low-Platinum Proton-Exchange Membrane Fuel Cells. *The Journal of Physical Chemistry Letters* 2016, **7**, 1127-1137 doi:10.1021/acs.jpclett.6b00216

10. Li, M.; Zhao, Z.; Cheng, T.; Fortunelli, A.; Chen, C.-Y.; Yu, R.; Zhang, Q.; Gu, L.; Merinov, B. V.; Lin, Z.; Zhu, E.; Yu, T.; Jia, Q.; Guo, J.; Zhang, L.; Goddard, W. A.; Huang, Y.; Duan, X., Ultrafine Jagged Platinum Nanowires Enable Ultrahigh Mass Activity for the Oxygen Reduction Reaction. *Science* 2016, **354**, 1414-1419 doi:10.1126/science.aaf9050

11. Escudero-Escribano, M.; Malacrida, P.; Hansen, M. H.; Vej-Hansen, U. G.; Velázquez-Palenzuela, A.; Tripkovic, V.; Schiøtz, J.; Rossmeisl, J.; Stephens, I. E. L.; Chorkendorff, I., Tuning the Activity of Pt Alloy Electrocatalysts by Means of the Lanthanide Contraction. *Science* 2016, **352**, 73-76 doi:10.1126/science.aad8892

12. Chen, C.; Kang, Y.; Huo, Z.; Zhu, Z.; Huang, W.; Xin, H. L.; Snyder, J. D.; Li, D.; Herron, J. A.; Mavrikakis, M.; Chi, M.; More, K. L.; Li, Y.; Markovic, N. M.; Somorjai, G. A.; Yang, P.; Stamenkovic, V. R., Highly Crystalline Multimetallic Nanoframes with Three-Dimensional Electrocatalytic Surfaces. *Science* 2014, **343**, 1339-1343 doi:10.1126/science.1249061

13. Greeley, J.; Stephens, I. E. L.; Bondarenko, A. S.; Johansson, T. P.; Hansen, H. A.; Jaramillo, T. F.; Rossmeisl, J.; Chorkendorff, I.; Nørskov, J. K., Alloys of Platinum and Early Transition Metals as Oxygen Reduction Electrocatalysts. *Nature Chemistry* 2009, **1**, 552-556 doi:10.1038/nchem.367

14. Zhang, L.; Roling, L. T.; Wang, X.; Vara, M.; Chi, M.; Liu, J.; Choi, S.-I.; Park, J.; Herron, J. A.; Xie, Z.; Mavrikakis, M.; Xia, Y., Platinum-Based Nanocages with Subnanometer-Thick Walls and Well-Defined, Controllable Facets. *Science* 2015, **349**, 412-416 doi:10.1126/science.aab0801

15. Cui, C.; Gan, L.; Heggen, M.; Rudi, S.; Strasser, P., Compositional Segregation in Shaped Pt Alloy Nanoparticles and Their Structural Behaviour During Electrocatalysis. *Nature Materials* 2013, **12**, 765-771 doi:10.1038/nmat3668

16. Seh, Z. W.; Kibsgaard, J.; Dickens, C. F.; Chorkendorff, I.; Nørskov, J. K.; Jaramillo, T. F., Combining Theory and Experiment in Electrocatalysis: Insights into Materials Design. *Science* 2017, **355**, eaad4998 doi:10.1126/science.aad4998

17. Li, W.; Chen, Z.; Xu, L.; Yan, Y., A Solution-Phase Synthesis Method to Highly Active Pt-Co/C Electrocatalysts for Proton Exchange Membrane Fuel Cell. *Journal of Power Sources* 2010, **195**, 2534-2540 doi:https://doi.org/10.1016/j.jpowsour.2009.11.035

18. Zhang, Z.; Luo, Z.; Chen, B.; Wei, C.; Zhao, J.; Chen, J.; Zhang, X.; Lai, Z.; Fan, Z.; Tan, C.; Zhao, M.; Lu, Q.; Li, B.; Zong, Y.; Yan, C.; Wang, G.; Xu, Z. J.; Zhang, H., One-Pot Synthesis of Highly Anisotropic Five-Fold-Twinned Ptcu Nanoframes Used as a Bifunctional Electrocatalyst for Oxygen Reduction and Methanol Oxidation. *Advanced Materials* 2016, **28**, 8712-8717 doi:https://doi.org/10.1002/adma.201603075

19. Wang, X. X.; Hwang, S.; Pan, Y.-T.; Chen, K.; He, Y.; Karakalos, S.; Zhang, H.; Spendelow, J. S.; Su, D.; Wu, G., Ordered Pt3co Intermetallic Nanoparticles Derived from Metal–Organic Frameworks for Oxygen Reduction. *Nano Letters* 2018, **18**, 4163-4171 doi:10.1021/acs.nanolett.8b00978

20. Huang, L.; Zheng, C. Y.; Shen, B.; Mirkin, C. A., High-Index-Facet Metal-Alloy Nanoparticles as Fuel Cell Electrocatalysts. *Advanced Materials* 2020, **32**, 2002849 doi:https://doi.org/10.1002/adma.202002849

21. Ott, S.; Orfanidi, A.; Schmies, H.; Anke, B.; Nong, H. N.; Hübner, J.; Gernert, U.; Gliech, M.; Lerch, M.; Strasser, P., Ionomer Distribution Control in Porous Carbon-Supported Catalyst Layers for High-Power and Low Pt-Loaded Proton Exchange Membrane Fuel Cells. *Nature Materials* 2019, **19**, 77-85 doi:https://doi.org/10.1038/s41563-019-0487-0

22. Qiao, Z.; Hwang, S.; Li, X.; Wang, C.; Samarakoon, W.; Karakalos, S.; Li, D.; Chen, M.; He, Y.; Wang, M.; Liu, Z.; Wang, G.; Zhou, H.; Feng, Z.; Su, D.; Spendelow, J. S.; Wu, G., 3d Porous Graphitic Nanocarbon for Enhancing the Performance and Durability of Pt Catalysts: A Balance between Graphitization and Hierarchical Porosity. *Energy & Environmental Science* 2019, **12**, 2830-2841 doi:10.1039/C9EE01899A

23. Wang, L.; Zeng, Z.; Gao, W.; Maxson, T.; Raciti, D.; Giroux, M.; Pan, X.; Wang, C.; Greeley, J., Tunable Intrinsic Strain in Two-Dimensional Transition Metal Electrocatalysts. *Science* 2019, **363**, 870-874 doi:10.1126/science.aat8051

24. Wang, C.; Chi, M.; Li, D.; van der Vliet, D.; Wang, G.; Lin, Q.; Mitchell, J. F.; More, K. L.; Markovic, N. M.; Stamenkovic, V. R., Synthesis of Homogeneous Pt-Bimetallic Nanoparticles as Highly Efficient Electrocatalysts. *ACS Catalysis* 2011, **1**, 1355-1359 doi:10.1021/cs200328z

25. He, D. S.; He, D.; Wang, J.; Lin, Y.; Yin, P.; Hong, X.; Wu, Y.; Li, Y., Ultrathin Icosahedral Pt-Enriched Nanocage with Excellent Oxygen Reduction Reaction Activity. *Journal of the American Chemical Society* 2016, **138**, 1494-1497 doi:10.1021/jacs.5b12530

26. Pizzutilo, E.; Knossalla, J.; Geiger, S.; Grote, J.-P.; Polymeros, G.; Baldizzone, C.; Mezzavilla, S.; Ledendecker, M.; Mingers, A.; Cherevko, S.; Schüth, F.; Mayrhofer, K. J. J., The Space Confinement Approach Using Hollow Graphitic Spheres to Unveil Activity and Stability of Pt-Co Nanocatalysts for Pemfc. *Advanced Energy Materials* 2017, **7**, 1700835 doi:https://doi.org/10.1002/aenm.201700835

27. Mezzavilla, S.; Baldizzone, C.; Swertz, A.-C.; Hodnik, N.; Pizzutilo, E.; Polymeros, G.; Keeley, G. P.; Knossalla, J.; Heggen, M.; Mayrhofer, K. J. J.; Schüth, F., Structure–Activity–Stability Relationships for Space-Confined Ptxniy Nanoparticles in the Oxygen Reduction Reaction. *ACS Catalysis* 2016, **6**, 8058-8068 doi:10.1021/acscatal.6b02221

28. Doe Technical Targets for Polymer Electrolyte Membrane Fuel Cell Components. https://energy.gov/eere/fuelcells/doe-technical-targets-polymer-electrolyte-membrane-fuel-cell-components (accessed June 11).

29. Kodama, K.; Nagai, T.; Kuwaki, A.; Jinnouchi, R.; Morimoto, Y., Challenges in Applying Highly Active Pt-Based Nanostructured Catalysts for Oxygen Reduction Reactions to Fuel Cell Vehicles. *Nature Nanotechnology* 2021, **16**, 140-147 doi:10.1038/s41565-020-00824-w

30. Weber, A. Z.; Kusoglu, A., Unexplained Transport Resistances for Low-Loaded Fuel-Cell Catalyst Layers. *Journal of Materials Chemistry A* 2014, **2**, 17207-17211 doi:10.1039/C4TA02952F

31. Holby, E. F.; Sheng, W.; Shao-Horn, Y.; Morgan, D., Pt Nanoparticle Stability in Pem Fuel Cells: Influence of Particle Size Distribution and Crossover Hydrogen. *Energy & Environmental Science* 2009, **2**, 865-871 doi:10.1039/B821622N

32. Borup, R. L.; Kusoglu, A.; Neyerlin, K. C.; Mukundan, R.; Ahluwalia, R. K.; Cullen, D. A.; More, K. L.; Weber, A. Z.; Myers, D. J., Recent Developments in Catalyst-Related Pem Fuel Cell Durability. *Current Opinion in Electrochemistry* 2020, **21**, 192-200 doi:https://doi.org/10.1016/j.coelec.2020.02.007

33. Tang, L.; Li, X.; Cammarata, R. C.; Friesen, C.; Sieradzki, K., Electrochemical Stability of Elemental Metal Nanoparticles. *Journal of the American Chemical Society* 2010, **132**, 11722-11726 doi:10.1021/ja104421t

34. Tang, L.; Han, B.; Persson, K.; Friesen, C.; He, T.; Sieradzki, K.; Ceder, G., Electrochemical Stability of Nanometer-Scale Pt Particles in Acidic Environments. *Journal of the American Chemical Society* 2010, **132**, 596-600 doi:10.1021/ja9071496

35. Du, L.; Prabhakaran, V.; Xie, X.; Park, S.; Wang, Y.; Shao, Y., Low-Pgm and Pgm-Free Catalysts for Proton Exchange Membrane Fuel Cells: Stability Challenges and Material Solutions. *Advanced Materials* 2021, **33**, 1908232 doi:https://doi.org/10.1002/adma.201908232

36. Zhao, Z.; Liu, Z.; Zhang, A.; Yan, X.; Xue, W.; Peng, B.; Xin, H. L.; Pan, X.; Duan, X.; Huang, Y., Graphene-Nanopocket-Encaged Ptco Nanocatalysts for Highly Durable Fuel Cell Operation under Demanding Ultralow-Pt-Loading Conditions. *Nature Nanotechnology* 2022, doi:10.1038/s41565-022-01170-9

37. Zhao, Z.; Hossain, M. D.; Xu, C.; Lu, Z.; Liu, Y.-S.; Hsieh, S.-H.; Lee, I.; Gao, W.; Yang, J.; Merinov, B. V.; Xue, W.; Liu, Z.; Zhou, J.; Luo, Z.; Pan, X.; Zaera, F.; Guo, J.; Duan, X.; Goddard, W. A.; Huang, Y., Tailoring a Three-Phase Microenvironment for High-Performance Oxygen Reduction Reaction in Proton Exchange Membrane Fuel Cells. *Matter* 2020, **3**, 1774-1790 doi:https://doi.org/10.1016/j.matt.2020.09.025

38. Huang, P. Y.; Ruiz-Vargas, C. S.; van der Zande, A. M.; Whitney, W. S.; Levendorf, M. P.; Kevek, J. W.; Garg, S.; Alden, J. S.; Hustedt, C. J.; Zhu, Y.; Park, J.; McEuen, P. L.; Muller, D. A., Grains and Grain Boundaries in Single-Layer Graphene Atomic Patchwork Quilts. *Nature* 2011, **469**, 389-392 doi:10.1038/nature09718

39. Stariha, S.; Macauley, N.; Sneed, B. T.; Langlois, D.; More, K. L.; Mukundan, R.; Borup, R. L., Recent Advances in Catalyst Accelerated Stress Tests for Polymer Electrolyte Membrane Fuel Cells. *Journal of The Electrochemical Society* 2018, **165**, F492-F501 doi:10.1149/2.0881807jes

40. Garrick, T. R.; Moylan, T. E.; Carpenter, M. K.; Kongkanand, A., Electrochemically Active Surface Area Measurement of Aged Pt Alloy Catalysts in Pem Fuel Cells by Co Stripping. *Journal of The Electrochemical Society* 2016, **164**, F55-F59 doi:10.1149/2.0381702jes

41. Garsany, Y.; Atkinson, R. W.; Gould, B. D.; Swider-Lyons, K. E., High Power, Low-Pt Membrane Electrode Assemblies for Proton Exchange Membrane Fuel Cells. *Journal of Power Sources* 2018, **408**, 38-45 doi:https://doi.org/10.1016/j.jpowsour.2018.10.073

42. Baker, D. R.; Caulk, D. A.; Neyerlin, K. C.; Murphy, M. W., Measurement of Oxygen Transport Resistance in Pem Fuel Cells by Limiting Current Methods. *Journal of The Electrochemical Society* 2009, **156**, B991-B1003 doi:10.1149/1.3152226

43. Han, B.; Carlton, C. E.; Kongkanand, A.; Kukreja, R. S.; Theobald, B. R.; Gan, L.; O'Malley, R.; Strasser, P.; Wagner, F. T.; Shao-Horn, Y., Record Activity and Stability of Dealloyed Bimetallic Catalysts for Proton Exchange Membrane Fuel Cells. *Energy & Environmental Science* 2015, **8**, 258-266 doi:10.1039/C4EE02144D

44. Braaten, J. P.; Xu, X.; Cai, Y.; Kongkanand, A.; Litster, S., Contaminant Cation Effect on Oxygen Transport through the Ionomers of Polymer Electrolyte Membrane Fuel Cells. *Journal of The Electrochemical Society* 2019, **166**, F1337-F1343 doi:10.1149/2.0671916jes

45. Sulek, M.; Adams, J.; Kaberline, S.; Ricketts, M.; Waldecker, J. R., In Situ Metal Ion Contamination and the Effects on Proton Exchange Membrane Fuel Cell Performance. *Journal of Power Sources* 2011, **196**, 8967-8972 doi:https://doi.org/10.1016/j.jpowsour.2011.01.086

46. Hoene, J. V.; Charles, R. G.; Hickam, W. M., Thermal Decomposition of Metal Acetylacetonates: Mass Spectrometer Studies. *The Journal of Physical Chemistry* 1958, **62**, 1098-1101 doi:10.1021/j150567a019

47. Grimm, S.; Baik, S.-J.; Hemberger, P.; Bodi, A.; Kempf, A. M.; Kasper, T.; Atakan, B., Gas-Phase Aluminium Acetylacetonate Decomposition: Revision of the Current Mechanism by Vuv Synchrotron Radiation. *Physical Chemistry Chemical Physics* 2021, **23**, 15059-15075 doi:10.1039/D1CP00720C

48. Fei, L.-f.; Sun, T.-y.; Lu, W.; An, X.-q.; Hu, Z.-f.; Yu, J. C.; Zheng, R.-k.; Li, X.-m.; Chan, H. L. W.; Wang, Y., Direct Observation of Carbon Nanostructure Growth at Liquid–Solid Interfaces. *Chemical Communications* 2014, **50**, 826-828 doi:10.1039/C3CC46264A

49. Picher, M.; Lin, P. A.; Gomez-Ballesteros, J. L.; Balbuena, P. B.; Sharma, R., Nucleation of Graphene and Its Conversion to Single-Walled Carbon Nanotubes. *Nano Letters* 2014, **14**, 6104-6108 doi:10.1021/nl501977b

50. Fan, H.; Qiu, L.; Fedorov, A.; Willinger, M.-G.; Ding, F.; Huang, X., Dynamic State and Active Structure of Ni–Co Catalyst in Carbon Nanofiber Growth Revealed by in Situ Transmission Electron Microscopy. *ACS Nano* 2021, **15**, 17895-17906 doi:10.1021/acsnano.1c06189

51. Cullen, D. A.; Neyerlin, K. C.; Ahluwalia, R. K.; Mukundan, R.; More, K. L.; Borup, R. L.; Weber, A. Z.; Myers, D. J.; Kusoglu, A., New Roads and Challenges for Fuel Cells in Heavy-Duty Transportation. *Nature Energy* 2021, **6**, 462-474 doi:10.1038/s41560-021-00775-z

52. Chong, L.; Wen, J.; Kubal, J.; Sen, F. G.; Zou, J.; Greeley, J.; Chan, M.; Barkholtz, H.; Ding, W.; Liu, D.-J., Ultralow-Loading Platinum-Cobalt Fuel Cell Catalysts Derived from Imidazolate Frameworks. *Science* 2018, **362**, 1276-1281 doi:10.1126/science.aau0630

53. Jia, Q.; Caldwell, K.; Strickland, K.; Ziegelbauer, J. M.; Liu, Z.; Yu, Z.; Ramaker, D. E.; Mukerjee, S., Improved Oxygen Reduction Activity and Durability of Dealloyed Ptcox Catalysts for Proton Exchange Membrane Fuel Cells: Strain, Ligand, and Particle Size Effects. *ACS Catalysis* 2015, **5**, 176-186 doi:10.1021/cs501537n

54. Li, J.; Sharma, S.; Liu, X.; Pan, Y.-T.; Spendelow, J. S.; Chi, M.; Jia, Y.; Zhang, P.; Cullen, D. A.; Xi, Z.; Lin, H.; Yin, Z.; Shen, B.; Muzzio, M.; Yu, C.; Kim, Y. S.; Peterson, A. A.; More, K. L.; Zhu, H.; Sun, S., Hard-Magnet L10-Copt Nanoparticles Advance Fuel Cell Catalysis. *Joule* 2019, **3**, 124-135 doi:https://doi.org/10.1016/j.joule.2018.09.016

55. Papadias, D. D.; Ahluwalia, R. K.; Kariuki, N.; Myers, D.; More, K. L.; Cullen, D. A.; Sneed, B. T.; Neyerlin, K. C.; Mukundan, R.; Borup, R. L., Durability of Pt-Co Alloy Polymer Electrolyte Fuel Cell Cathode Catalysts under Accelerated Stress Tests. *Journal of The Electrochemical Society* 2018, **165**, F3166-F3177 doi:10.1149/2.0171806jes

56. Slack, J. J.; Gumeci, C.; Dale, N.; Parrondo, J.; Macauley, N.; Mukundan, R.; Cullen, D.; Sneed, B.; More, K.; Pintauro, P. N., Nanofiber Fuel Cell Meas with a Ptco/C Cathode. *Journal of The Electrochemical Society* 2019, **166**, F3202-F3209 doi:10.1149/2.0151907jes

57. Fuel Cell Technologies Office Multi-Year Research, Development, and Demonstration Plan. https://www.energy.gov/eere/fuelcells/downloads/fuel-cell-technologies-office-multi-year-research-development-and-22 (accessed June 11).

58. Zhao, Z.; Chen, C.; Liu, Z.; Huang, J.; Wu, M.; Liu, H.; Li, Y.; Huang, Y., Pt-Based Nanocrystal for Electrocatalytic Oxygen Reduction. *Advanced Materials* 2019, **31**, 1808115 doi:10.1002/adma.201808115

59. Kleen, G.; Padgett, E. *Durability-Adjusted Fuel Cell System Cost*; US Department of Energy, 2021.

60. Papageorgopoulos, D. *Fuel Cell R&D Overview*; US Department of Energy, 2019.

Chapter 4. Ultrafine Pt Nanoparticles with Endohedral Oxide Clusters for Highly Durable Fuel Cells

4.1 Introduction

To ensure the competitiveness of PEMFCs against conventional vehicles running on fossil fuels, the US Department of Energy (DOE) has set a series of technical targets for PEMFC catalysts in light-duty vehicles.[1] For typical transportation applications, fuel cell performances at low current density (LCD) and high current density (HCD) regimes are both critical to ensure the conversion efficiency and sufficient power output under different operation scenarios. Specifically, the performance in the kinetic-dominated LCD region strongly affects the fuel efficiency in vehicle applications, since the cells predominantly (90% of the time) operate in a low-power mode during cruising,[2] while the performance in HCD regime determines the maximum power output available for the start-up or aggressive acceleration [3], and generally dictates performance retention and the PEMFC lifetime. Performance retention is critical, especially for the emerging heavy-duty vehicle applications, as it also affects the average fuel economy and the total cost of the fuel cell system throughout the required service period.[4-5]

Despite the great progress in ORR catalysts in the past decades, the key performance metrics of PEMFEC catalysts (e.g., activity vs. lifetime durability) is difficult to achieve simultaneously due to the intrinsic trade-off relationships. These challenges have motivated immense efforts to improve the catalyst activity and durability.[6-15] In particular, various nanostructured (nanowires, nanoframes, nanocages, core-shell, etc.) Pt-based alloy (Pt-M, M = Co, Ni, etc.) catalysts with tailored strain and ligand effects have been explored to modulate the oxygen binding energy and the ORR catalytic activity.[16-17] However, the application of these elaborate designs in practical fuel cells is commonly challenged by their limited stability and/or

difficulties in mass production.[3] For example, the Ostwald ripening of typical nanostructured catalysts could lead to rapid loss of electrochemical surface area (ECSA) and overall mass activity (MA). The Pt-M alloy catalysts often suffer from additional durability penalties associated with the dissolution of non-precious metal cations [3, 5, 18], which could occupy the proton sites in the ionomers and lead to cation poisoning effects [19-21] that substantially impede mass transport and compromise the fuel cell performance. To this end, it has been shown that structurally ordered intermetallic Pt-M alloys could improve stability and deliver satisfactory MA retention (> 60%) in LCD region. However, the metal leaching and the associated cation poisoning effects remain a persistent challenge [5, 21], particularly in the HCD region where mass transport could dominate the device performance, as highlighted by an unsatisfactory rated power loss (>10%). [12, 22-27]

Considerable efforts have been made to mitigate metal leaching and cation poisoning effects in Pt-M alloy catalysts.[3, 28-31] For example, it has been shown that oxide-supported Pt catalysts can exhibit improved activity and stability due to the strong metal-oxide interaction [30, 32-33]. Although the role of the oxide support in modifying the electronic structure and stabilizing the Pt has been well corroborated [32, 34], the typically poor conductivity and limited stability of the oxide support itself under acidic conditions prevent its practical implementation in PEMFCs [35].

Inspired by these pioneering studies, herein we report a unique design of ultrafine Pt nanocatalysts with embedded atomically dispersed Co oxide clusters to form a CoO_x@Pt core-shell nanostructure as a highly durable ORR electrocatalyst in PEMFCs (Figure 4.1a, b). This endohedral-oxide design takes full advantage of the strong Pt-oxide interaction to modify the electronic structure of Pt, thus simultaneously (i) suppressing the Pt atom dissolution, and (ii) enhancing the catalytic activity. Meanwhile, with the unstable and less conductive oxide species fully enclosed by the metallic Pt shells, this design also effectively (i) mitigates the CoO_x

dissolution and the consequent cation poisoning effect, and (ii) bypasses the charge transport limitations of typical oxide support (Figure 4.1b).

These combined merits deliver superior PEMFC performance and durability. With the embedded CoO_x retarding Pt leaching and Oswald ripening, the resulting CoO_x@Pt exhibits extraordinary stability at an ultrafine size (≈1.5 nm) and displays a compressive surface strain to enable superior performance compared to commercial Pt or PtCo alloy catalysts. The membrane electrode assembly (MEA) made with the CoO_x@Pt nanocatalyst demonstrates an outstanding initial MA of 1.10 A/mg_{PGM} and a high rated power density of 1.04 W/cm^2 (10.4 W/mg_{PGM}) at only 0.10 mg/cm^2 total PGM loading. With minimized metal dissolution, the developed MEAs deliver the best durability reported to date: achieving an MA retention of 88.2%, a voltage loss of only 13.3 mV at 0.8 A/cm^2, and an exceptionally small rated-power loss of 7.5% after the accelerated degradation test (ADT), greatly exceeding the relevant DOE technical targets.[1] The exceptional durability makes the CoO_x@Pt nanocatalyst a highly promising material especially for heavy-duty fuel cell applications, where the catalyst durability represents a most critical roadblock.

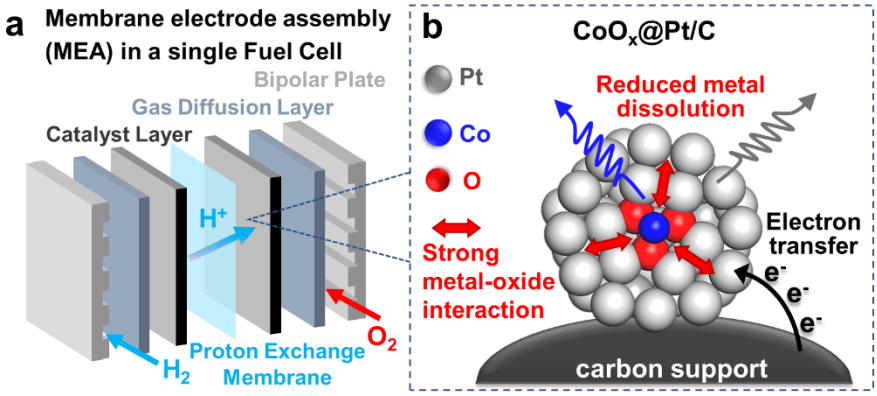

Figure 4. 1. Comparison of the needed PGM in Toyota Mairi or a 90-kW FCV based on DOE target, or our catalyst design, and that in an internal combustion engine powered vehicle.

4.2 Experimental and Computational Methods

Materials and Chemicals

Platinum(II) acetylacetonate [$Pt(acac)_2$], aquivion D83-06A ionomer dispersion were purchased from Sigma Aldrich. Cobalt(II) acetylacetonate [$Co(acac)_2$], 10% Pt/C (weight ratio of Pt: 10%), Pt/C (weight ratio of Pt: 40%) were purchased from Alfa Aesar. Commercial PtCo/C (c-PtCo/C) catalyst was purchased from Premetek. Acetone and isopropanol (IPA) were purchased from Fisher Scientific. Freudenberg H14C7 gas diffusion layer (GDL) and polytetrafluoroethylene (PTFE) gasket were purchased from Fuel Cell Store. Carbon support (Ketjenblack EC-300J) was purchased from Fitz Chem LLC. The water was Ultrapure Millipore (18.2 MΩ·cm)

Synthesis of CoO_x@Pt/C

The carbon support (Ketjenblack EC-300J) was activated in hydrogen (H_2)/argon (Ar) mixture before use as noted in the literature[36]. A typical synthesis includes 150-180 mg carbon support, 150-170 mg $Pt(acac)_2$, 150-160 mg $Co(acac)_2$, and 15ml acetone were mixed under ultrasonication for 20 minutes. After acetone evaporation, the resultant metal precursor adsorbed carbon support was collected, and then annealed in a quartz tube in Ar gas tube, whereby the temperature is heated from room temperature (20 °C) to 250 °C and maintained at 250 °C for 8 hours. The sample was collected after it was cooled to room temperature. Then the obtained powder was washed in N_2-saturated 0.05M H_2SO_4 solution at 80 °C for 12-16 h. After acid washing, the catalyst was rinsed with ultrapure water till the pH was neutral and collected *via* centrifugation. After thoroughly drying in a vacuum, the obtained catalyst was further annealed in H_2/Ar mixture at 180 °C for 1.5 h. After cooled down to room temperature, the sample collected was the CoO_x@Pt/C catalyst, which was ready for the test.

Structure and Composition Characterization

Transmission electron microscopy (TEM) images were taken with a JEOL JEM 2800 transmission electron microscope operated at 200 kV. Atomic resolution high angle annular dark-

field (HAADF) images, as well as energy-dispersive spectroscopy (EDS) maps, were taken using a JEOL Grand ARM300CF scanning/transmission electron microscopy (S/TEM) operated at 300 kV. The TEM/STEM sample grids were prepared by dispersing the sample in a mixture of water and ethanol, then drop casting the dispersion onto lacey carbon film coated copper grids (for high-resolution STEM and EDS analysis) using a pipette and drying under ambient conditions. The concentration of catalysts was determined by inductively coupled plasma atomic emission spectroscopy (ICP-AES, Shimadzu ICPE-9000) as well as by EDS coupled in JEOL Grand ARM300CF. X-ray powder diffraction (XRD) patterns were collected with a Panalytical X'Pert Pro X-ray powder diffractometer with Cu-Kα radiation. X-ray photoelectron spectroscopy (XPS) tests were done with Kratos AXIS Ultra DLD spectrometer. XPS depth profiling was conducted using the instrument's Ar^+ ion source operated at 4kV, 50uA, and rastered over a 3×3 mm area for 4 minutes. The atomic composition was determined based on photoelectron peak areas and the relative sensitivity factors provided in CasaXPS.

X-ray Absorption Spectroscopy (XAS) Data Collection and Analysis

The electrode inks for the XAS electrodes were composed of 60% ethanol, 40% water, 5 wt % Nafion solution, and the catalyst powder. The ink was spray-coated onto a carbon paper with a total catalyst loading about 12.5 mg/cm^2 (with Co loading of 0.05 mg/cm^2 and Pt loading of 2.7 mg/cm^2). The XAS experiments were conducted at room temperature in an *in-situ* spectro-electrochemical half-cell circulated with a continuously O_2 purged 0.1 M $HClO_4$ aqueous solution[37], at the beamline ISS 6-BM and 8-ID in National Synchrotron Light Source II (NSLS-II) (Brookhaven National Laboratory, NY). Before being transferred into the cell, the electrodes were conditioned in 0.1 M $HClO_4$ under vacuum for 40 minutes without applying the potential to remove surface contaminants. Potentiostatic control was maintained with an Autolab PGSTAT30

potentiostat (Metrohm USA, formerly Brinkman Instruments). Data were collected on the same electrode in transmission mode at the Pt L_3-edge, and fluorescence mode at the Co K-edge, with a Pt/Co reference foil positioned between I2 and I3 as a reference. The voltage cycling limits were 0.05 to 1.00 V vs. RHE. Data collection was performed at the chosen potentials held during anodic sweeps. The electrode was fully cycled following each potential hold to clean the electrode surfaces after each potential hold. Typical experimental procedures were utilized with details provided in previous work [38]. The data were processed and fitted using the Ifeffit–based Athena [39] and Artemis [40] programs. Scans were calibrated, aligned, and normalized with background removed using the IFEFFIT suite.[41] The $\chi(R)$ were modeled using single scattering paths calculated by FEFF6.[42]

MEA Preparation and Single Fuel Cell Test

The MEA fabrication followed the protocol in the previous work of our group.[43] The catalyst ink was made by mixing the catalysts with the ionomer solution (Aquivion D83-06A) and water-IPA solvent through ultrasonication. The catalyst ink was then spray-coated onto a reinforced perfluorosulfonic acid (PFSA) membrane (12 μm thickness) using a Sono-Tek ultrasonic spray system to form a catalyst-coated membrane (CCM).

For a fair comparison, cell components and fabrication conditions were the same in all MEAs except for the cathode catalysts. Accordingly, the MEAs were labeled by the cathode catalysts. The anode catalyst was the commercial 10% Pt/C with platinum group metal (PGM) loading fixed to be 0.01 mg_{PGM}/cm^2. The anode ionomer to carbon mass ratio was 0.6. The commercial 40% Pt/C (c-Pt/C) and 40% PtCo/C (c-PtCo/C) were used as benchmark of cathode catalyst. The ionomer to carbon ratio was 0.6 for c-Pt/C and c-PtCo/C, while 0.7 for CoO_x@Pt/C. The cathode catalyst loading was controlled to be about 0.09 mg_{PGM}/cm^2. The PGM loading on

anode/cathode were confirmed by the ICP-AES measurements. The fabricated CCM was dried under vacuum for an hour to evaporate the solvents. For the MEA fabrication, two gas diffusion layers (GDLs), two PTFE gaskets, and the prepared CCM were pressed together. The thickness of the PTFE gasket is 127 μm (5 mil). The thickness of GDL, which includes a microporous layer, is 175 μm (Freudenberg H14C7).

MEA Activity Tests

The MEA was loaded in Fuel Cell Technology 5 cm^2 or 25 cm^2 single-cell fixture and tested in the Scribner 850e fuel cell test stand. Firstly, MEA activation was conducted by holding the voltage at 0.5 V under H_2/Air flow of 100/100 standard cubic centimeters per minute (sccm) for 5 cm^2 cell and 500/500 sccm for 25 cm^2 cell at 80 °C, 100% relative humidity (RH), 150 kPa_{abs} (all pressure noted in this work refer to the absolute pressure) until the current reached plateau (usually about 30 minutes). Then, the MEA was further activated at oversaturated conditions, where the fuel temperate was set at 80 °C for both cathode and anode before entering the cell (hold at 60 °C). The mass activity (MA) tests were at 80 °C, 100% RH, 150 kPa_{abs} with a flow rate of 835 (H_2)/2000 (O_2) sccm.

The rated power at BOL and EOL was tested in Scribner 850e fuel cell fixture under 94 °C, 250 $kPa_{abs,}$ and 100% RH.[44] The H_2/Air gas flow rate was 126/400 sccm for 5 cm^2 cell and 630/2000 sccm for 25 cm^2 cell, which is equivalent to the stoichiometry of 1.5/2.0 at 2.4 A/cm^2 (endpoint of current density plot). The DOE has set a heat-rejection limit of $Q/\Delta T_i$ <1.45 for light-duty vehicles, assuming 90 kW stack gross power (P_{stack}) required for 80 kW net power and ambient temperature of 40 °C as the baseline. Power density at rated voltage (V_{rated}) is defined as the rated power, which is the maximum power aligned with heat management capability. The rated voltage is defined by the following equation 1 (Eq. 1)[44].

$$\frac{Q}{\Delta T_i} = \frac{P_{stack}(1.25 - V_{rated})}{V_{rated}(T_{stack} - T_{ambient})} \quad \text{Eq. 1}$$

The DOE protocol assumes P_{stack} = 90 kW and $T_{ambient}$ =40 °C, if T_{stack} =94 °C, Q/ ΔT_i =1.445, which meets the target (Q/ΔT_i of ≤1.45), the V_{rated} will be around 0.67 V. Thus, the rated power will be measured at 0.67 V.[44]

All of the MEA's BOL and EOL performance metrics, such as MA, ECSA, and H_2 crossover, were recorded by the Scribner 850e fuel cell test station and the Scribner 885 potentiostat. The ECSA was determined by integrating the CO stripping peak, assuming 420 μC/cm^2_{Pt}. The CO stripping test in MEA followed the protocol in the literature.[45]

MEA ADT tests

For the accelerated degradation test (ADT), we adopted the more aggressive 30,000-cycle square wave protocol with each cycle holding the MEA at the voltage of 0.6 V for 3 seconds and then 0.95 V for 3 seconds. The full ADT is carried at 80 °C, ambient pressure, 100% RH with H_2/N_2 flow 100/100 sccm for anode and cathode, respectively. We noted that our ADT protocol strictly followed the DOE protocol for PGM-based catalysts.[1, 46]

Computational Studies

Density-Functional Global Optimizations (DF-GO) simulations were performed employing the Basin Hopping (BH) algorithm [47-48] as implemented in an in-house python code. In each BH step, starting from a given locally relaxed initial structure, defined by 3N atomic coordinates (where N is the number of atoms in the cluster), the GO algorithm generates a new configuration via a random perturbation of the coordinates which is then subjected to a local geometry optimization, after which the new configuration is accepted or rejected according to a Metropolis criterion, i.e., with probability min(1,exp(ΔE/T), where ΔE is the energy difference between the initial and the new locally relaxed configurations and T is a fictitious temperature (in our

simulations varying between 3500 and 5000 K). The procedure starts from a sample of 3N arbitrary or selected atomic coordinates and iteratively continues with the random generation of new local minima starting from the currently accepted one, eventually providing a putative Global Minimum (GM) as the lowest-energy configuration. All the local minima, which belong to a DFT-PBE [49] Potential Energy Hyper-Surface (PES), were generated employing the OPENMX code[50], which solves the Kohn-Sham equations within the pseudopotential-LCAO framework by using localized pseudo-atomic numerical basis sets[51], whereas the Hartree potential is evaluated with the aid of a fast FFT solver, which relies on the use of a plane-wave basis set whose size depends on a chosen cut-off energy[52]. In our simulations, the Kohn-Sham energies were evaluated by feeding OPENMX with 'Quick'-type basis sets, norm-conserving pseudopotentials, and an energy cutoff of 150 Ry [53].

The energy sequence as a function of the BH iterations for two typical GO runs: a DF-GO run on the Pt_{79} cluster starting from the Pt_{79} truncated octahedron as the initial configuration, and the random sampling of the oxygen binding sites on the $Pt_{77}CoO_6$ GM cluster. In the latter case, oxygen binding sites were singled out by employing a Voronoi tessellation procedure[54]. All the tools needed for the analysis of the results of the simulation are encoded in the authors' proprietary python software.

Starting from the OPENMX DF-GO database, a more accurate approach was used to predict energies and atomic equilibrium configurations by local geometry relaxation of candidate low-energy GO structures using the plane-wave Quantum Espresso (QE) code[55]. All the energies reported in the main text refer to the QE approach. The QE calculations were conducted spin unrestricted at the DFT/PBE level augmented with both Grimme-D3 dispersion and Hubbard-U corrections (U=3.5 eV for Co and U=0.0 for the other atomic species). We employed a cut-off

energy of 40 Ry for describing the wave functions, a cut-off energy of 200 Ry for describing the electron density, and GBRV ultra-soft pseudopotentials[56]. Work functions were evaluated according to the procedure proposed in Refs.[57-58]. Transmission Electron Microscopy (TEM) images were simulated using the QSTEM code.[59]

4.3 Results and discussion

Structural and compositional characterizations

The scanning transmission electron microscopy (STEM) and high-resolution transmission electron microscopy (HRTEM) images reveal that the resulted CoO_x@Pt/C product (Figure 4.2a, Figure 4.3a) are uniformly dispersed on the carbon support with average diameters of 1.5 ± 0.2 nm (Figure 4.2a inset). Powder X-ray diffraction (XRD) studies show a similar XRD pattern to that of the commercial Pt (c-Pt/C) and commercial PtCo (c-PtCo/C) catalysts with a face-centered cubic (fcc) structure (Figure 4.3b). We see a notably broader peak in the XRD pattern, based on which we can estimate an average size of 1.5 nm, consistent with microscopic size analysis (Figure 4.3c).

The composition analysis via inductively coupled plasma atomic emission spectroscopy (ICP-AES) shows that the CoO_x@Pt/C has a Co:Pt atomic ratio of 4.7:95.3. The energy dispersive X-ray spectroscopies (EDS) reveal a consistent Co:Pt ratio of 4.9:95.1, and the spatially resolved EDS mapping shows that the Co content is sparsely dispersed inside the nanoparticle (Figure 4.2b). Interestingly, X-ray photoelectron spectroscopy (XPS) analysis of the CoO_x@Pt/C shows no Co 2p peak (Figure 4.2c), indicating an essentially pure metallic Pt shell. This is not surprising considering the acid washing process could remove most surface CoO_x species, and the remaining CoO_x is likely fully enclosed by the Pt shell and thus less sensitive to surface-sensitive XPS studies. Indeed, the Co 2p peak (consistent with Co^{2+}) emerged after removing the surface atomic layer by

in-situ Ar^+ etching (Figure 4.2c), confirming that the resulting material has a core-shell structure with the CoO_x clusters embedded in a Pt shell.

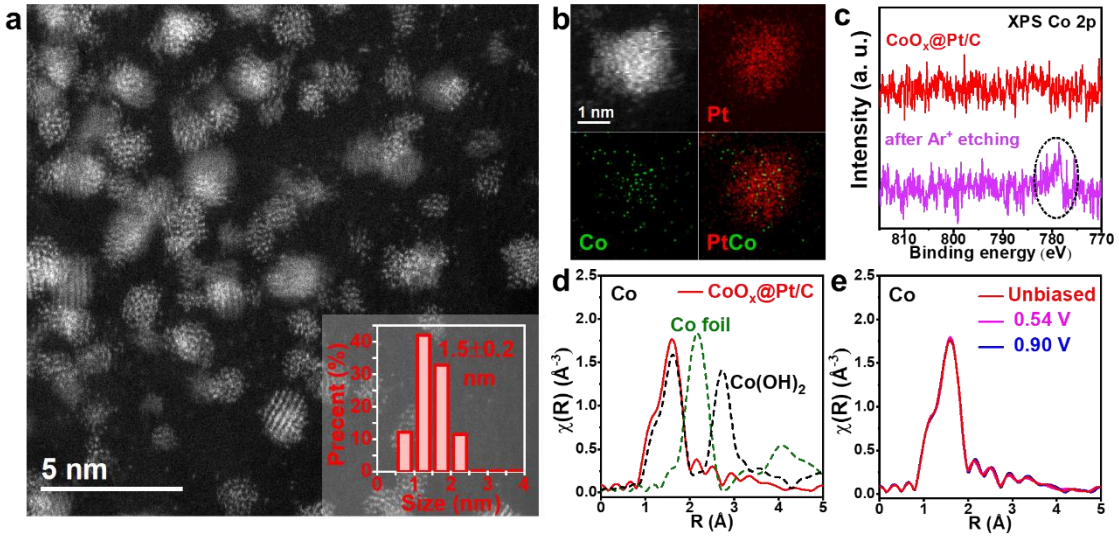

Figure 4. 2. Synthesis and structural characterization of CoO_x@Pt supported on carbon. (a) HAADF STEM images of the CoO_x@Pt/C nanocatalyst. Inset: corresponding size distributions and the averaged size measured in particle diameter. (b) HAADF STEM image and corresponding EDS elemental maps with red representing Pt and green representing Co. (c) XPS depth profiling with spectra of Co 2p for CoO_x@Pt/C before and after Ar^+ etching. *In situ* Fourier transform EXAFS of CoO_x@Pt/C collected at Co edge: (d) unbiased spectrum (red solid line) compared with Co foil (green dot line) and $Co(OH)_2$ (black dot line) references; and (e) potential dependent spectra compared with unbiased one, showing unchanged signals under varied applied potentials.

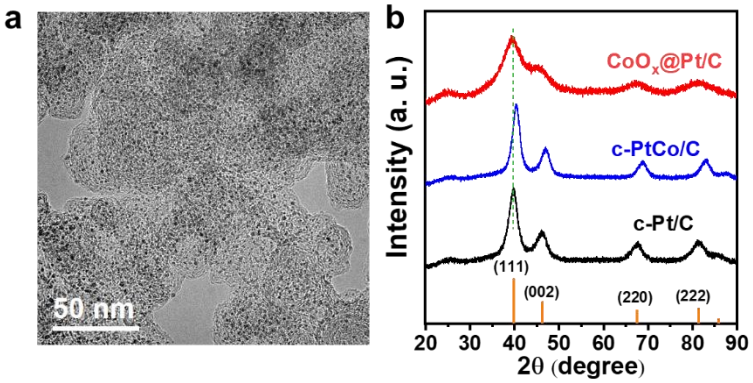

c

Catalyst	XRD	
	FWHM	Size
c-Pt/C	2.36°	3.68 nm
c-PtCo/C	1.94°	4.51 nm
CoO_x@Pt/C	5.65°	1.51 nm

Figure 4. 3. TEM and XRD characterizations. (a) TEM image of the CoOx@Pt/C catalyst. (b) XRD patterns and (c) the averaged XRD size of CoOx@Pt, and benchmarking commercial c-Pt/C, c-PtCo catalysts. They were calculated from the full width at half maximum (FWHM) of the XRD peaks using the Scherrer equation.

We further conducted in-situ X-ray absorption spectroscopy (XAS) studies in 0.1 M $HClO_4$ aqueous solution to understand the local atomistic and electronic structures (Figure 4.2d and e,

Figure 4.4, Figure 4.5, Figure 4.6, Table 4.1). The Pt L_3-edge X-ray absorption near-edge structure (XANES) spectra show that the majority of Pt is in the metallic phase (Figure 4.4a). The extended X-ray absorption fine structure (EXAFS) fitting result gives a Pt-Pt bond length of 2.74 Å (Figure 4.4b, c, Extended Data Table 2), which is 1.4% smaller than that in bulk Pt (2.78 Å in Pt foil), suggesting the existence of compressive strain that is beneficial for ORR [7, 60]. The Co K-edge XANES result confirms the Co(II) oxidation state (Figure 4.5a). Importantly, the Co EXAFS and fitting results show a single Co-O peak with a coordination number of 6 ± 1, with no obvious Co-Co and Co-O-Co interactions (Figure 4.2d, Table 4.1), indicating atomically dispersed $Co(II)O_6$ clusters. Moreover, the Co K-edge is found to be independent of the applied potentials (Figure 4.2e, Figure 4.5b), suggesting the $Co(II)O_6$ clusters are well-protected inside the nanoparticles and do not directly interact with electrolytes. Meanwhile, the intensity of Pt-O interaction reduced with decreasing potential from 0.90 V to 0.54 V, which is consistent with the desorption of oxygenated species on Pt surface in this potential regime (Figure 4.6a, c). Interestingly, a clear Pt-O interaction remains at 0.54 V (Figure 4.6c, red arrow) where the electrode surface is presumably free of oxygenated adsorbates (Figure 4.6d red arrow, Table 4.1) [38]. Such remaining Pt-O interaction can be attributable to the interaction between Pt atoms and the embedded $Co(II)O_6$ species. These combined STEM-EDS, XPS, and in-situ XAS characterizations robustly demonstrate the formation of a unique design of ultrafine Pt nanocatalysts with embedded atomically dispersed $Co(II)O_6$ clusters well-protected by the Pt shell.

Pt L_3-edge EXAFS fitting						
Sample	Scattering path	CN	R (Å)	σ^2 (10^{-3} Å^2)	E_0 (eV)	R factor
CoO_x@Pt/C unbiased	Pt-Pt	6±1	2.74±0.01	7±1	7±1	0.01
	Pt-Co	0.8±0.7	2.61±0.03	8±8		
	Pt-O	0.4±0.3	2.02±0.03	4±7		
CoO_x@Pt	Pt-Pt	7±1	2.74±0.01	7±1	8±1	0.01

at 0.54 V	Pt-Co	0.3±0.4	2.61±0.03	2±7		
	Pt-O	0.4±0.2	2.00±0.03	0.3±3		
Commercial Pt/C at 0.54 V	Pt-Pt	9.2±0.7	2.755±0.003	5.9±0.6	7.8±0.5	0.006
	Pt-O	-	-	-		
Co K-edge EXAFS fitting						
Sample	Scattering path	CN	R (Å)	σ^2 (10^{-3} Å^2)	E_0 (eV)	R factor
CoO_x@Pt/C unbiased	Co-O	6±1	2.08±0.01	5±2	-2±1	0.010

Table 4. 1. Summaries of structural parameters extracted from *in-situ* EXAFS fitting of CoO_x@Pt at the Pt L_3-edge and Co K-edge and commercial Pt/C reference. CN is the coordination number; R is the interatomic distance (the bond length between Pt or Co central atoms and surrounding coordination atoms); σ^2 is the Debye-Waller factor (a measure of thermal and static disorder in absorber-scatterer distances); E_0 is edge-energy shift (the difference between the zero kinetic energy value of the sample and that of the theoretical model). R factor is used to value the goodness of the fitting.

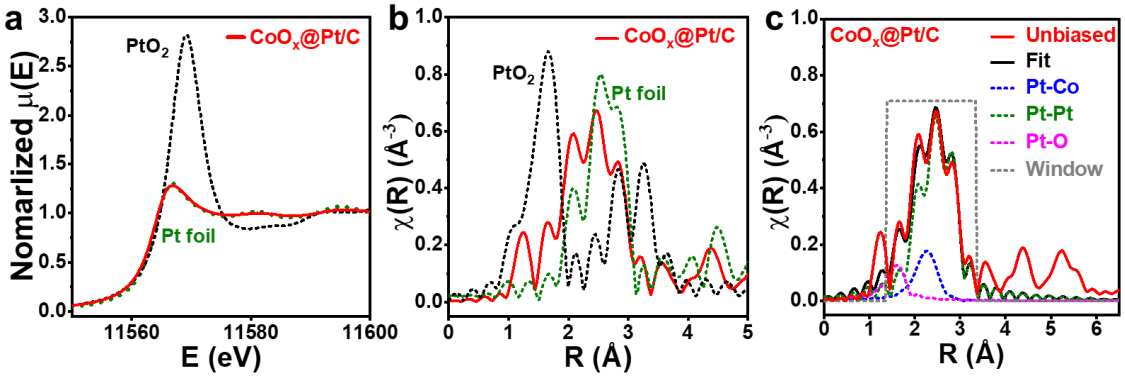

Figure 4. 4. The *in-situ* X-ray absorption (XAS) spectra of CoO_x@Pt/C at Pt L_3-edge without applied potential (Unbiased). (a) X-ray absorption near-edge structure (XANES) spectra, and (b) Fourier transform extended X-ray absorption fine structure (EXAFS) spectra with references noted as Pt foil (green dot line) and PtO_2 (black dot line). (c) Fitting of the Fourier transform EXAFS spectrum. The *in-situ* data were collected in 0.1 M $HClO_4$ electrolyte without applied potential (unbiased).

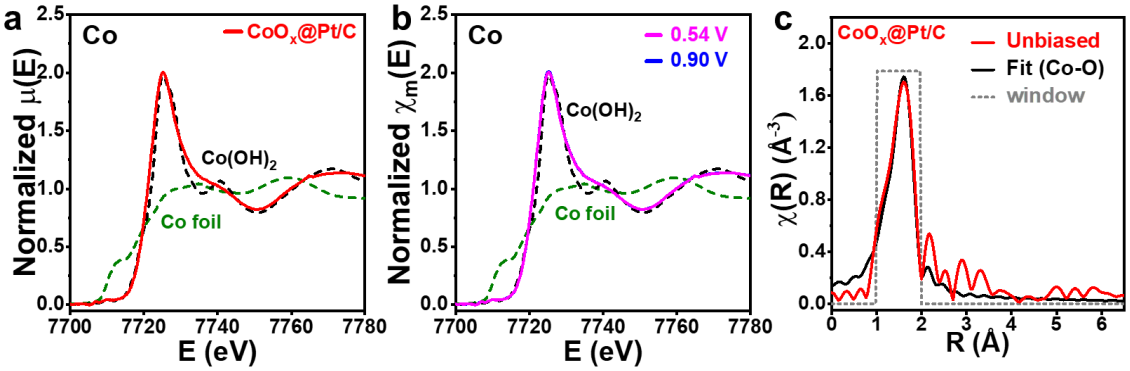

Figure 4. 5. The *in-situ* X-ray absorption (XAS) spectra of CoO_x@Pt/C at Co K-edge. XANES spectrum (a) without applied potential (unbiased), and (b) under 0.54 V and 0.90 V. (c) Fitting of the

unbiased Fourier transform EXAFS spectrum. The *in-situ* data were collected in 0.1 M $HClO_4$ electrolyte without applied potential (unbiased), at 0.54 V, and 0.90 V versus RHE.

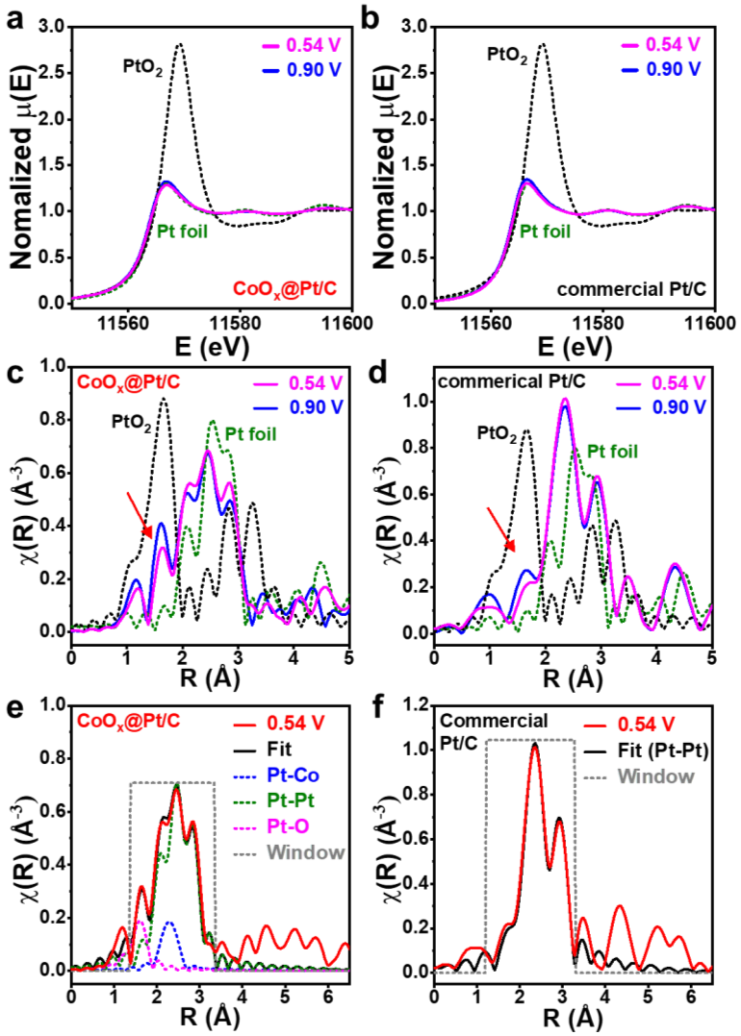

Figure 4. 6. The *in-situ* XAS spectra of CoO_x@Pt/C and reference commercial Pt/C at the Pt L_3-edge. *In-situ* XANES spectra at 0.54 V and 0.90 V of (a) CoO_x@Pt/C, and (b) commercial Pt/C. *In-situ* Fourier transform EXAFS spectra at 0.54 V and 0.90 V of (c) CoO_x@Pt/C, and (d) commercial Pt/C. Fitting of the Fourier transform EXAFS spectrum at 0.54 V of (e) CoO_x@Pt/C, and (f) commercial Pt/C; noted that no Pt-O interaction is observed at 0.54 V in the commercial Pt/C, which suggests that the existence of Pt-O interaction at 0.54 V in the CoO_x@Pt/C catalyst is from the interaction with the embedded CoO_x.

MEA Evaluation of Fuel Cell Performance

The practical fuel cell performance of the CoO_x@Pt/C was evaluated in a 5 cm^2 single-cell fuel cell fixture (Fig. 4.1a). The MEA was prepared by directly coating the catalyst ink on the proton exchange membrane using the ultrasonic spray at the cathode loading of 0.09 mg_{PGM}/cm^2

and anode loading of 0.01 mg_{PGM}/cm^2. The performance is benchmarked against commercial c-Pt/C and c-PtCo/C under identical conditions. Notably, the CoO_x@Pt/C exhibits an initial MA of 1.10 A/mg_{PGM} (Figure 4.7a), considerably higher than those of the c-Pt/C (0.34 A/mg_{PGM}), c-PtCo (0.57 A/mg_{PGM}) and DOE target (0.44 A/mg_{PGM}). Furthermore, the CoO_x@Pt/C retains 88.2% of its initial MA after the aggressive square wave ADT (Figure 4.7a), which is much higher than the 22.5% and 36.8% MA retentions observed in c-Pt/C and c-PtCo, respectively. It represents the state-of-the-art MA retention achieved in the demanding square wave ADT test.[61] Significantly, the end-of-life (EOL) MA (0.97 A/mg_{PGM}) is 3.7 times of the DOE target (0.264 A/mg_{PGM}), 4.6 times the c-PtCo/C catalyst (0.21 A/mg_{PGM}), and 13.1 times of the c-Pt/C catalysts (0.07 A/mg_{PGM}), and represents the highest EOL MA reported in MEA tests to date.[22-26, 36, 62-63]

It is important to note that the MA test, under pure oxygen, primarily assesses the intrinsic activity of catalysts without being affected by mass transport issues, while the rated power test under H_2-air test reflects the practical performance of the catalyst. The H_2-air fuel cell with CoO_x@Pt/C catalyst delivers a rated power of 1.04 W/cm^2, outperforming those with c-Pt/C (0.88 W/cm^2) and c-PtCo (0.92 W/cm^2) (Figure 4.7b), and exceeding the DOE 2020 target of 1.0 W/cm^2. In addition, a useful metric to evaluate the PGM utilization in fuel cells is to normalize the power by the total PGM loading (W/mg_{PGM}). In this regard, the CoO_x@Pt/C MEA delivers a high Pt utilization of 10.4 W/mg_{PGM} (Figure 4.7c), well above the DOE target (8.0 W/mg_{PGM}). Furthermore, the CoO_x@Pt/C demonstrated notably better performance than c-Pt/C or c-PtCo/C throughout the entire current density regime (Figure 4.7d, e). These power performances of the CoO_x@Pt/C are among the best reported performance for Pt-based catalysts. More importantly, the CoO_x@Pt/C exhibits a record high EOL rated power (Pt utilization) of 0.96 W/cm^2 (9.6

W/mg$_{PGM}$) (Figure 4.7b), far higher than those of c-Pt/C (0.32 W/cm^2, 3.2 W/mg$_{PGM}$) and c-PtCo (0.61 W/cm^2, 6.1 W/mg$_{PGM}$).

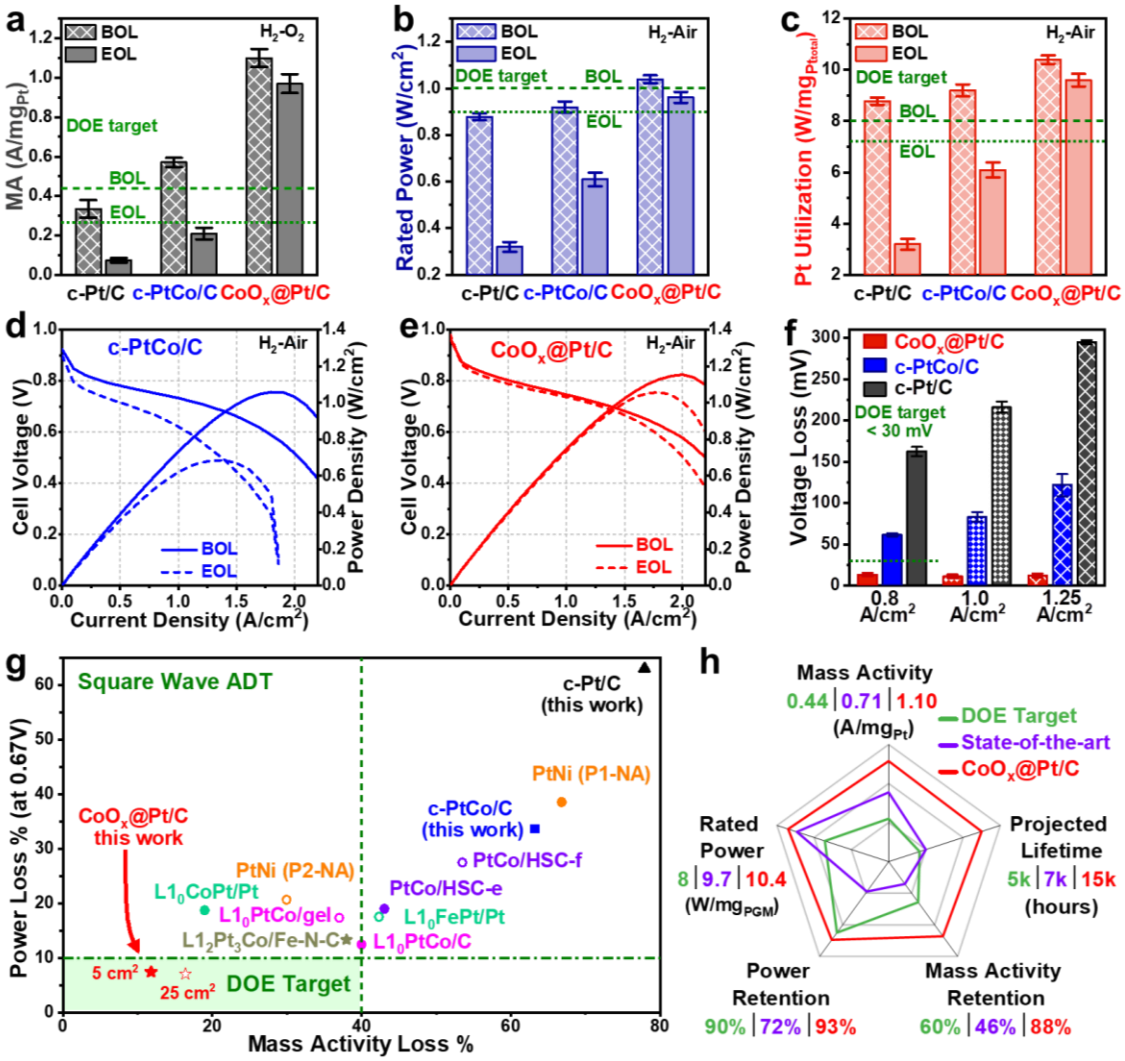

Figure 4. 7. MEA performance of CoO_x@Pt/C, commercial PtCo (c-PtCo/C), commercial Pt/C (c-Pt/C. (a) Comparison of mass activity (MA) obtained in H_2/O_2 tests at the beginning of life (BOL; before ADT) and end of life (EOL; after ADT). Comparison of (b) rated power density and (c) Pt utilization obtained in H_2/air tests at BOL and EOL. DOE targets are represented by green dash (BOL) and green dot (EOL) lines. (d, e) Polarization plots (left axis) and power density plots (right axis) of (d) c-PtCo/C and (e) CoO_x@Pt/C obtained in H_2/air tests at BOL and EOL, highlighting extraordinary power performance and stability of the MEA with CoO_x@Pt/C. (f) Voltage loss at current density of 0.8, 1.0 and 1.25 mA/cm^2. (g) The comparison of MA loss and power loss between CoO_x@Pt/C (data obtained from 5 cm^2 (solid star) and 25 cm^2 (hollow star) cell active area) and the state-of-the-art catalysts reported in the literature: PtCo/HSC-e, PtCo/HSC-f [23]; PtNi P1-NA, PtNi P2-NA [22]; $L1_0$PtCo/C, $L1_0$PtCo/gel [63]; $L1_0$CoPt/Pt, $L1_0$FePt/Pt [26]; $L1_2Pt_3$Co/Fe-N-C [24]. It highlights that CoO_x@Pt/C is the only catalyst that can meet both durability targets (light green square). The CoO_x@Pt/C represents the only catalyst simultaneously satisfying the MA loss and power loss target.

(h) The comparison of major fuel cell performance metrics among DOE target, the state-of-the-art catalyst (PtCo/HSC-e/f DOE selected as current status reference) [1, 23], and the CoO_x@Pt/C in this work.

The stability can be further evaluated by the voltage loss at a given current density (e.g., 0.8 A/cm^2). The DOE 2020 target suggested a voltage loss <30 mV at 0.8 A/cm^2. When comparing the BOL and EOL polarization curves, the CoO_x@Pt/C exhibits superior durability greatly outperforming the c-Pt/C or c-PtCo, with only 13.3 mV loss at 0.8 A/cm^2 (Figure 4.7f), which is substantially smaller than that of Pt/C (162.5 mV) or c-PtCo/C (61.3 mV). Moreover, there was only a slight drop throughout the entire curve after the ADT for CoO_x@Pt/C (Figure 4.7f), even in the more challenging HCD region (*e.g.*, 11.1 mV loss at 1.0 A/cm^2 and 12.0 mV loss at 1.25 A/cm^2), clearly highlighting the exceptional stability of the CoO_x@Pt/C catalysts. With the high MA retention of 88.2% and remarkably low rated power loss of 7.5%, the CoO_x@Pt/**C** nanocatalyst represents the first catalyst satisfying both MA and the more challenging power durability targets (light green area in Figure 4.7g). It is interesting to note that such a small voltage loss in the HCD region can be translated into an extraordinary projected lifetime of around 15,000 hours, which is three times of the DOE 2020 target (5,000 hours) for light-duty transportation applications.[1]

To the best of our knowledge, our catalyst represents the only catalyst with both BOL and EOL performance metrics simultaneously exceeding the DOE targets (Figure 4.7h).[17, 43-44] It should be highlighted that although a number of advanced catalyst designs have led to impressive BOL performance previously, the durability has been a persistent challenge and the EOL performance is generally far from satisfactory [43, 62]. In particular, there is no report of catalyst system that can deliver a rated power retention of 90 % and MA retention of 60% while satisfying all BOL performance metrics set in DOE targets.[1] As the fuel cells must meet performance

requirements throughout their service lifetime, the EOL instead of BOL performance ultimately determines the amount of Pt needed [5]. In this regard, the exceptional EOL performance achieved in our design is particularly important for enabling PEMFCs with substantially reduced lifetime-adjusted cost in practical applications.

Understanding of the exceptional durability

We have analyzed the nanocatalyst size distribution before and after the ADT in MEA (Figure 4.8a, b, Figure 4.9). Overall, the size of c-Pt/C increased dramatically from 3.5 ± 0.8 nm at BOL to 7.2 ± 3.6 nm at EOL (Figure 4.9a-d), and a similar size growth was also observed in c-PtCo/C (from 4.7 ± 1.4 nm at BOL to 8.1 ± 3.5 nm at EOL) (Figure 4.8b, Figure 4.9e-h). Such a substantial size increase can be attributed to (i) nanoparticle detachment, movement, and coalescence, and (ii) oxidative dissolution, diffusion, and Ostwald ripening process[18]. In contrast, the average size of the CoO_x@Pt/C only increased moderately from 1.5 ± 0.2 nm at BOL to 2.5 ± 1.2 nm at EOL (Figure 4.8a, Figure 4.9i-l). Similarly, the CoO_x@Pt catalyst exhibits a considerably higher EOL ECSA (35.9 ± 0.9 m^2/g_{PGM}) from CO stripping experiments at 80°C in MEAs than those of commercial Pt (8.9 ± 1.8 m^2/g_{PGM}) and PtCo alloy (12.3 ± 1.0 m^2/g_{PGM}) catalysts. These analyses clearly highlight the benefit of our design to effectively restrain the size growth and improve the overall durability. In particular, the embedded CoO_x strengthens the interactions with surface Pt atoms due to the strong metal-oxide interaction, greatly slowing down the oxidation and dissolution of surface Pt atoms and retarding the Ostwald ripening process (Figure 4.1b). This stabilization effect is supported by the simulation results to be discussed later.

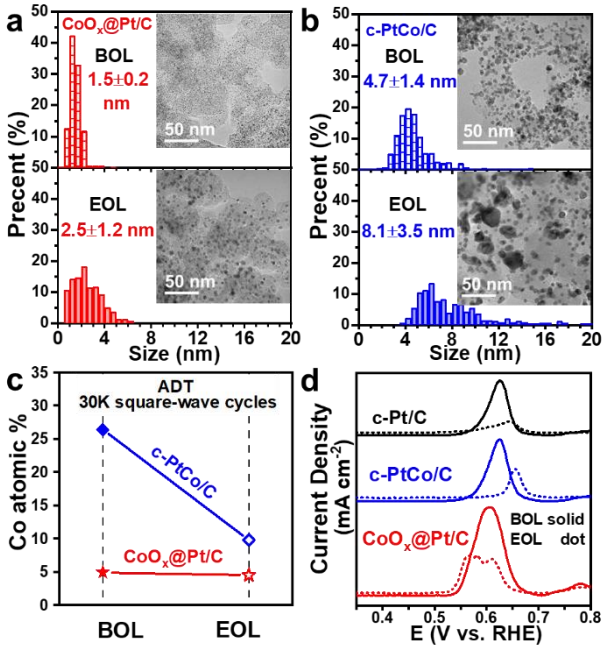

Figure 4. 8. Size, composition, and CO stripping analyses of catalysts at BOL and EOL. Histogram of particle size distribution at BOL and EOL (a) CoO_x@Pt/C and (b) c-PtCo/C catalysts. The inset shows the corresponding TEM images. (c) The change of Co atomic composition based at BOL and EOL. (d) Comparison of CO stripping experiments at 80°C in MEAs, showing the change of oxidation peaks at BOL (solid lines) and EOL (dotted lines) of the commercial and CoO_x@Pt/C catalysts.

In addition to size analyses, the EDS composition analyses also confirm that the Co content of CoO_x@Pt nanoparticles was well retained during the ADT with a minor decrease from 4.9 at.% at BOL to 4.5 at.% at EOL (Figure 4.8c), with the Co content remaining sparsely embedded inside the nanoparticle (Figure 4.10). In contrast, there was a drastic composition change from 26.4 at.% to 9.8 at.% in the c-PtCo nanoparticles (Figure 4.8c), indicating substantial leaching of Co cations that may cause considerable loss in intrinsic activity and cation poisoning effects on the mass transport and overall device performance [19-20].

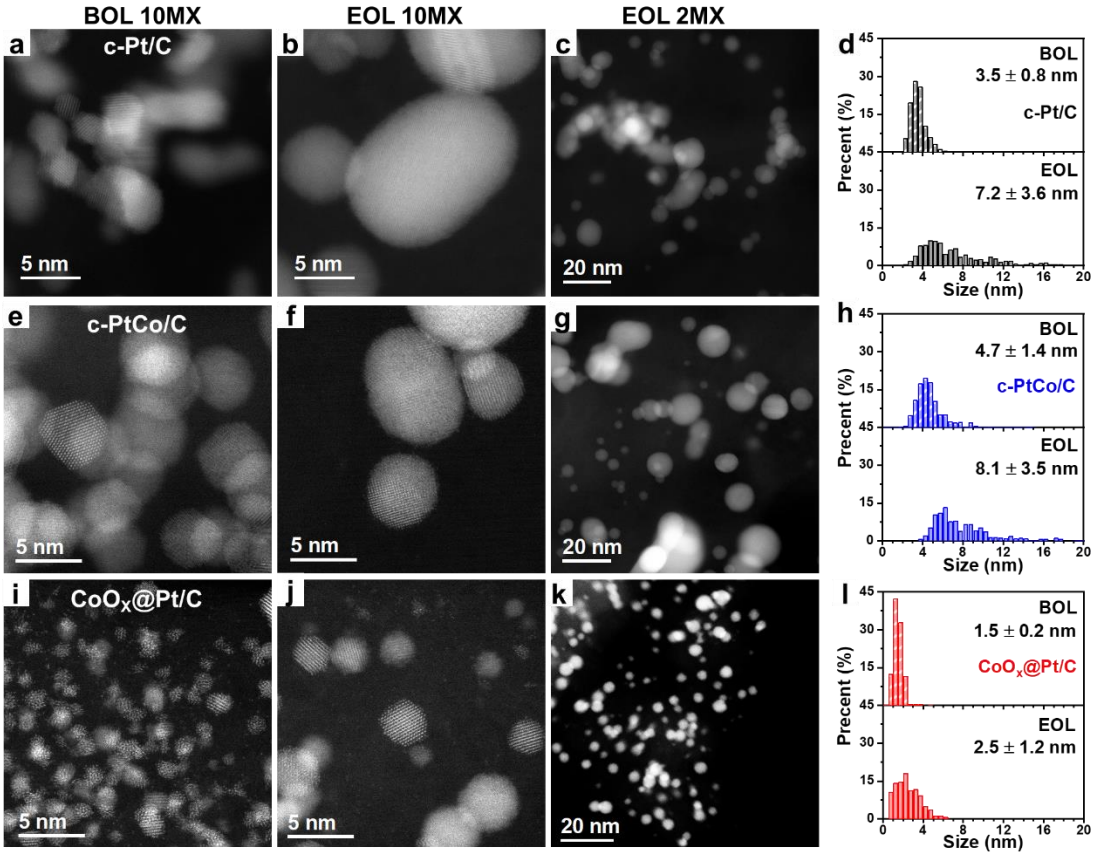

Figure 4. 9. STEM images and size distribution at both BOL and EOL. (a-d) c-Pt/C. (e-h) c-PtCo/C. (i-l) CoO_x@Pt/C.

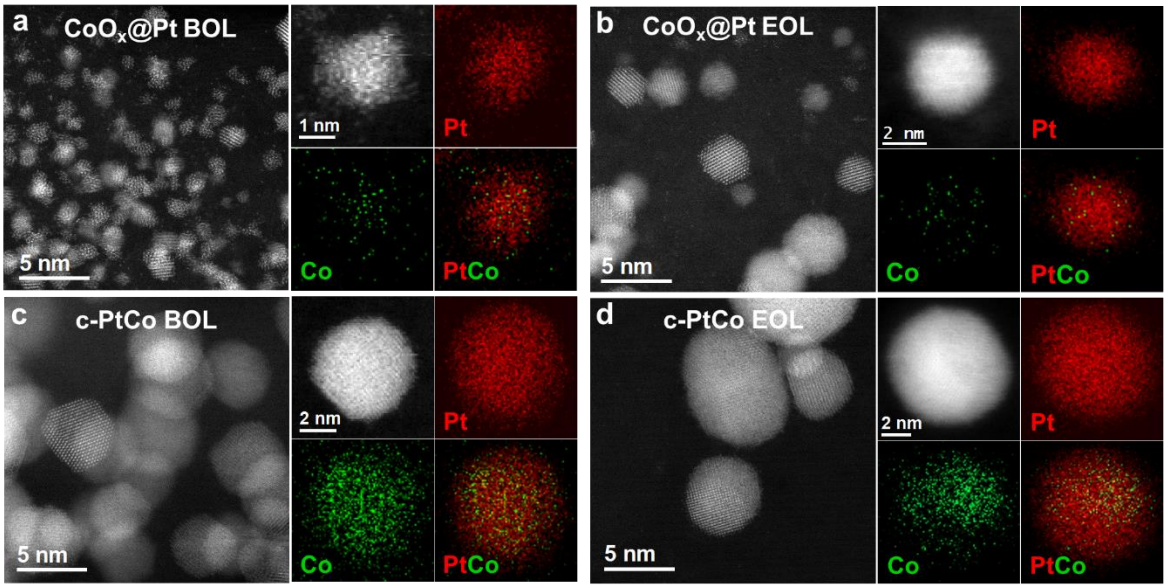

Figure 4. 10. Characterization of catalysts at BOL and EOL, HAADF STEM, and corresponding EDS elemental mappings of (a-b) CoO_x@Pt/C. (c-d) c-PtCo/C.

Moreover, CO stripping experiments were also used to probe the change in the chemisorption behavior of different catalysts. Previous studies have shown that the lower the peak potential of CO oxidation, the weaker the CO binding strength, which indicates a lower Pt *d*-band center and weaker oxygen adsorption energy favorable for ORR kinetics [64]. Interestingly, after the ADT, both c-Pt/C and c-PtCo/C show a notable shift to higher binding energy, while such a shift is not observed in the CoO_x@Pt/C (Figure 4.8d), indicating the retainment of the favorable weak oxygen adsorption characteristics for excellent EOL performance.

Theoretical Analysis

To further understand the fundamental origin of their exceptional stability, we computationally predicted the atomistic configurations, energetics, and electronic structure of the ultrafine Pt nanoparticles with endohedral CoO_x clusters to compare their thermodynamic and kinetic stability with pure Pt and PtCo alloy nanoparticles. We focused on the size large enough to accommodate a single CoO_x unit (typically, CoO_6, see below) with a complete shell of Pt atoms, around 80 atoms. Our calculations indicated that the preferred stoichiometry of the CoO_x unit was CoO_6 (Figure 4.11), in agreement with experimental EXAFS studies.

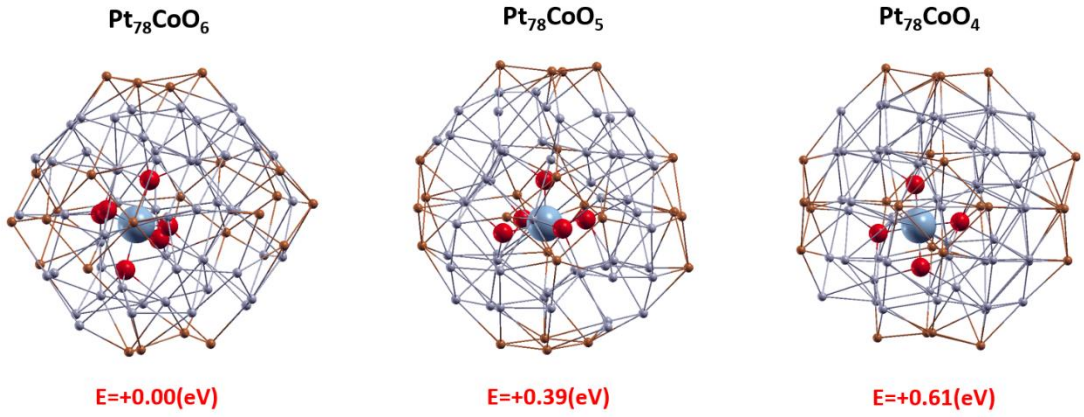

Figure 4. 11. Energetics of initial structures of $Pt_{78}CoO_x$ clusters generated from the TO configuration with different oxygen content (x). Note the increase in energy when reducing the oxygen content of the $Pt_{79}CoO_6$ cluster (whose initial configuration was obtained encapsulating an octahedral CoO_6 unit inside a Pt_{79} Truncated Octahedron structure). Note that the encapsulation of CoO_x inside the host

Pt structure strongly deforms the initial TO shape where Pt atoms belonging to 100 facets (reddish brown color in the figure) and 111 facets can hardly be singled out.

No rigorous information exists in the literature on the atomistic configurations of Pt-based nanoparticles in this size regime, not even pure Pt, which must be predicted *ab initio*. We therefore performed extensive Density-Functional Global Optimization (DF-GO) [47] on nanoparticles with different atom numbers and stoichiometry, to determine their Global Minimum (GM) configurations, the corresponding energetics, electronic structure, and interaction with oxygen adatoms (see Methods). Interestingly, our DF-GO studies reveal that the most stable structure in this size range (e.g., Pt_{78}, $Pt_{77}Co$, and $Pt_{77}CoO_6$) typically exhibit a barrel-like structural motif (Figure 4.12a, b), which is energetically more stable by several eV with respect to other motifs, such as the truncated octahedron Pt_{79} with a closed-shell crystalline-like Wulff shape. Moreover, the Lowdin analysis reveals a positive charge of +0.45 on Co atoms, which compares well with the Lowdin charge of +0.39 for Co in bulk CoO, consistent with Co^{2+} status observed in XAS studies (Figure 4.5). We also note that the predicted oxygen and platinum coordination numbers of Pt (evaluated with a cut-off distance of 3.00 Å) are 0.21 and 6.23, in agreement with the experimental values of 0.4 ±0.3 and 6 ± 1, respectively (Table 4.1).

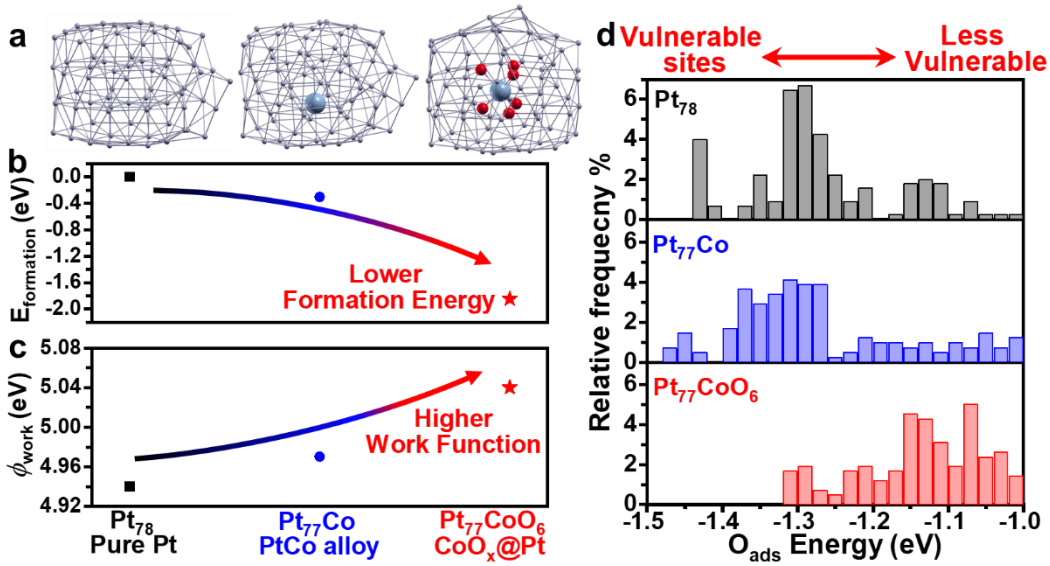

Figure 4. 12. Energetics of initial structures of $Pt_{78}CoO_x$ clusters generated from the TO configuration with different oxygen content (x). Note the increase in energy when reducing the oxygen content of the $Pt_{79}CoO_6$ cluster (whose initial configuration was obtained encapsulating an octahedral CoO_6 unit inside a Pt_{79} Truncated Octahedron structure). Note that the encapsulation of CoO_x inside the host Pt structure strongly deforms the initial TO shape where Pt atoms belonging to 100 facets (reddish brown color in the figure) and 111 facets can hardly be singled out.

More importantly, our calculation shows that the free energy of the Pt nanoparticle with endohedral CoO_6 ($Pt_{77}CoO_6$) is 1.85 and 1.55 eV lower than that of pure Pt (Pt_{78}) and PtCo alloy ($Pt_{77}Co$) structures with a similar size (Figure 4.12b), respectively. We have further calculated the work function of these structures and found the order: Pt_{78} (4.94 eV) < $Pt_{77}Co$ (4.97 eV) < $Pt_{77}CoO_6$ (5.04 eV) (Figure 4.12c), which correlates well with the experimentally observed order of stability under bias (Figure 4.7). Indeed, the nanocatalysts need to adjust their work function via oxygen adsorption and/or adding positive charge so that their work function equalizes with the target electrode potential under operating conditions (e.g., 0.90-0.95 V) [65]. A larger work function implies a lower positive charge density and makes the cluster less liable to oxidation, which contributes to improved stability against oxidative dissolution.

Next, we further explored the relative kinetic stability of these clusters under ORR conditions. Previous studies have revealed that the Pt dissolution during fuel cell operation mainly goes through an oxidative/reductive dissolution mechanism [3]. Therefore, we have calculated the oxygen adsorption energies on the surface sites of Pt_{78}, $Pt_{77}Co$, and $Pt_{77}CoO_6$ nanocatalysts to probe the kinetics of Pt dissolution. It is interesting to note that both Pt_{78} and $Pt_{77}Co$ alloy have a considerably higher population of surface sites with stronger oxidation adsorption energy (Figure 4.12c, black and blue), which are considered to be more vulnerable sites, i.e., more prone to oxidation and oxidative dissolution [31, 66-67]. In contrast, the surface Pt sites on $Pt_{77}CoO_6$ generally show weaker oxygen adsorption energy and thus have a higher kinetic barrier for oxidative dissolution (Figure 4.12c, red). Overall, these calculations explain the exceptional stability of the

CoO_x@Pt/C against oxidative dissolution of surface Pt atoms and Oswald ripening process, which further prevents the embedded CoO_x from leaching out, as observed in experiment (Figure 4.8c).

4.4 Conclusion

Overall, by embedding near atomically dispersed CoO_x clusters inside ultrafine Pt nanoparticles to induce strong metal-oxide interaction against both size and composition degradation, we have created a unique design of ultrafine CoO_x@Pt/C nanocatalysts. Both experiments and simulations corroborate the existence of a set of CoO_x-endohedral-doped Pt nanoparticles with unique thermodynamic stability and reduced tendency to oxidative dissolution. This CoO_x@Pt/C nanocatalysts show remarkable fuel cell performance, delivering a high MA of 1.10 A/g_{PGM}, a high power-density of 1.04 W/cm^2 at a low total PGM loading of 0.1 mg_{Pt}/cm^2, an unprecedentedly MA retention of 88.2%, and power retention of 92.5% after the aggressive 30,000 cycles of square wave ADT, all exceeding the current state-of-the-art catalysts and the relevant DOE targets for the first time. The remarkable power retention performance projects a record-breaking fuel cell lifetime of 15,000 hours. Lastly, we should note that the atomically dispersed CoO_x species embedded in the Pt nanoparticle are conceptually distinct from conventional oxide supported catalysts. Our design takes advantage of the strong metal-oxide interaction while avoiding the common drawbacks of the oxide as a support, such as oxide dissolution and low conductivity. Considering fuel cell system cost and lifetime represent the two major roadblocks, our study presents a major leap in fuel cell catalyst development and holds significant potential for improving the commercial viability of PEMFCs, particularly for heavy-duty applications.

4.5 References

1. *Fuel Cell Technologies Office Multi-Year Research, Development, and Demonstration Plan*; U.S. Department of Energy, 2017.

2. Lohse-Busch, H.; Stutenberg, K.; Duoba, M.; Liu, X.; Elgowainy, A.; Wang, M.; Wallner, T.; Richard, B.; Christenson, M., Automotive Fuel Cell Stack and System Efficiency and Fuel Consumption Based on Vehicle Testing on a Chassis Dynamometer at Minus 18 °C to Positive 35 °C Temperatures. *International Journal of Hydrogen Energy* 2020, **45**, 861-872 doi:https://doi.org/10.1016/j.ijhydene.2019.10.150

3. Kodama, K.; Nagai, T.; Kuwaki, A.; Jinnouchi, R.; Morimoto, Y., Challenges in Applying Highly Active Pt-Based Nanostructured Catalysts for Oxygen Reduction Reactions to Fuel Cell Vehicles. *Nature Nanotechnology* 2021, **16**, 140-147 doi:10.1038/s41565-020-00824-w

4. *Average Annual Vehicle Miles Traveled by Major Vehicle Category*; EERE Alternative Fuels Data Center: https://afdc.energy.gov/data/, 2020.

5. Cullen, D. A.; Neyerlin, K. C.; Ahluwalia, R. K.; Mukundan, R.; More, K. L.; Borup, R. L.; Weber, A. Z.; Myers, D. J.; Kusoglu, A., New Roads and Challenges for Fuel Cells in Heavy-Duty Transportation. *Nature Energy* 2021, **6**, 462-474 doi:10.1038/s41560-021-00775-z

6. Li, M.; Zhao, Z.; Cheng, T.; Fortunelli, A.; Chen, C.-Y.; Yu, R.; Zhang, Q.; Gu, L.; Merinov, B. V.; Lin, Z.; Zhu, E.; Yu, T.; Jia, Q.; Guo, J.; Zhang, L.; Goddard, W. A.; Huang, Y.; Duan, X., Ultrafine Jagged Platinum Nanowires Enable Ultrahigh Mass Activity for the Oxygen Reduction Reaction. *Science* 2016, **354**, 1414-1419 doi:10.1126/science.aaf9050

7. Escudero-Escribano, M.; Malacrida, P.; Hansen, M. H.; Vej-Hansen, U. G.; Velázquez-Palenzuela, A.; Tripkovic, V.; Schiøtz, J.; Rossmeisl, J.; Stephens, I. E. L.; Chorkendorff, I., Tuning the Activity of Pt Alloy Electrocatalysts by Means of the Lanthanide Contraction. *Science* 2016, **352**, 73-76 doi:10.1126/science.aad8892

8. Chen, C.; Kang, Y.; Huo, Z.; Zhu, Z.; Huang, W.; Xin, H. L.; Snyder, J. D.; Li, D.; Herron, J. A.; Mavrikakis, M.; Chi, M.; More, K. L.; Li, Y.; Markovic, N. M.; Somorjai, G. A.; Yang, P.;

Stamenkovic, V. R., Highly Crystalline Multimetallic Nanoframes with Three-Dimensional Electrocatalytic Surfaces. *Science* 2014, **343**, 1339-1343 doi:10.1126/science.1249061

9. Zhang, L.; Roling, L. T.; Wang, X.; Vara, M.; Chi, M.; Liu, J.; Choi, S.-I.; Park, J.; Herron, J. A.; Xie, Z.; Mavrikakis, M.; Xia, Y., Platinum-Based Nanocages with Subnanometer-Thick Walls and Well-Defined, Controllable Facets. *Science* 2015, **349**, 412-416 doi:10.1126/science.aab0801

10. Seh, Z. W.; Kibsgaard, J.; Dickens, C. F.; Chorkendorff, I.; Nørskov, J. K.; Jaramillo, T. F., Combining Theory and Experiment in Electrocatalysis: Insights into Materials Design. *Science* 2017, **355**, eaad4998 doi:10.1126/science.aad4998

11. Li, W.; Chen, Z.; Xu, L.; Yan, Y., A Solution-Phase Synthesis Method to Highly Active Pt-Co/C Electrocatalysts for Proton Exchange Membrane Fuel Cell. *Journal of Power Sources* 2010, **195**, 2534-2540 doi:https://doi.org/10.1016/j.jpowsour.2009.11.035

12. Wang, X. X.; Hwang, S.; Pan, Y.-T.; Chen, K.; He, Y.; Karakalos, S.; Zhang, H.; Spendelow, J. S.; Su, D.; Wu, G., Ordered Pt3co Intermetallic Nanoparticles Derived from Metal–Organic Frameworks for Oxygen Reduction. *Nano Letters* 2018, **18**, 4163-4171 doi:10.1021/acs.nanolett.8b00978

13. Huang, L.; Zheng, C. Y.; Shen, B.; Mirkin, C. A., High-Index-Facet Metal-Alloy Nanoparticles as Fuel Cell Electrocatalysts. *Advanced Materials* 2020, **32**, 2002849 doi:https://doi.org/10.1002/adma.202002849

14. Ge, Y.; Wang, X.; Huang, B.; Huang, Z.; Chen, B.; Ling, C.; Liu, J.; Liu, G.; Zhang, J.; Wang, G.; Chen, Y.; Li, L.; Liao, L.; Wang, L.; Yun, Q.; Lai, Z.; Lu, S.; Luo, Q.; Wang, J.; Zheng, Z.; Zhang, H., Seeded Synthesis of Unconventional 2h-Phase Pd Alloy Nanomaterials for Highly

Efficient Oxygen Reduction. *Journal of the American Chemical Society* 2021, **143**, 17292-17299 doi:10.1021/jacs.1c08973

15. Liu, H.; Zhong, P.; Liu, K.; Han, L.; Zheng, H.; Yin, Y.; Gao, C., Synthesis of Ultrathin Platinum Nanoplates for Enhanced Oxygen Reduction Activity. *Chemical Science* 2018, **9**, 398-404 doi:10.1039/C7SC02997G

16. Liu, Z.; Zhao, Z.; Peng, B.; Duan, X.; Huang, Y., Beyond Extended Surfaces: Understanding the Oxygen Reduction Reaction on Nanocatalysts. *Journal of the American Chemical Society* 2020, **142**, 17812-17827 doi:10.1021/jacs.0c07696

17. Zhao, Z.; Chen, C.; Liu, Z.; Huang, J.; Wu, M.; Liu, H.; Li, Y.; Huang, Y., Pt-Based Nanocrystal for Electrocatalytic Oxygen Reduction. *Advanced Materials* 2019, **31**, 1808115 doi:10.1002/adma.201808115

18. Borup, R. L.; Kusoglu, A.; Neyerlin, K. C.; Mukundan, R.; Ahluwalia, R. K.; Cullen, D. A.; More, K. L.; Weber, A. Z.; Myers, D. J., Recent Developments in Catalyst-Related Pem Fuel Cell Durability. *Current Opinion in Electrochemistry* 2020, **21**, 192-200 doi:https://doi.org/10.1016/j.coelec.2020.02.007

19. Braaten, J. P.; Xu, X.; Cai, Y.; Kongkanand, A.; Litster, S., Contaminant Cation Effect on Oxygen Transport through the Ionomers of Polymer Electrolyte Membrane Fuel Cells. *Journal of The Electrochemical Society* 2019, **166**, F1337-F1343 doi:10.1149/2.0671916jes

20. Dumont, J. H.; Baker, A. M.; Maurya, S.; Kim, Y. S.; Mukundan, R.; Myers, D. J.; Borup, R. L., Effect of Cerium, Cobalt and Nickel Contaminants on the Oxygen Reduction Reaction at Platinum Electrodes. *ECS Transactions* 2017, **80**, 861-867 doi:10.1149/08008.0861ecst

21. Cai, Y.; Kongkanand, A.; Gu, W.; Moylan, T. E., Effects of Cobalt Cation on Low Pt-Loaded Pem Fuel Cell Performance. *ECS Transactions* 2015, **69**, 1047-1061 doi:10.1149/06917.1047ecst

22. Han, B.; Carlton, C. E.; Kongkanand, A.; Kukreja, R. S.; Theobald, B. R.; Gan, L.; O'Malley, R.; Strasser, P.; Wagner, F. T.; Shao-Horn, Y., Record Activity and Stability of Dealloyed Bimetallic Catalysts for Proton Exchange Membrane Fuel Cells. *Energy & Environmental Science* 2015, **8**, 258-266 doi:10.1039/C4EE02144D

23. Ko, M.; Padgett, E.; Yarlagadda, V.; Kongkanand, A.; Muller, D. A., Revealing the Nanostructure of Mesoporous Fuel Cell Catalyst Supports for Durable, High-Power Performance. *Journal of The Electrochemical Society* 2021, **168**, 024512 doi:10.1149/1945-7111/abe28e

24. Qiao, Z.; Wang, C.; Li, C.; Zeng, Y.; Hwang, S.; Li, B.; Karakalos, S.; Park, J.; Kropf, A. J.; Wegener, E. C.; Gong, Q.; Xu, H.; Wang, G.; Myers, D. J.; Xie, J.; Spendelow, J. S.; Wu, G., Atomically Dispersed Single Iron Sites for Promoting Pt and Pt3co Fuel Cell Catalysts: Performance and Durability Improvements. *Energy & Environmental Science* 2021, **14**, 4948-4960 doi:10.1039/D1EE01675J

25. Duan, X.; Cao, F.; Ding, R.; Li, X.; Li, Q.; Aisha, R.; Zhang, S.; Hua, K.; Rui, Z.; Wu, Y.; Li, J.; Li, A.; Liu, J., Cobalt-Doping Stabilized Active and Durable Sub-2 nm Pt Nanoclusters for Low-Pt-Loading Pemfc Cathode. *Advanced Energy Materials* 2022, **12**, 2103144 doi:https://doi.org/10.1002/aenm.202103144

26. Li, J.; Sharma, S.; Liu, X.; Pan, Y.-T.; Spendelow, J. S.; Chi, M.; Jia, Y.; Zhang, P.; Cullen, D. A.; Xi, Z.; Lin, H.; Yin, Z.; Shen, B.; Muzzio, M.; Yu, C.; Kim, Y. S.; Peterson, A. A.; More, K. L.; Zhu, H.; Sun, S., Hard-Magnet L10-Copt Nanoparticles Advance Fuel Cell Catalysis. *Joule* 2019, **3**, 124-135 doi:https://doi.org/10.1016/j.joule.2018.09.016

27. Yang, C.-L.; Wang, L.-N.; Yin, P.; Liu, J.; Chen, M.-X.; Yan, Q.-Q.; Wang, Z.-S.; Xu, S.-L.; Chu, S.-Q.; Cui, C.; Ju, H.; Zhu, J.; Lin, Y.; Shui, J.; Liang, H.-W., Sulfur-Anchoring Synthesis of Platinum Intermetallic Nanoparticle Catalysts for Fuel Cells. *Science* 2021, **374**, 459-464 doi:10.1126/science.abj9980

28. Qiu, H. J.; Gao, J. J.; Wen, Y. R.; Shang, B.; Wang, J. Q.; Lin, X.; Wang, Y., Platinum Cluster/Nanoparticle on Coo Nanosheets with Coupled Atomic Structure and High Electrocatalytic Durability. *ACS Applied Energy Materials* 2018, **1**, 1840-1845 doi:10.1021/acsaem.8b00263

29. Xu, S.; Wang, Z.; Dull, S.; Liu, Y.; Lee, D. U.; Lezama Pacheco, J. S.; Orazov, M.; Vullum, P. E.; Dadlani, A. L.; Vinogradova, O.; Schindler, P.; Tam, Q.; Schladt, T. D.; Mueller, J. E.; Kirsch, S.; Huebner, G.; Higgins, D.; Torgersen, J.; Viswanathan, V.; Jaramillo, T. F.; Prinz, F. B., Direct Integration of Strained-Pt Catalysts into Proton-Exchange-Membrane Fuel Cells with Atomic Layer Deposition. *Advanced Materials* 2021, **33**, 2007885 doi:https://doi.org/10.1002/adma.202007885

30. Sievers, G. W.; Jensen, A. W.; Quinson, J.; Zana, A.; Bizzotto, F.; Oezaslan, M.; Dworzak, A.; Kirkensgaard, J. J. K.; Smitshuysen, T. E. L.; Kadkhodazadeh, S.; Juelsholt, M.; Jensen, K. M. Ø.; Anklam, K.; Wan, H.; Schäfer, J.; Čépe, K.; Escudero-Escribano, M.; Rossmeisl, J.; Quade, A.; Brüser, V.; Arenz, M., Self-Supported Pt–Coo Networks Combining High Specific Activity with High Surface Area for Oxygen Reduction. *Nature Materials* 2021, **20**, 208-213 doi:10.1038/s41563-020-0775-8

31. Zhu, E.; Wu, M.; Xu, H.; Peng, B.; Liu, Z.; Huang, Y.; Li, Y., Stability of Platinum-Group-Metal-Based Electrocatalysts in Proton Exchange Membrane Fuel Cells. *Advanced Functional Materials* 2022, **n/a**, 2203883 doi:https://doi.org/10.1002/adfm.202203883

32. Bertram, M.; Prössl, C.; Ronovský, M.; Knöppel, J.; Matvija, P.; Fusek, L.; Skála, T.; Tsud, N.; Kastenmeier, M.; Matolín, V.; Mayrhofer, K. J. J.; Johánek, V.; Mysliveček, J.; Cherevko, S.; Lykhach, Y.; Brummel, O.; Libuda, J., Cobalt Oxide-Supported Pt Electrocatalysts: Intimate Correlation between Particle Size, Electronic Metal–Support Interaction and Stability. *The Journal of Physical Chemistry Letters* 2020, **11**, 8365-8371 doi:10.1021/acs.jpclett.0c02233

33. Zeng, Z.; Chang, K.-C.; Kubal, J.; Markovic, N. M.; Greeley, J., Stabilization of Ultrathin (Hydroxy)Oxide Films on Transition Metal Substrates for Electrochemical Energy Conversion. *Nature Energy* 2017, **2**, 17070 doi:10.1038/nenergy.2017.70

34. Schmies, H.; Bergmann, A.; Drnec, J.; Wang, G.; Teschner, D.; Kühl, S.; Sandbeck, D. J. S.; Cherevko, S.; Gocyla, M.; Shviro, M.; Heggen, M.; Ramani, V.; Dunin-Borkowski, R. E.; Mayrhofer, K. J. J.; Strasser, P., Unravelling Degradation Pathways of Oxide-Supported Pt Fuel Cell Nanocatalysts under in Situ Operating Conditions. *Advanced Energy Materials* 2018, **8**, 1701663 doi:https://doi.org/10.1002/aenm.201701663

35. Xu, C.; Yang, J.; Liu, E.; Jia, Q.; Veith, G. M.; Nair, G.; DiPietro, S.; Sun, K.; Chen, J.; Pietrasz, P.; Lu, Z.; Jagner, M.; Gath, K. K.; Mukerjee, S.; Waldecker, J. R., Physical Vapor Deposition Process for Engineering Pt Based Oxygen Reduction Reaction Catalysts on Nbox Templated Carbon Support. *Journal of Power Sources* 2020, **451**, 227709 doi:https://doi.org/10.1016/j.jpowsour.2020.227709

36. Zhao, Z.; Hossain, M. D.; Xu, C.; Lu, Z.; Liu, Y.-S.; Hsieh, S.-H.; Lee, I.; Gao, W.; Yang, J.; Merinov, B. V.; Xue, W.; Liu, Z.; Zhou, J.; Luo, Z.; Pan, X.; Zaera, F.; Guo, J.; Duan, X.; Goddard, W. A.; Huang, Y., Tailoring a Three-Phase Microenvironment for High-Performance Oxygen Reduction Reaction in Proton Exchange Membrane Fuel Cells. *Matter* 2020, **3**, 1774-1790 doi:https://doi.org/10.1016/j.matt.2020.09.025

37. Arruda, T. M.; Shyam, B.; Ziegelbauer, J. M.; Mukerjee, S.; Ramaker, D. E., Investigation into the Competitive and Site-Specific Nature of Anion Adsorption on Pt Using in Situ X-Ray Absorption Spectroscopy. *The Journal of Physical Chemistry C* 2008, **112**, 18087-18097 doi:10.1021/jp8067359

38. Jia, Q.; Liang, W.; Bates, M. K.; Mani, P.; Lee, W.; Mukerjee, S., Activity Descriptor Identification for Oxygen Reduction on Platinum-Based Bimetallic Nanoparticles: In Situ Observation of the Linear Composition–Strain–Activity Relationship. *ACS Nano* 2015, **9**, 387-400 doi:10.1021/nn506721f

39. Newville, M., Ifeffit: Interactive Xafs Analysis and Feff Fitting. *J Synchrotron Radiat* 2001, **8**, 322-4 doi:10.1107/s0909049500016964

40. Ravel, B.; Newville, M., Athena, Artemis, Hephaestus: Data Analysis for X-Ray Absorption Spectroscopy Using Ifeffit. *J Synchrotron Radiat* 2005, **12**, 537-41 doi:10.1107/s0909049505012719

41. Newville, M.; Līviņš, P.; Yacoby, Y.; Rehr, J. J.; Stern, E. A., Near-Edge X-Ray-Absorption Fine Structure of Pb: A Comparison of Theory and Experiment. *Phys Rev B* 1993, **47**, 14126-14131 doi:10.1103/PhysRevB.47.14126

42. Ankudinov, A. L.; Ravel, B.; Rehr, J. J.; Conradson, S. D., Real-Space Multiple-Scattering Calculation and Interpretation of X-Ray-Absorption near-Edge Structure. *Phys Rev B* 1998, **58**, 7565-7576 doi:10.1103/PhysRevB.58.7565

43. Zhao, Z.; Liu, Z.; Zhang, A.; Yan, X.; Xue, W.; Peng, B.; Xin, H. L.; Pan, X.; Duan, X.; Huang, Y., Graphene-Nanopocket-Encaged Ptco Nanocatalysts for Highly Durable Fuel Cell Operation under Demanding Ultralow-Pt-Loading Conditions. *Nature Nanotechnology* 2022, doi:10.1038/s41565-022-01170-9

44. Yarlagadda, V.; Carpenter, M. K.; Moylan, T. E.; Kukreja, R. S.; Koestner, R.; Gu, W.; Thompson, L.; Kongkanand, A., Boosting Fuel Cell Performance with Accessible Carbon Mesopores. *ACS Energy Letters* 2018, **3**, 618-621 doi:10.1021/acsenergylett.8b00186

45. Garrick, T. R.; Moylan, T. E.; Carpenter, M. K.; Kongkanand, A., Electrochemically Active Surface Area Measurement of Aged Pt Alloy Catalysts in Pem Fuel Cells by Co Stripping. *Journal of The Electrochemical Society* 2016, **164**, F55-F59 doi:10.1149/2.0381702jes

46. Hydrogen Class 8 Long Haul Truck Targets. US Department of Energy: https://www.hydrogen.energy.gov/program_records.html, 2019.

47. Aprà, E.; Ferrando, R.; Fortunelli, A., Density-Functional Global Optimization of Gold Nanoclusters. *Physical Review B* 2006, **73**, 205414 doi:10.1103/PhysRevB.73.205414

48. Wales, D. J.; Doye, J. P. K., Global Optimization by Basin-Hopping and the Lowest Energy Structures of Lennard-Jones Clusters Containing up to 110 Atoms. *The Journal of Physical Chemistry A* 1997, **101**, 5111-5116 doi:10.1021/jp970984n

49. Perdew, J. P.; Burke, K.; Ernzerhof, M., Generalized Gradient Approximation Made Simple. *Physical Review Letters* 1996, **77**, 3865-3868 doi:10.1103/PhysRevLett.77.3865

50. Ozaki, T. Openmx Package. http://www.openmx-square.org/.

51. Ozaki, T.; Kino, H., Numerical Atomic Basis Orbitals from H to Kr. *Physical Review B* 2004, **69**, 195113 doi:10.1103/PhysRevB.69.195113

52. Duy, T. V. T.; Ozaki, T., A Decomposition Method with Minimum Communication Amount for Parallelization of Multi-Dimensional Ffts. *Computer Physics Communications* 2014, **185**, 153-164 doi:https://doi.org/10.1016/j.cpc.2013.08.028

53. Ozaki, T. Database (2019) of Optimized Vps and Pao. https://t-ozaki.issp.u-tokyo.ac.jp/vps_pao2019/.

54. Barber, C. B.; Dobkin, D. P.; Huhdanpaa, H., The Quickhull Algorithm for Convex Hulls. *ACM Trans. Math. Softw.* 1996, **22**, 469–483 doi:10.1145/235815.235821

55. Giannozzi, P.; Baroni, S.; Bonini, N.; Calandra, M.; Car, R.; Cavazzoni, C.; Ceresoli, D.; Chiarotti, G. L.; Cococcioni, M.; Dabo, I.; Dal Corso, A.; de Gironcoli, S.; Fabris, S.; Fratesi, G.; Gebauer, R.; Gerstmann, U.; Gougoussis, C.; Kokalj, A.; Lazzeri, M.; Martin-Samos, L.; Marzari, N.; Mauri, F.; Mazzarello, R.; Paolini, S.; Pasquarello, A.; Paulatto, L.; Sbraccia, C.; Scandolo, S.; Sclauzero, G.; Seitsonen, A. P.; Smogunov, A.; Umari, P.; Wentzcovitch, R. M., Quantum Espresso: A Modular and Open-Source Software Project for Quantum Simulations of Materials. *Journal of Physics: Condensed Matter* 2009, **21**, 395502 doi:10.1088/0953-8984/21/39/395502

56. Garrity, K. F.; Bennett, J. W.; Rabe, K. M.; Vanderbilt, D., Pseudopotentials for High-Throughput Dft Calculations. *Computational Materials Science* 2014, **81**, 446-452 doi:https://doi.org/10.1016/j.commatsci.2013.08.053

57. Dabo, I.; Kozinsky, B.; Singh-Miller, N. E.; Marzari, N., Electrostatics in Periodic Boundary Conditions and Real-Space Corrections. *Physical Review B* 2008, **77**, 115139 doi:10.1103/PhysRevB.77.115139

58. Andreussi, O.; Marzari, N., Electrostatics of Solvated Systems in Periodic Boundary Conditions. *Physical Review B* 2014, **90**, 245101 doi:10.1103/PhysRevB.90.245101

59. *Qstem: Quantitative Tem/Stem Simulations*; https://www.physik.hu-berlin.de/en/sem/software/software_qstem.

60. Luo, M.; Guo, S., Strain-Controlled Electrocatalysis on Multimetallic Nanomaterials. *Nature Reviews Materials* 2017, **2**, 17059 doi:10.1038/natrevmats.2017.59

61. Stariha, S.; Macauley, N.; Sneed, B. T.; Langlois, D.; More, K. L.; Mukundan, R.; Borup, R. L., Recent Advances in Catalyst Accelerated Stress Tests for Polymer Electrolyte Membrane

Fuel Cells. *Journal of The Electrochemical Society* 2018, **165**, F492-F501 doi:10.1149/2.0881807jes

62. Chong, L.; Wen, J.; Kubal, J.; Sen, F. G.; Zou, J.; Greeley, J.; Chan, M.; Barkholtz, H.; Ding, W.; Liu, D.-J., Ultralow-Loading Platinum-Cobalt Fuel Cell Catalysts Derived from Imidazolate Frameworks. *Science* 2018, **362**, 1276-1281 doi:10.1126/science.aau0630

63. Spendelow, J. S. *Advanced Electro-Catalysts through Crystallographic Enhancement*; U.S. Department of Energy: https://www.hydrogen.energy.gov/pdfs/review19/fc161_spendelow_2019_o.pdf, 2019.

64. Nilsson, A.; Pettersson, L. G. M.; Hammer, B.; Bligaard, T.; Christensen, C. H.; Nørskov, J. K., The Electronic Structure Effect in Heterogeneous Catalysis. *Catalysis Letters* 2005, **100**, 111-114 doi:10.1007/s10562-004-3434-9

65. Sundararaman, R.; Goddard, W. A.; Arias, T. A., Grand Canonical Electronic Density-Functional Theory: Algorithms and Applications to Electrochemistry. *The Journal of Chemical Physics* 2017, **146**, 114104 doi:10.1063/1.4978411

66. Lopes, P. P.; Strmcnik, D.; Tripkovic, D.; Connell, J. G.; Stamenkovic, V.; Markovic, N. M., Relationships between Atomic Level Surface Structure and Stability/Activity of Platinum Surface Atoms in Aqueous Environments. *ACS Catalysis* 2016, **6**, 2536-2544 doi:10.1021/acscatal.5b02920

67. Huang, J.; Sementa, L.; Liu, Z.; Barcaro, G.; Feng, M.; Liu, E.; Jiao, L.; Xu, M.; Leshchev, D.; Lee, S.-J.; Li, M.; Wan, C.; Zhu, E.; Liu, Y.; Peng, B.; Duan, X.; Goddard, W. A.; Fortunelli, A.; Jia, Q.; Huang, Y., Experimental Sabatier Plot for Predictive Design of Active and Stable Pt-Alloy Oxygen Reduction Reaction Catalysts. *Nature Catalysis* 2022, **5**, 513-523 doi:10.1038/s41929-022-00797-0

Chapter 5. Conclusion and Perspective

During the five years of my Ph.D. journey, I have designed multiple nanocatalysts and evaluated these catalysts in both RDE and MEA testing. These discoveries of unique nanocatalysts with exceptional performance provide a rich and unique platform for discovering and understanding the actual configuration of catalytic active sites for ORR; and exploring new design principles for ORR nanocatalysts to meet the practical needs of PEMFC. By combining advanced characterization and computational simulations, I have discovered and rationalized several effective performance and durability enhancement strategies for practical fuel cells. As a result, my coworkers and I have successfully demonstrated advanced catalysts meeting the DOE targets for light-duty applications as well as the emerging heavy-duty applications. Moreover, I have recognized the gap between laboratory-scale RDE testing and device-level MEA testing.

In the future, I will mainly focus on the following topics:

1. Understand the operating conditions in practical fuel cells and develop effective performance and durability enhancement strategies, including the engineering of catalyst, support, and ionomer electrolyte interfaces.
2. Develop and design high-performance catalysts aiming for the specific needs in heavy-duty applications which emphasize on durability and energy conversion efficiency.
3. Continue exploration of advanced electrocatalysts for multiple energy conversion reaction, including water electrolysis and hydrogen fuel cells that are crucial for making hydrogen an important part of a clean energy future.